

Electronic Thesis and Dissertation Repository

---

10-8-2020 1:00 PM

## A Periglacial Landsystem Analysis in the Canadian High Arctic: A Tool for Planetary Geomorphology

Chimira Nicole Andres, *The University of Western Ontario*

Supervisor: Osinski, Gordon R., *The University of Western Ontario*

A thesis submitted in partial fulfillment of the requirements for the Master of Science degree in Geophysics

© Chimira Nicole Andres 2020

Follow this and additional works at: <https://ir.lib.uwo.ca/etd>



Part of the [Geology Commons](#), [Geomorphology Commons](#), [Geophysics and Seismology Commons](#), [Glaciology Commons](#), [Natural Resources and Conservation Commons](#), and the [Sedimentology Commons](#)

---

### Recommended Citation

Andres, Chimira Nicole, "A Periglacial Landsystem Analysis in the Canadian High Arctic: A Tool for Planetary Geomorphology" (2020). *Electronic Thesis and Dissertation Repository*. 7528.  
<https://ir.lib.uwo.ca/etd/7528>

This Dissertation/Thesis is brought to you for free and open access by Scholarship@Western. It has been accepted for inclusion in Electronic Thesis and Dissertation Repository by an authorized administrator of Scholarship@Western. For more information, please contact [wlsadmin@uwo.ca](mailto:wlsadmin@uwo.ca).





## Summary for Lay Audience

The Canadian High Arctic Archipelago has many similarities to ice-rich planetary bodies like Mars. On Earth, permafrost (or frozen ground) in high-latitude and high-altitude areas is the main driving factor for changes in the landscape overtime. As years pass, permafrost terrain that overlay massive volumes of ice underground start to degrade and shape landforms such as patterned ground. Examples of periglacial patterned ground landforms include honeycomb like-polygons, stone circles, mud boils, gully-polygons (or “gullygons”) and more. Surprisingly, these landforms can also be seen on Mars, which poses the question: *Are we able to estimate how much ice there is underneath the surface of Mars by looking at the landforms on Earth? Will investigations on Earth be able to infer how the landscape of Mars looked/will look like in the past/in the future?* This research goes into depth on how these potentially ice-rich landforms are all connected and affect the formation of one another using different fieldwork and mapping methods – a concept called landsystem analysis.

Fieldwork was done in Devon Island, Nunavut in July 2018/July-August 2019 as well as Axel Heiberg Island, Nunavut in July 2019. This was done through three different methods: (1) *sedimentology*; measuring sediment grains, (2) *geomorphology*; mapping landforms, (3) *ground penetrating radar (GPR)*; a non-invasive towed system to classify different soil layers, and (4) *kinematic light detection altimetry and ranging*; a laser on a backpack for 3D modelling of the terrain. Data collected showed that ice-wedge polygons often occur in secondary and tertiary polygons (multiple episodes of cracking) locally in the middle of transition areas within the landscape (i.e. smaller to bigger polygons, from the mouth of an alluvial fan to the terminus; Chapter 2). It also showed that 3D-GPR is a powerful tool to visualize the ground for the shape/size of ice-wedges in order to estimate ice volume (Chapter 2). In combination with quantitative geomorphology (Chapter 3), we were also able to measure the compactness, elongation ratio, and other shape descriptors of patterned ground and found a potential trend.

All in all, periglacial (permafrost) landforms and patterns can provide a better understanding of how buried ice behaves and how the landscape of the Canadian High Arctic Archipelago evolves over time as a resource for communities/planetary exploration.

## Co-Authorship Statement

The concept behind this thesis grew as a discussion with Drs. Gordon R. Osinski, Etienne Godin, and Dr. Carolyn Eyles (McMaster University), with all providing initial guidance. Overall contributions to this thesis were made by Dr. Gordon Osinski, Dr. Etienne Godin, Antero Kukko, and Dr. Michael Zanetti. Dr. Gordon Osinski and Dr. Etienne Godin provided commentary and feedback on all thesis chapters as well as suggesting Axel Heiberg and Devon Island as ideal field sites for a “periglacial Mars” analogue. Antero Kukko kindly supported and built the LiDAR systems used to collect high resolution topography as per Chapter 2 and 3. Dr. Michael Zanetti provided assistance with the production and processing of the LiDAR figures. Chimira N. Andres is the lead author on all chapters and is primarily responsible for all research, writing, data collection, digitization, processing, and presentation of results.

## Acknowledgments

Thank you to my family, Charlie, Dorothy, Chloei, and Riley, who have always been (and continue to be) so supportive throughout my life no matter how big the dream. I am so grateful for everything that you have done for me and will be forever more.

A sincere and heartfelt thank you to my advisor, Dr. Gordon R. Osinski, for firstly accepting me as his MSc student, taking a chance on me, taking me under his wing, and showing me the true beauty of the Canadian High Arctic. I have been truly inspired by everything that you do and will forever cherish the training and encouragement that you have given me throughout my 2 years at Western. Without a doubt, it has been a true honour to be your student.

A huge thanks also to Dr. Etienne Godin for your unfailing guidance throughout my MSc journey. Ever since I met you during our first field season, after getting attacked by a polar bear, getting ATVs stuck, and enduring the strong winds at the Houghton Impact Crater together, I can honestly say that I do not know what I would have done without you.

To my partner in life, Julian, who through the thick and thin, has always been by my side to provide me with support, love and compassion in every form possible. You are my very best friend and thanks for teaching me to use passion and drive as tools to succeed in whatever I do. I admire and look up to you in more ways that you can even imagine – I look forward to the amazing things we will achieve together!

Lastly, thank you to my unclaimed support system, whom behind the scenes inspired me to be better than I was yesterday and to try new things each and every day: my “space moms” Courtney Barrett and Dr. Parshati Patel. Also, a huge thanks goes to Dr. Livio Tornabene, for the training on all things ENVI, Mars Mission Planning, and HiRISE as well as Amy Wickham who has helped me navigate through the Earth Sciences department for the benefit of my overall degree.

It’s been a treat.



1.7	Landsystem Analysis .....	23
1.7.1	The Development of the Landsystem Concept.....	23
1.7.2	Utility of Landsystem Analysis in Periglacial Environments.....	24
1.8	Chapter Summary .....	28
1.9	Introduction to Thesis .....	29
1.10	References.....	31
Chapter 2.....		41
2	A Periglacial Landsystem Analysis of Strand Fiord, Axel Heiberg Island, Nunavut: <i>A Polar Desert Case Study on Polygonal Terrain Evolution</i> .....	41
2.1	Introduction.....	41
2.2	Study Area .....	44
2.3	Methods .....	46
2.3.1	Sedimentological Logging and Description .....	46
2.3.2	LiDAR .....	47
2.3.3	Geophysical Survey: Ground Penetrating Radar (GPR) .....	47
2.4	Results.....	49
2.4.1	Field Observations .....	50
2.4.2	Sedimentology .....	55
2.4.3	Radargram Facies & 3D-GPR Modelling of Subsurface Ice.....	64
2.5	Discussion.....	68
2.5.1	Surface Evolution: <i>Polygon Size Variation</i> .....	68
2.5.2	Surface Evolution: <i>Secondary Polygon Formation</i> .....	70
2.5.3	Heterogeneity of Distribution of Ice.....	73
2.5.4	Periglacial Landsystem Model .....	75
2.6	Conclusions.....	77
2.7	References.....	80
Chapter 3.....		83

3	Utility of Hyper-Resolution LiDAR for Patterned Ground Geomorphometry in the Haughton River Valley, Devon Island, Nunavut.....	83
3.1	Introduction.....	83
3.2	Study Area .....	86
3.3	Methods and Data Collection .....	88
3.3.1	Remote Sensing Field Methods: Light Detection and Ranging (LiDAR).....	88
3.3.2	Geomorphometric Image Analysis .....	89
3.3.3	Kernel Density Estimation (KDE).....	90
3.3.4	Lithological Mapping .....	91
3.4	Results.....	91
3.4.1	General Lithology, Remote Sensing Observations and Quantification.....	91
3.4.2	Cumulative Spatial Sorting Analysis.....	109
3.5	Discussion.....	110
3.5.1	Variations in Patterned Ground Morphology .....	111
3.5.2	Periglacial Landsystem Model for the Haughton River Valley.....	113
3.6	Conclusions.....	114
3.7	References.....	117
	Chapter 4.....	121
4	Summary and Future Work.....	121
4.1	Contributions to Periglacial Science.....	122
4.1.1	The Periglacial Landsystem.....	122
4.1.2	3D-GPR and Sedimentology of Ice-wedge Polygons .....	123
4.2	The Canadian High Arctic as an Icy Analogue for Mars .....	124
4.2.1	Targeted Techniques to Characterize Periglacial Terrain .....	125
	Curriculum Vitae .....	126

## List of Tables

<b>Table 1.1.</b> Genetic classification of patterned ground morphology (modified from Washburn, 1973; Washburn, 1980).....	12
<b>Table 1.2.</b> Akhka-R3 backpack Kinematic LiDAR System (KLS) .....	19
<b>Table 1.3.</b> AkhkaR4DW backpack mobile laser scanning system components .....	19
<b>Table 2.1.</b> Statistics for length, width, area, and diameter of polygons in all zones measured in meters from satellite imagery (i.e Worldview) observations. ....	51
<b>Table 2.2.</b> Stratigraphic units and facies types identified in the Apex/Proximal, Transition/Medial, and Distal Zones of the Strand Fiord alluvial fossil fan (see Figure 6 for facies codes).....	59
<b>Table 2.3.</b> Stratigraphic units and facies types identified in the Fan Edge Zone outcrop (see Figure 2.7 for facies codes).....	63
<b>Table 3.1.</b> Coordinates of the nine LiDAR Grids in the Haughton River Valley used for this study. The latitudes and longitudes of the 9 grids are listed in Decimal Degrees and UTM meters and the map projection is UTM 16N, WGS 84.....	88
<b>Table 3.2.</b> Elementary diagrams and equations for shape descriptors used for patterned ground analysis. ....	90
<b>Table 3.3.</b> Summary chart of geomorphometric statistics of patterned ground in the HRV (Note: Long axis azimuth values range from 0-180, 90 trending E-W and 180 trending N-S).....	92

## List of Figures

<b>Figure 1.1. (A)</b> Geologic map of the Canadian Arctic Archipelago (adapted from Arne et al., 2002; Embry, 2009), highlighting the extent of the Sverdrup Basin (in green). <b>(B)</b> A contextual map of Axel Heiberg Island, Nunavut within the Sverdrup Basin.....	4
<b>Figure 1.2.</b> Devon Island geologic map highlighting the Arctic Sedimentary Platform and showing the location of the Haughton Impact Structure (Osinski et al., 2005) .....	6
<b>Figure 1.3.</b> Freeze-thaw indices for specific permafrost types and their thermal controls. The outer limit outlined in grey represents the range of values observed on Earth. The Canadian High Arctic sites lie within the continuous permafrost regional gradient (adapted from Harris, 1982). .....	8
<b>Figure 1.4.</b> Topographic map of Mars illustrated using colourized Mars Orbiter Laser Altimeter (MOLA) data. Utopia Planitia is labeled as the basin and/or lowlands situated on the northeast portion of the map in blue. Image credit: Christine M. Rodrigue, Department of Geography, California State University. ....	10
<b>Figure 1.5.</b> Examples of facies codes for sedimentology applications used in this study (adapted from Andres et al., 2018 and Eyles et al., 1983).....	14
Figure 1.6. A North American classification of cryostructures proposed by Murton and French (1994). (A) Cryostructure types and codes with ice shown in white and sediment in black. (B) terms and illustrations to describe layered and lenticular cryostructures.....	16
<b>Figure 1.7. (A)</b> 2017 field team member (Michael Zanetti) traversing with the Akhka-R3 Kinematic Lidar System (KLS) in the Haughton Impact Structure on Devon Island in the Canadian High-Arctic <b>(B)</b> Prof. Antero Kukko traversing with the AkhkaR4DW Backpack mobile laser scanning system in the Mokka Fiord Valley on Axel Heiberg Island in the Canadian High-Arctic in 2018. ....	18
<b>Figure 1.8.</b> ArcticDEM (A) hillshaded 2m-DEM of Axel Heiberg <b>(B)</b> raw 2m-DEM of Haughton Crater.....	20



<b>Figure 1.9.</b> Concept of GPR survey setup and image of the Sensors and Software Noggin™ 250MHz ground penetrating radar (left). Dielectric permittivity calculations for various types of ground ice in periglacial environments (from Thompson et al., 2012)...	21
<b>Figure 1.10.</b> 3D GPR cube model of Footprint Lake to image ice-wedge networks in Lake Manitoba, Canada (left; Munroe et al., 2007). 3D Model of ice wedge volume estimates for a High Arctic polar desert environment, Fosheim Peninsula, Ellesmere Island (right; Bernard-Grand’Maison and Pollard; 2018). .....	22
<b>Figure 1.11</b> A hierarchal overview of landsystem terrain elements. This diagram illustrates the relationship between different system tracts: (1) the terrain system, (2) terrain facet, and (3) terrain element (Cooke & Doornkamp 1990). .....	24
<b>Figure 1.12.</b> First geomorphologic map of Axel Heiberg. Field sketch of the north-facing Expedition Fiord landsystem (Rudberg, 1983).....	26
<b>Figure 1.13</b> Landscape model for depression formation in Deuteronilus Mensae; illustrate initial formation by either (A) impact cratering, or (B) thermokarst degradation and subsequent erosion, or (C) headward erosion by thaw slumping. (D) After formation of the main depression a volatile-rich layer might have been deposited from the atmosphere at midlatitudes in the course of obliquity changes. (E) Here the atmospheric deposit has been substantially eroded, mixed with older material and moves downslope toward the North (Van Gasselt et al., 2010). .....	28
<b>Figure 2.1.</b> (A) Map of a portion of the Canadian High Arctic Archipelago highlighting Axel Heiberg Island and the study site located in Strand Fiord <i>Source: Esri.</i> (B) A subset map of the study site (outlined in the black box) and valley networks to provide contextual setting of the fiord system. <i>Source: Esri.</i> (C) An oblique aerial photograph of the study site of the polygonized “fossil” fan on Strand Fjord, Axel Heiberg Island. The high albedo or light colour-toned features on the fan are water-marker indicators of mineral deposits (i.e. gypsum). There is a smaller, more recently active fan to the left-most of the image.....	46
<b>Figure 2.2.</b> Sediment overlaying bedrock cross-section of deglaciated trunk river valley encompassing the study site. The top is a Landsat 8 satellite image showing a 5-km	

profile of the cross section from point B to B' with elevation values extracted from Google Earth (meters above sea level or m.a.s.l.). The bottom is a schematic and interpreted landsystem diagram highlighting various physiographic features of the valley estimated through bedrock depth (exposed through the valley walls) and the depth of overlying sediment and active layer. ....49

**Figure 2.3.** (A) Aerial (taken in summer 2016 via helicopter) and (B) ground images of polygons at the Strand Fiord alluvial fan looking towards the west.....50

**Figure 2.4.** Context image of the study area. (A) Aerial photograph of study area showing sedimentological excavation, GPR and LiDAR sites. (B) Strand Fiord alluvial fossil fan classification zones projected onto (A) at identical zoom scales to show consistency. Green dots show sites of polygon centre excavation and red dots show sites of polygon trough excavation. (C) Partial LiDAR coverage map of the alluvial fan (covering 350m horizontal scale). Partial LiDAR coverage of the study area is also shown in Figure 3 with a 25m x 25m white box within the LiDAR image that represents the GPR grid. Additionally, six pits were excavated throughout the alluvial fossil fan composed of two sediment pits per zone located on the polygon troughs and centres shown by the red and green dots respectively. A profile cross-section of the fan was acquired using A-A' coordinates shown in Figure 2.6. With relevance to the thaw depth of the active layer, it should be mentioned that these excavated pits were dug on July 4<sup>th</sup> and 6<sup>th</sup> 2019. ....54

**Figure 2.5.** 3cm LiDAR DEM showing clustering of secondary polygons as well as a distinct polygon ridge that may indicate the outward movement of sediment from polygons towards the ice wedges (troughs) shown by the black arrow. A possible downstream flow feature downslope towards possible ice-wedge replenishment. ....56

**Figure 2.6.** Sedimentological log of the six sediment pits/excavations throughout Strand Fiord alluvial fossil fan sediments. Sedimentary facies types are grouped into units (PPC/PPT, MPC/MPT, DMC/DMT) depending on their location on the fan. Profile A-A' follows the exact topography of the fan illustrating the transition of the fan sediments from fine-medium sands (Apex/Proximal Zone) to fine silty clays (Distal Zone). The

facies codes and symbols are shown in the legend. No data are available regarding the nature of sediments beneath these sediment pits due to the frozen nature of the ground..58

**Figure 2.7.** (A) Sedimentological log of the 12.5-meter-high exposure through the Strand Fiord alluvial fossil fan sediments. Sedimentary facies types are grouped into units (A-H). The facies codes and symbols are shown in the legend. No data are available regarding the nature of sediments beneath those exposed in outcrop. (B) An 3D image rendering of the Fan Edge Zone showing an incision from a fan feeder stream along a polygon trough where (A) is located. This model was made using terrestrial photogrammetric techniques. (C) 12.5-meter-high outcrop of Strand Fiord alluvial fossil fan sediments in the Fan Edge Zone.....62

**Figure 2.8.** (Top) Stratigraphic reconstruction of an ice-wedge-polygon system within the Transition/Medial Zone using data from cross sections, GPR profiles and sedimentological analyses. (Bottom) 25m GPR profile conducted at 250 MHz straddling polygons A and B within the 25m x 25m grid. Radargram interpretation has been incorporated into (Top).....66

**Figure 2.9.** (A) Stacked GPR depth slices rendered using MATLAB. Probable ice-rich areas and ice-wedges are highlighted in yellow mostly saturated in polygon troughs. (B) Voxler model of ice-wedge isosurfaces using isolated data from GPR radargrams. The active layer thaw depth is illustrated by the black bolded line in both images. ....67

**Figure 2.10.** A schematic flowchart of plausible polygon evolution. This chart outlines causative factors, effects, and measurable parameters when analyzing the formation and morphological processes of polygonal terrain. *\*Not limited to outlined measurable parameters. NOTE: Causative factors and effects are all independent of one another. ...72*

**Figure 2.11.** Schematic diagram to illustrate landsystem constituents characteristic of a periglacial, alluvial-dominated landsystem. This is the current stage of sedimentation and evolution of Strand Fiord alluvial fossil fan. ....76

**Figure 3.1.** (A) Context map of the Houghton Impact Structure, Devon Island, Nunavut. (B) An Annotated map of the Houghton River Valley study site and grid sites within the localized zone. Basecamp in labeled in a black star for reference. ....87

**Figure 3.2.** A general overview of the distribution and location of the nine 1cm-LiDAR grids that were scanned in the Houghton River Valley showing their relative lithology. (A), (B), (C), (E), and (F) are stone circles, (G) and (I) are mud boils, (H) are polygons, and (D) are stripes. LiDAR digital elevation models are analyzed in detail in next figures following this spatial distribution.....94

**Figure 3.3.** (A) LiDAR digital elevation map showing topographical variations on a centimeter scale for stone circles. (B) Mapped stone circle geometries in Grid 16A. (C) KDE model of the elongation ratio of Grid 16A stone circles. Lowest elongation ratio values (values closer to 0) that show more elongated features are shown in dark grey with the lighter shades signifying higher elongation ratios (values closer to 1), which are more equally rounded features. (D) KDE model of the area of stone circles in Grid 16A. Larger areas are indicated by white and smaller areas are indicated by the darker shades.....97

**Figure 3.4.** (A) LiDAR digital elevation map showing topographical variations on a centimeter scale for stone circles. (B) Mapped stone circle geometries in Grid 16C. (C) KDE model of the elongation ratio of Grid 16C stone circles. Lowest elongation ratio values (values closer to 0) that show more elongated features are shown in dark grey with the lighter shades signifying higher elongation ratios (values closer to 1), which are more equally rounded features. (D) KDE model of the area of stone circles in Grid 16C. Larger areas are indicated by white and smaller areas are indicated by the darker shades.....98

**Figure 3.5.** (A) LiDAR digital elevation map showing topographical variations on a centimeter scale for stone circles. (B) Mapped stone circle geometries in Grid 16D. (C) KDE model of the elongation ratio of Grid 16D stone circles. Lowest elongation ratio values (values closer to 0) that show more elongated features are shown in dark grey with the lighter shades signifying higher elongation ratios (values closer to 1), which are more equally rounded features. (D) KDE model of the area of stone circles in Grid 16D. Larger areas are indicated by white and smaller areas are indicated by the darker shades.....99

**Figure 3.6.** (A) LiDAR digital elevation map showing topographical variations on a centimeter scale for stone circles. (B) Mapped stone circle geometries in Grid 16K. (C) KDE model of the elongation ratio of Grid 16K stone circles. Lowest elongation ratio values (values closer to 0) that show more elongated features are shown in dark grey with

the lighter shades signifying higher elongation ratios (values closer to 1), which are more equally rounded features. **(D)** KDE model of the area of stone circles in Grid 16K. Larger areas are indicated by white and smaller areas are indicated by the darker shades..... 100

**Figure 3.7.** **(A)** LiDAR digital elevation map showing topographical variations on a centimeter scale for stone circles. **(B)** Mapped stone circle geometries in Grid 16L. **(C)** KDE model of the elongation ratio of Grid 16L stone circles. Lowest elongation ratio values (values closer to 0) that show more elongated features are shown in dark grey with the lighter shades signifying higher elongation ratios (values closer to 1), which are more equally rounded features. **(D)** KDE model of the area of stone circles in Grid 16L. Larger areas are indicated by white and smaller areas are indicated by the darker shades..... 101

**Figure 3.8.** **(A)** LiDAR digital elevation map showing topographical variations on a centimeter scale of mud boils and frost-shattered nets. **(B)** Mapped mud boil geometries in Grid 16N. **(C)** KDE model of the elongation ratio of Grid 16N mud boils. Lowest elongation ratio values (values closer to 0) that show more elongated features are shown in dark grey with the lighter shades signifying higher elongation ratios (values closer to 1), which are more equally rounded features. **(D)** KDE model of the area of mud boils in Grid 16N. Larger areas are indicated by white and smaller areas are indicated by the darker shades. .... 103

**Figure 3.9.** **(A)** LiDAR digital elevation map showing topographical variations on a centimeter scale of mud boils and frost-shattered nets. **(B)** Mapped mud boil geometries in Grid 16AD. **(C)** KDE model of the elongation ratio of Grid 16AD mud boils. Lowest elongation ratio values (values closer to 0) that show more elongated features are shown in dark grey with the lighter shades signifying higher elongation ratios (values closer to 1), which are more equally rounded features. **(D)** KDE model of the area of mud boils in Grid 16AD. Larger areas are indicated by white and smaller areas are indicated by the darker shades. .... 104

**Figure 3.10.** **(A)** LiDAR digital elevation map showing topographical variations on a centimeter scale. **(B)** Mapped Stone Stripes geometries. **(C)** KDE model of the elongation ratio of Stone Stripes. Lowest elongation ratio values (values closer to 0) that show more elongated features are shown in dark grey with the lighter shades signifying higher

elongation ratios (values closer to 1), which are more equally rounded features. **(D)** KDE model of the area of Stone Stripes. Larger areas are indicated by white and smaller areas are indicated by the darker shades. .... 106

**Figure 3.11.** **(A)** LiDAR digital elevation map showing topographical variations on a centimeter scale. **(B)** Mapped polygon geometries of East Camp Polygons. **(C)** KDE model of the elongation ratio of polygons in HRV. Lowest elongation ratio values (values closer to 0) that show more elongated features are shown in dark grey with the lighter shades signifying higher elongation ratios (values closer to 1), which are more equally rounded features. **(D)** KDE model of the area of polygons in HRV. Larger areas are indicated by white and smaller areas are indicated by the darker shades..... 108

**Figure 3.12.** Scale plot of the degree of spatial sorting using cumulative area and perimeter fractions for all patterned ground types based on vectorized shape maps **(Figures 3.3b-3.11b)**. Using image analysis, there are two groups of very well to well sorted and moderately sorted periglacial landforms (adapted from Chanou et al., 2014) ..... 110

**Figure 3.13.** Conceptual periglacial landsystem model of the Haughton River Valley (HRV), Haughton Impact Structure, Devon Island, Nunavut. This perspective is upstream of the HRV..... 114

# Chapter 1

## 1 An Overview of Principle Concepts and Techniques in Periglacial Geology

### 1.1 Introduction

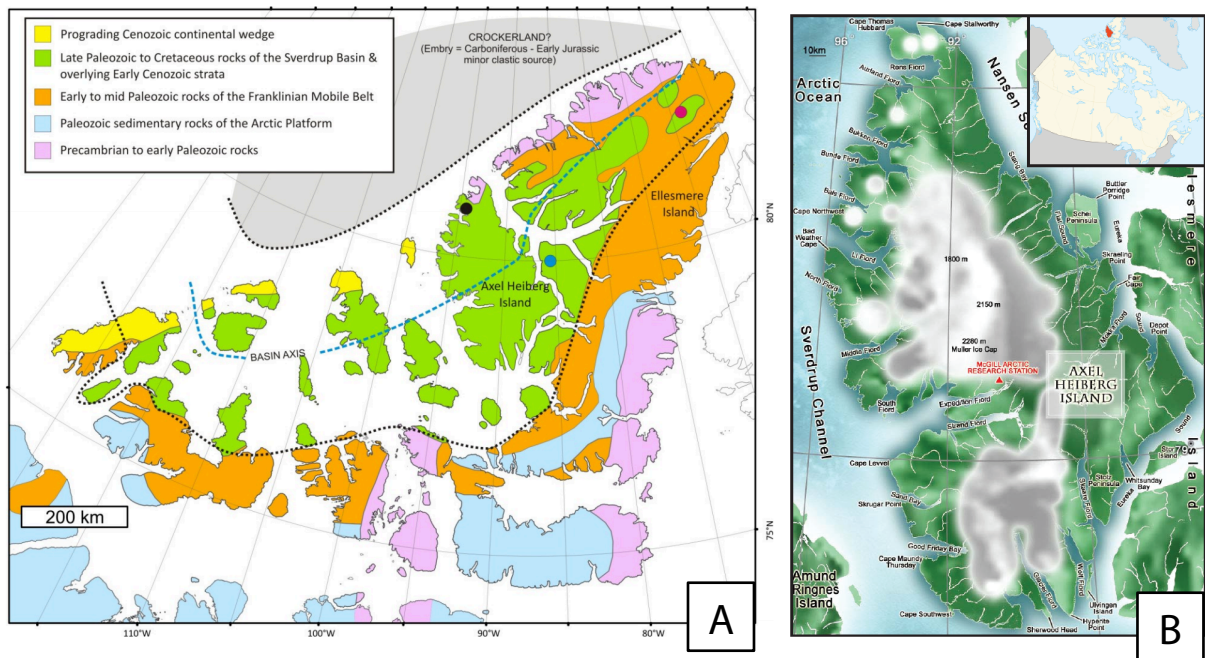
Permafrost underlies 50% of Canada's terrain (NRCan, 2019) and underlies 24% of the Earth's total land area (IPCC, 2018). By definition, permafrost is the thermal condition of earth materials, such as those involving water, soil and rock, as their temperature remains  $<0^{\circ}\text{C}$  continuously for more than two consecutive years (Brown, 1970). It is considered a major driving force for the generation of patterned ground and other landforms that are highly influenced by hydrology, geomorphology, climate, surface processes, and landscape evolution. Patterned ground is geometrically distinct and often symmetrical natural pattern of geometric shapes formed by ground material in periglacial regions commonly used as in comparative planetology such as terrestrial analogues for Mars. As today's technologies are only capable of non-crewed space travel to Mars, over numerous years, several landers and orbiter satellites have been used to gather detailed records of Martian terrain that has yet to be correlated and modelled back to Earth (i.e. Phoenix lander, Mars Advanced Radar for Subsurface and Ionosphere Sounding (MARSIS) on board Mars Express, Shallow Radar (SHARAD) and High Resolution Imaging Science Experiment (HiRISE) on board the Mars Reconnaissance Orbiter or MRO). Due to the limitations to only satellite and remotely sensed sourced, potentially glaciated and deglaciated regions of Mars have been evidenced to show Earth-like, ice-rich morphologies (i.e. patterned ground, lobate debris aprons, glacial scours), therefore, in depth investigation, and ground-truthing of these periglacial geomorphologies on Earth may give rise to further understanding of their mechanisms. More specifically, the Canadian High -Arctic shares a geomorphologic similarity with the middle and high latitudes of Mars, as both have many cold-climate landforms related to the presence of ground-ice (e.g., glacier-like flows, polygonal patterned ground, debris-flow gullies). This research studies and contrasts two study sites in the Canadian High Arctic Archipelago namely, Strand Fjord in Axel Heiberg Island (cold and dry with a mean temperature of  $-15^{\circ}\text{C}$  and total annual precipitation of  $<100$  mm;  $79.22^{\circ}$  - $90.36^{\circ}$ ) and Houghton River Valley in Devon Island (cold and wet with a mean temperature of  $-15^{\circ}\text{C}$  and total annual precipitation of  $<200$  mm;  $75.38^{\circ}$  - $89.54^{\circ}$ ).

Within a cold and dry climate zone, periglacial landsystems in the present day are often ‘cold and non-glacial’ where sediments are characteristically subject to intense freeze-thaw cycles of water-ice rather than Late Pleistocene processes as once defined by Lozinski in 1909 (French 2000, Washburn, 1980; Ballantyne, 2018). Permafrost or frozen ground is a distinguishing feature that is commonly present within periglacial environments and the formation of patterned ground is unique to the periglacial landscape. Terrestrial patterned ground systems develop through the repeated freezing and thawing of the permafrost active layer. The active layer is the upper layer of frozen soil, approximately a meter in depth on Earth and sometimes deeper on marginal and low latitudes, which is subject to seasonal freeze-thaw cycles (French, 2017). This seasonal thaw creates variable periglacial environments and results in a variety of characteristic landforms such as sorted stone circles, patterned ground, stripes, and gully-polygon systems. Thus, if Martian terrestrial patterned ground is periglacial in origin then it would act as useful geomorphic markers for sites where there may be seasonal freeze-thaw cycles.

Since water is not stable on the surface of Mars, these seasonal processes would likely occur in the subsurface. It is also possible that patterned ground in non-ice-rich regions on Mars are “relict” features and can provide information of past climate (Leslie and McGlone, 1973; Creemens et al., 2005; Rodriguez-Ochoa et al., 2019). In addition, Matthews et al. (1998) outlines the importance of investigating the concept of spatial variability, permafrost drainage, and micro-topography to validate the formation of patterned ground along with other associated periglacial features such as freeze-thaw kettle lakes, gullies, and stone circles. This was done in this study using a landsystem analysis approach. Slomka and Eyles (2015) define landsystem analysis as a commonly applied methodology when investigating process-form relationships in glacial environments. This method can characterize the periglacial landscape architecture and may be utilized to understand the landsystem evolution of Quaternary and periglacial subsurface stratigraphies in which patterned ground landforms are not apparent. This makes the delineation of the sedimentary architecture of periglacial sediment movement less difficult and more robust. By investigating the behaviour of subsurface permafrost and sediment type, patterned ground morphology may be used to deduce depositional environment in correlation with temporal change.







**Figure 1.1. (A)** Geologic map of the Canadian Arctic Archipelago (adapted from Arne et al., 2002; Embry, 2009), highlighting the extent of the Sverdrup Basin (in green). **(B)** A contextual map of Axel Heiberg Island, Nunavut within the Sverdrup Basin.

Nominally, Axel Heiberg is part of the Sverdrup Islands Basin, which include the islands, Axel Heiberg, Ellef Ringnes, Amund Ringnes, Cornwall, Graham, Meighen, King Christian, and Stor (Hund, 2014). The Sverdrup Basin is a 350,000 km<sup>2</sup> sedimentary basin that initially developed in Early Carboniferous as a rift basin upon highly deformed Early Paleozoic strata of the Ellesmerian Orogenic Belt (Embry and Beauchamp, 2008). Approximately 318 to 66 Ma, ~13 km of Carboniferous to Paleogene sediments accumulated in the basin — Axel Heiberg contains the thickest section. With this, Axel Heiberg is known for its unusual fossil forests, which date from the Eocene period. The fossil records provide strong evidence that the Axel Heiberg forest was a high-latitude wetland forest. Although, long-term climatic data are not available at widespread locations in Axel Heiberg Island a mean annual temperature for the Expedition Fjord region of approximately  $-15^{\circ}\text{C}$  and total annual precipitation of  $<100$  mm have been reported (Bigras et al., 1995).

Additionally, detailed studies of salt diapirs (e.g. Schwerdtner, 1984; Jackson and Harrison, 2006; Harrington et al., 2019) shows that Axel Heiberg Island has one of the highest concentrations of salt diapirs globally. As a result, it also hosts extensive secondary salt

deposits that have been weathered and precipitated away from their source as well as distributed in tributary valleys and flood plains such as in Strand Fiord Plateaus and Expedition Fiord. Because salt deposits and precipitates frequently provide localized water signatures upon transport and deposition, it is important to distinguish the source of these salt traps for interpretation of sedimentary and geologic data (Pollard et al, 1999, Pollard, 2005).

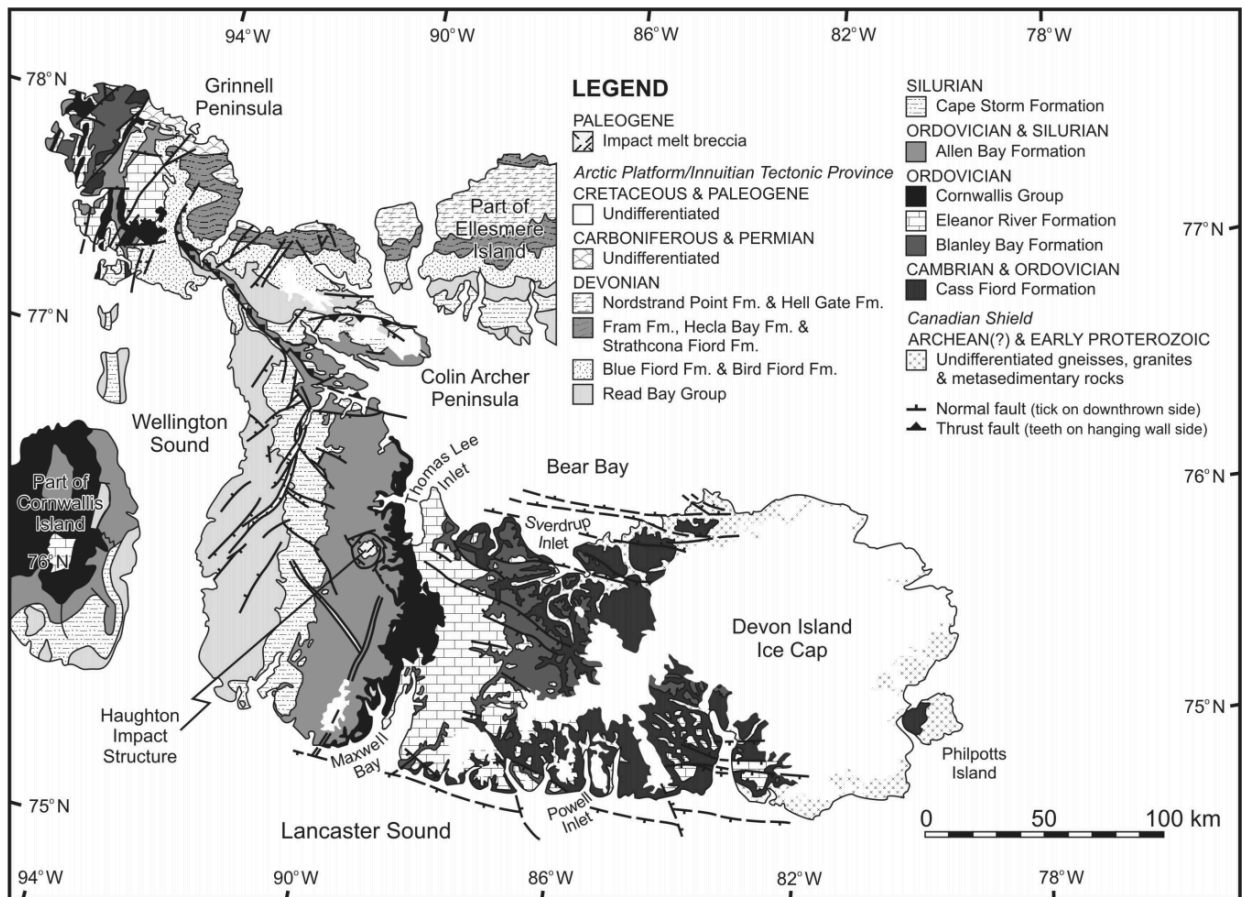
There have also been recent advances on massive sulfide deposits being associated with the High Arctic Large Igneous Province (HALIP) and Sverdrup Basin and in fact, Axel Heiberg Island holds the second example of mineralization in the Canadian High Arctic described in Wilton et al., (2019). The HALIP also houses The Strand Fiord Formation, which is a Late Cretaceous volcanic component, located on the midwestern region of the island. The formation contains flood basalts which are found on western Axel Heiberg Island at Dragon Cliffs that are ~300 m tall. The Strand Fiord Formation contains columnar jointing units that are usually 1-3 m in diameter. The formation is interpreted to represent the cratonward extension of a volcanic ridge (Ricketts et al, 1985).

## 1.2.2 Devon Island (ᑕᑦᓴᓂᑦ, Talluruti)

Devon Island is the largest uninhabited island on Earth and lies in the Canadian High Arctic located in the territory of Nunavut and the Qikiqtaaluk region. The island was first sighted by William Baffin in 1616 and was named North Devon by W.E. Parry after Devon, England. Its eastern third is covered with an ice cap with a maximum thickness of 500-700 m. The rocks consist of Precambrian, Cambrian and Ordovician in the east and Ordovician and Silurian siltstones and shales in the west. Most of the island follows a plateau topography with shallow valleys, 300-500 m in elevation; it is a barren landscape, dominated by frost-shattered rocks and nearly devoid of plants and animals. The mean annual temperature averages approximately -16°C (Lev and King, 1999).

Devon Island is widely known for the Haughton impact structure that is located there (75° 22' N, 89° 41' W), a 23 Myr, 23 km diameter complex impact crater (e.g., Osinski et al., 2005; Robertson and Sweeney, 1983; Grieve, 1988; Robertson and Mason, 1975; Frisch and Thorsteinsson 1978). Originally mapped as a salt dome (Greiner, 1963), with some association to the Sverdrup Basin ~400 km to the north, early scientists initially named this feature the Haughton Dome after Reverend Samuel Haughton, a geologist, medical doctor,

and reverend, who published one of the first geological studies of the Canadian High Arctic (Haughton 1860a, b). Nominally, Devon Island houses the Arctic Platform sediments, which is a thick sequence of Proterozoic to Paleogene sedimentary rocks that have not been folded or thrust-faulted on a regional scale (Thorsteinsson and Tozer 1970; Douglas 1970). Briefly, this includes the Proterozoic-age Strathcona Sound Formation, Cambrian and Ordovician-age Cass Fiord Formation, the Ordovician succession of the Cornwallis Group, Eleanor River and Banley Bay Formations, the Ordovician and Silurian-age Allen Bay Formation, and the Silurian-age Cape Storm Formation (Osinski et al., 2005; **Figure 1.2**). Moreover, Carboniferous to Late Jurassic-age rocks are not present on Devon Island – in fact, the youngest rocks of the Arctic Platform are of Early Cretaceous age (Osinski et al., 2005; **Figure 1.2**).



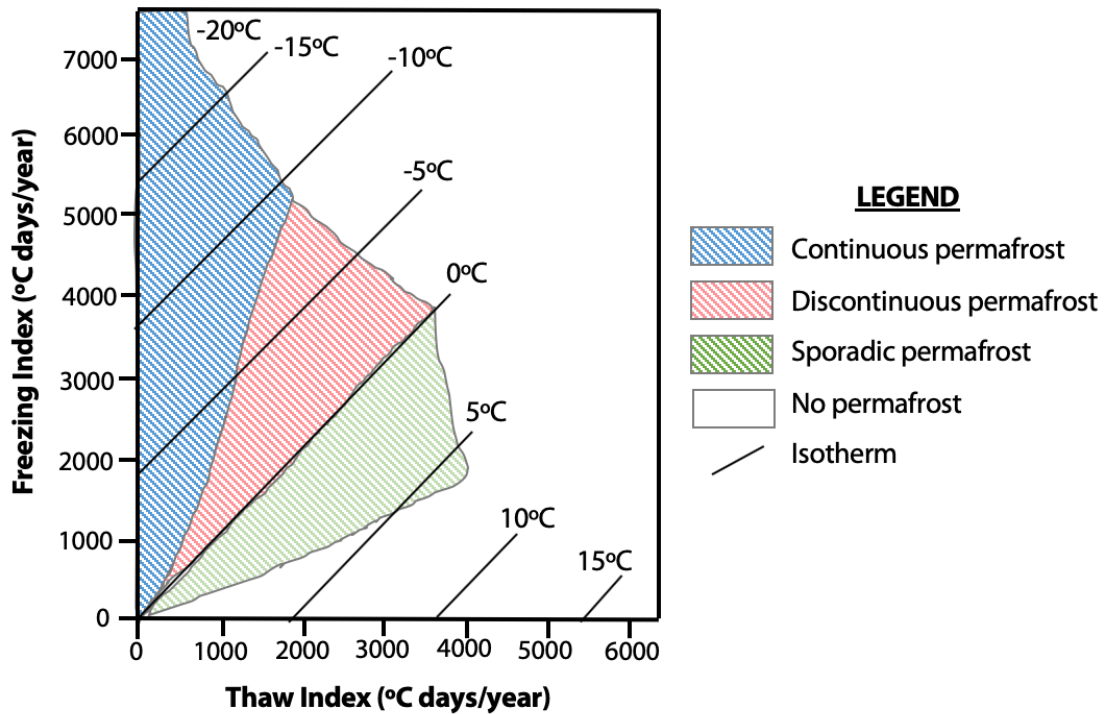
**Figure 1.2.** Devon Island geologic map highlighting the Arctic Sedimentary Platform and showing the location of the Haughton Impact Structure (Osinski et al., 2005)

## 1.3 Periglacial Environments and Patterned Ground

### 1.3.1 Ice on Earth and Mars

Lozinski first used the term *periglacial* in 1909 to explain the distribution of frost-shattered debris about the cold ice-free margins of Pleistocene glaciers (Lozinski, 1909; Embleton and King, 1968). As frost activity is not exclusive to the proximity of either former or present-day glaciers, the term *periglacial* nowadays is used to describe cold region processes and their landforms (Price, 1972; Washburn, 1979; Thorn et al., 1992). Ice is not distributed uniformly with respect to depth or content. By conservative estimates, large areas of frozen ground in the northern hemisphere contain more than 50% ice by volume within 2 to 3 m of the subsoil depth (Mackay, 1972). The depth penetration of permafrost is intricately related to the amplitude of the subfreezing mean annual temperature, rate of geothermal heat escape, time available for the permafrost to build, and hydrologic aspects of terrain. In the periglacial environment of North America, the permafrost depth increases with latitude-dependent amplitude of subfreezing mean annual temperature (Brown, 1960). The depth at which temperature remains stable above seasonal fluctuation, but yet changes over time is called the *level of zero annual amplitude*. The temperature at the level of zero amplitude in the permafrost of recent origin in North America is 0-2°C (Lachenbruch et al., 1962; Burn and Kokelj, 2009). The seasonal thaw of permafrost at the surface produces a layer of material (i.e. peat, mineral soils, coherent rock, mixed material, etc.) called active layer above the frozen ground. The base level of the active layer form a boundary with the upper limit of the permafrost body which is called the permafrost table. The thickness of the active layer varies with the complex response of the frozen ground to diurnal and seasonal temperature fluctuation, thermal conductivity of the surface, soil composition, slope and relief aspects of the terrain, and vegetation density. Therefore, the thickness of the active layer is expected to vary remarkably over short distances within the given permafrost situation (Owens and Harper, 1977). In general, the active layer is thickest in the subarctic. It progressively thins toward the northern latitudes of smaller magnitude of seasonal temperature range about the freezing point, and toward the southern latitudes of increasing thermal efficiency regime (Brown, 1970; Price, 1972). Freezing and thawing indices (**Figure 1.3**) overcome this weak relationship between the air temperature and type of permafrost. The freezing index is the sum total of daily subfreezing temperatures, and the thaw index is the aggregate of daily positive temperatures for the year as a whole (Harris

1982). The freeze-thaw indices essentially use distribution of zonal permafrost landforms for mapping limits of permafrost types. These indices have been subsequently used in this chapter for the thermal environment of periglacial landforms.



**Figure 1.3.** Freeze-thaw indices for specific permafrost types and their thermal controls. The outer limit outlined in grey represents the range of values observed on Earth. The Canadian High Arctic sites lie within the continuous permafrost regional gradient (adapted from Harris, 1982).

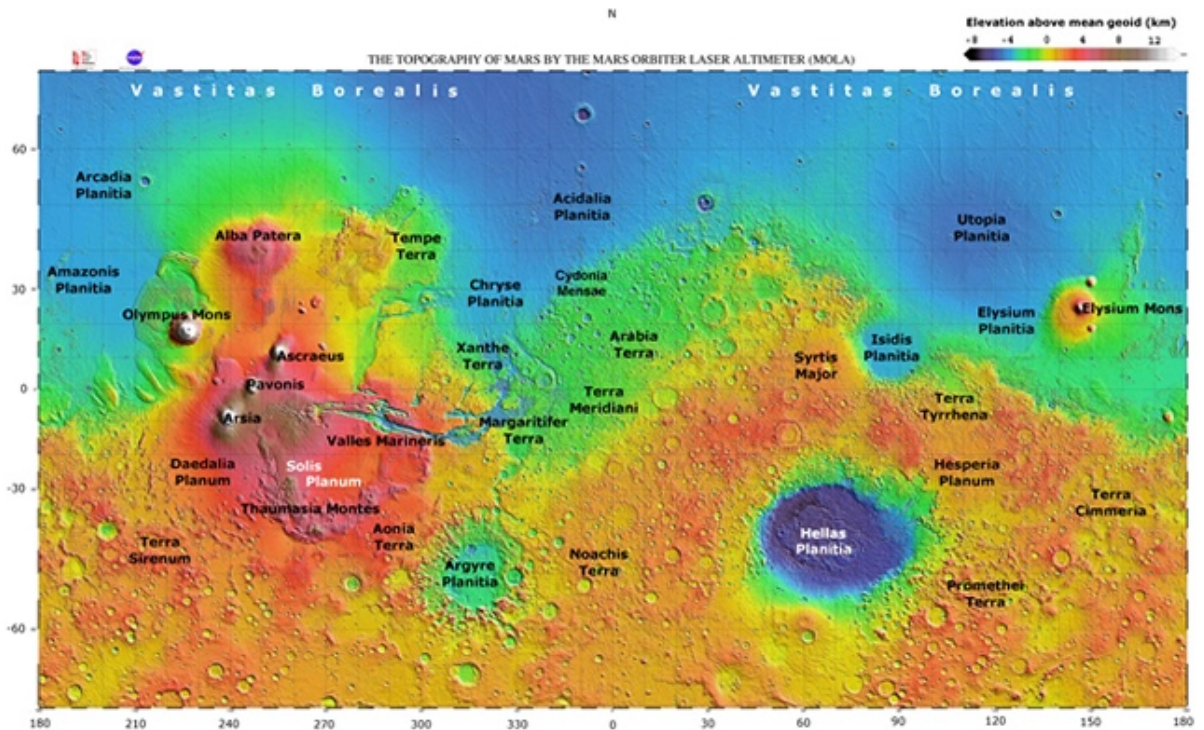
Ice is one of the most powerful and natural tools that can sculpt a planet. On Mars, ice may appear in various forms such as within the polar caps, debris-covered glaciers, and buried permafrost. In particular, ice is more common in the mid- to northern latitude regions and can even serve as paleoclimate indicators or windows to Mars' past climate (Lalich and Holt, 2017; Levy, Marchant, and Head, 2010). Today, seeing exposed ice on the surface of Mars is quite rare as it usually sublimates immediately instead of melting into its liquid form due to atmospheric conditions. As a consequence, ice on the Martian surface is unstable everywhere except on the polar ice caps. The Martian ice caps are primarily composed of water ice (North Polar Residual Ice Cap) and high-albedo solid CO<sub>2</sub> (South Polar Residual Ice Cap) and their evolution is highly dependent on the tilt or obliquity of

the planet, which consequently changes the size of the polar caps interannually (Kieffer et al. 1976; Malin and Edgett 2001; Hale et al. 2005; Byrne, 2009).

The presence of ground ice on Mars was first proposed in the 1970s on the basis of pioneering morphological interpretations of periglacial landforms (Sharp, 1974). The 1980s saw the first efforts to link distribution and morphology of patterned ground to buried ground ice from Viking imagery (Rossbacher and Judson, 1981, Squyres and Carr, 1986). With the launch of Mars Global Surveyor (MGS) and Mars Odyssey (MO), higher resolution imagery (MOC) combined with neutron data (GRS) as well as thermal inertia data (THEMIS) allowed for the first quantitative link to the presence of near-surface ground ice (Boynton et al., 2002, Mangold et al., 2004). The Phoenix mission, launched in 2008, then detected and confirmed a shallow ice table (5-18 cm depth) below patterned ground located in the landing site in the arctic region of Mars (Smith et al., 2009). Radar data from the SHARAD and MARSIS experiments was then key for the characterization of subsurface ice deposits, in particular their distribution and depth, down to a 10 m vertical resolution (Seu et al., 2007). The identification of subsurface ice is currently the focus of the Subsurface Water Ice Mapping on Mars (SWIM) team (Bramson et al., 2019; Putzig et al., 2019), and is for example the main goal of a planetary mission concept study for the 2023 decadal survey Mars Orbiter for Resources, Ices, and Environments (MORIE).

The use of geomorphic mapping of glacial and periglacial features from high resolution image data (from the Context Camera (CTX) and HiRISE onboard the Mars Reconnaissance Orbiter (MRO)) has become increasingly popular to identify buried excess ice. Significant ice deposits have thus been identified in Arcadia and Utopia Planitia (Stuurman et al., 2016, Bramson et al., 2019, Ramsdale et al., 2019). Additionally, an increasing body of evidence from high resolution imagery of relict periglacial landform morphology suggests that liquid water (wet periglaciation) occurred in recent periods of high obliquity.





**Figure 1.4.** Topographic map of Mars illustrated using colorized Mars Orbiter Laser Altimeter (MOLA) data. Utopia Planitia is labeled as the basin and/or lowlands situated on the northeast portion of the map in blue. Image credit: Christine M. Rodrigue, Department of Geography, California State University.

### 1.3.2 Patterned Ground Formation

Different patterned ground formations are major features of periglacial environments that are reflective of subsurface ice dynamics through geomorphologic, top-of-the-surface expressions. Over 50 years, patterned ground features have been observed with continuous, discontinuous, and sporadic types of permafrost suggesting further that there may be thermal controls within these zones (**Figure 1.3**). *Frost*, *mass movement*, *nivation*, and *wind activities* are major mechanical processes of the cold region environment (Thorn et al., 1992; Ballantyne, 2018). *Frost action* refers to the stress activity of frost shattering, frost cracking of permafrost, frost heave, and growth of needle ice. *Mass movement* involves gelifluction and frost creep activities, which redistribute sediments from higher to lower ground without substantial loss of mass. *Nivation* is the typical process of erosion and snowmelt transport beneath immobile patchy snow covers of sizable extent. Finally, *wind activity* is particularly strong toward the polar direction of frozen ground environments (Thorn et al., 1992; Ballantyne, 2018). By comparison, chemical weathering



is a minor stress activity, which possibly pulverizes clastic sediments in cold region environments (Ballantyne, 2018). Many aspects of periglacial processes, however, are inadequately understood.

There are various patterned ground features that have characteristic morphologies namely *stone circles*, *mud boils*, *polygons*, *solifluction lobes*, *nets*, and *stripes*. A compiled summary of patterned ground morphologies is summarized in **Table 1.1** and will be explored in detail in later chapters. In short, sorted patterned ground has been proposed to form through differential frost heave generated by recurrent freezing and thawing of moist, frost-susceptible soil containing abundant clasts (Washburn 1956; Ballantyne, 2013). Non-sorted patterned ground is also formed through differential frost heave of moist, frost-susceptible soil, but without concentration of clasts (Giles et al., 2017; Washburn, 1956; Hallet, 1990; Hutchinson, 1991; Ballantyne, 2013; Murton, 2013). The mechanisms of formation of various patterned ground features are further explored and expanded in detail in Chapter 3. Moreover, outstanding questions regarding their formation, evolution and spatial connectivity in a given periglacial landsystem setting are also addressed in the third chapter.

**Table 1.1.** Genetic classification of patterned ground morphology (modified from Washburn, 1973; Washburn, 1980).






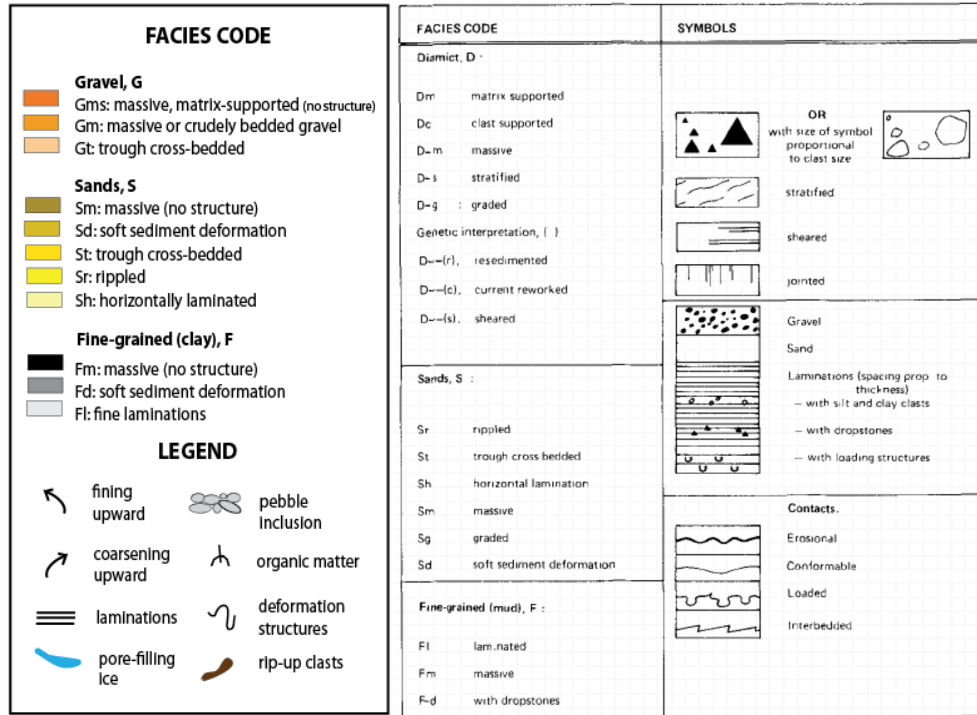
Type	Subtype	Shape	Occurrence	Size	Sediment composition	Vegetation	Notes
Stone Circles / circular ridges (mud boils)	Unsorted		- Flat areas - Singular or in groups	Height: 0.1-0.2m, Width: 0.3-1.0m Slightly domed	Silt-pebbles	Yes	They are active if the centre is bare.
	Sorted		- Flat areas - Singular or in groups	Height: 0.1-0.2m, Width: 0.3-1.0m Slightly domed	Silt-boulders (at the rim)	Irregular	They are inactive if the border stones have lichens.
Polygons	Unsorted		- Flat areas - Often have ponded centres	Height: 0.1-0.3m Width: 0.5 – 10m	Silt-gravel	Yes	There are different surficial classifications of polygons (i.e. high/low/flat centre) as well as subsurficial descriptors (i.e. ice-/sand-wedge, etc.)
	Sorted		- Flat and moderate slopes - Often have ponded centres	Height: 0.1-1.0m Width: 0.5 – 10m (from trough to centre)	Silt-boulders (at the rim)	Optional	
Steps (solifluction lobes)	Unsorted		- On slight slopes (5-15deg) - Grouped	Height: 0.3-0.6m Width: 1-3m Length: 8m	Stoney soils	Yes (downslope)	They develop from polygons, circles, or nets.
	Sorted		- On slight slopes (5-15deg) - Grouped	Height: 0.3-0.6m Width: 1-3m Length: 8m	Cobbles-boulders (at the downslope rim)	Yes (downslope)	
Nets	Unsorted		- Flat areas - Grouped	Height: 0.5m Width: 0.25-0.80m	Clay-gravel	Yes, thick	Intermediate shape between circles and polygons (e.g. earth hummocks)
	Sorted		- Flat areas - Grouped	Height: 0.5m Width: 0.25-0.80m	Gravel-cobbles (at the rim)	Yes	
Stripes	Unsorted		- On slight to moderate slopes (5-20deg) - Grouped	Width: 0.3-0.6m	Clay-cobbles	Yes	Can be evenly spaced or 3-5m apart.
	Sorted		- On slight to moderate slopes (5-20deg) - Grouped	Width: 0.3-0.6m	Clay-cobbles	Yes	

Photo credits: <sup>1</sup> Taken by Örn Óakarrson in South Iceland <sup>2</sup> Taken by 2016 UWO Arctic field team <sup>3</sup> [epod.usra.edu](http://epod.usra.edu) <sup>4</sup> Davies et al., 2020

## 1.4 Basic Principles of Periglacial Sedimentology and Cryofacies

### 1.4.1 Sedimentology and Facies Codes

Sedimentology is the study of the physical and chemical properties of sediment grains and sedimentary rocks in the context of the processes involved in their transport, deposition, and lithification. Sediment facies are mappable units of rock or sediment that have specified physical characteristics, composition, formation, and various other attributes. The Swiss geologist Amanz Gressly introduced the term facies in 1838 as he demonstrated regular lateral facies transitions along beds, which he interpreted to record spatially changing environmental conditions (Cross and Homewood, 1997). A variety of field measurements including sediment texture (grain size), clast size, lithology, shape, sedimentary structures (including soft sediment deformation structures), bed thicknesses, and the lateral continuity of individual units are acquired in order to create an accurate facies association and further architectural-element analysis (AEA; Miall, 1985). The facies code is structured with the first upper case letter representing the grain size: clay/silt (F), sand (S), gravel (G) and the second lower case letter representing primary and secondary sedimentary structures such as, massive (m), deformed (d), rippled (r), and laminated (l), etc.



**Figure 1.5.** Examples of facies codes for sedimentology applications used in this study (adapted from Andres et al., 2018 and Eyles et al., 1983).

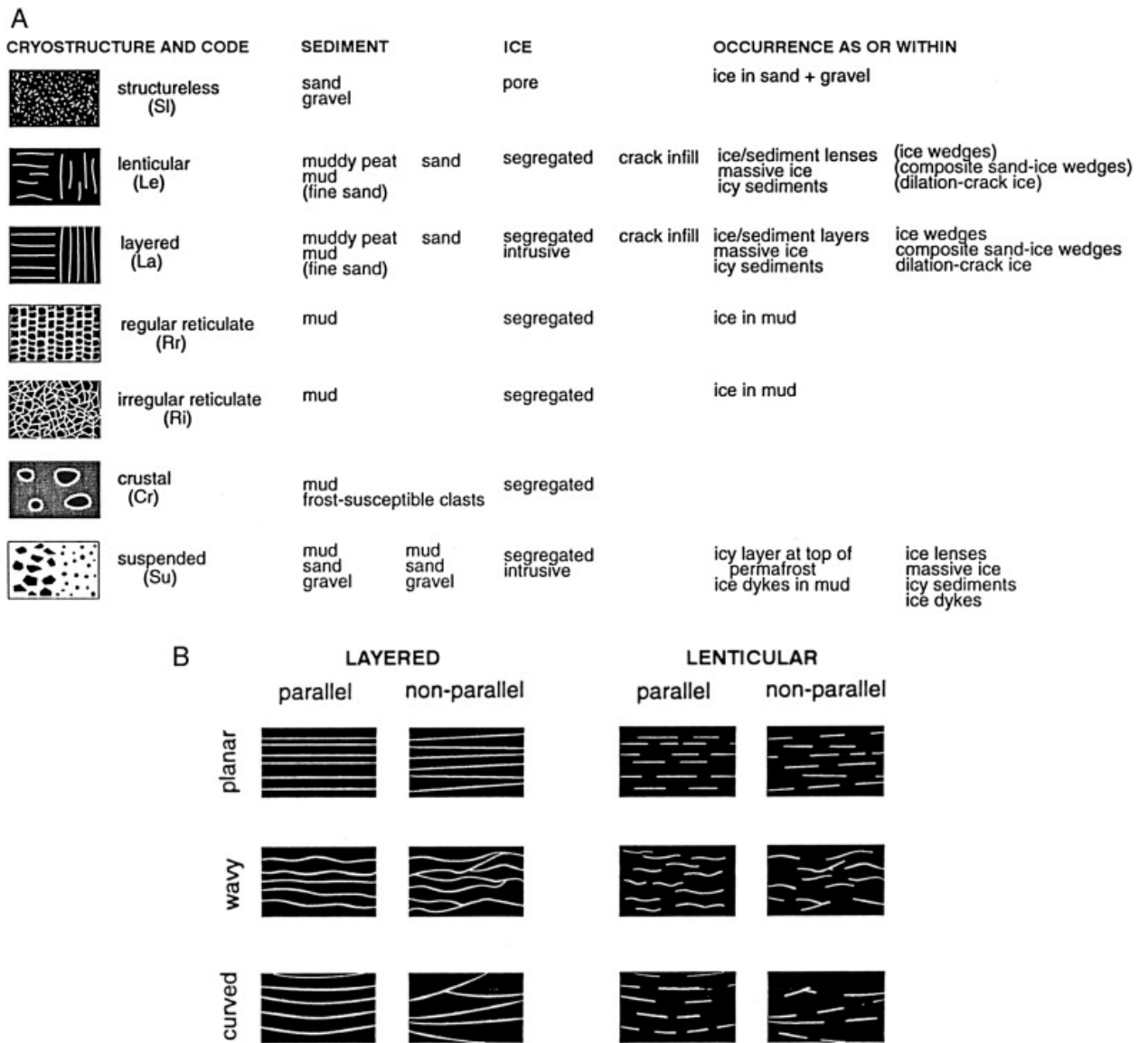
Although sedimentology is widely used in the fields of fluvial, glacial, and aeolian geomorphology, there is currently a gap and a need for the standardization of sedimentological facies codes that can be easily transferrable to any facies environment. More specifically, periglacial environments are dominated by subsurface processes and sediment transport through active layer freeze-thaw and the sedimentology and stratigraphic association of various periglacial landforms are currently lacking. The sedimentological facies techniques given by Eyles et al. (1983) are used and adapted to describe the excavation pits done in the Canadian High Arctic environment with the inclusion of other techniques that is solely used to describe ice within sediments as shown in **Figure 1.5**. In general, it is important to note that merging the two separate facies codes (i.e. sediment within ice vs. ice within sediment) would create a more efficient way of characterizing periglacial sedimentology.

## 1.4.2 Cryofacies

Cryostructures or structures within ice complexes were initially classified by Katasonov (1969) and Popov et al. (1974) in Northern Russia and adapted by Murton and French (1994) and Shur and Jorgenson (1998) in North America. A simplified version of these descriptions coined the term cryofacies basing observations and the structure of the code (Miall, 1985; Eyles et al., 1983) regarding soft sediments and sedimentary rocks. Cryofacies are observed with the naked eye and focus on the structure of ice within the pore spaces of sediment grains as well as their solidified architecture within the active layer of permafrost (**Figure 1.6**). There are currently seven outlined cryofacies descriptions namely, *SI: structureless*, *Le: lenticular*, *La: laminated*, *Re: regular reticulate*, *Ri: irregular reticulate*, *Cr: crustal*, and *Su: suspended* (French and Shur, 2010). All cryofacies are described in **Figure 1.6** with unique and distinguishable characteristic geometries of ice occurrences (adapted from French and Shur, 2010):

1. *'structureless' (SI)* — frozen sediment where ice is not visible and lacks cryostructures
2. *'lenticular' (Le)* — lens-like ice bodies that are described by inclination, thickness, length, shape and relationship to adjacent cryostructures
3. *'layered' (La)* — continuous bands of ice, sediment or a combination of both
4. *'regular-reticulate (R)* — a regular three-dimensional net-like structure of ice veins surrounding a block of structureless soil
5. *'irregular-reticulate' (Ri)* — an irregular three-dimensional net-like structure of ice veins surrounding a mud-rich block
6. *'crustal' (Cr)* — the ice crust or rim around a rock clast and gravel
7. *'suspended' (Su)* — grains, aggregates and rock clasts suspended in ice

Although cryofacies attempt to create classification within the sediment, these codes are hard to interpret due to the physical and thermal properties of ice as it rapidly melts out of sediment pore spaces. It is important to have a well-preserved periglacial facies body in order to maintain and conserve these structures for further sedimentological analysis and log correlation.



**Figure 1.6.** A North American classification of cryostructures proposed by Murton and French (1994). **(A)** Cryostructure types and codes with ice shown in white and sediment in black. **(B)** terms and illustrations to describe layered and lenticular cryostructures.

## 1.5 Remote Sensing as a Tool for Periglacial Mapping

### 1.5.1 Light Detection and Ranging (LiDAR)

There are different types of Light Detection and Ranging (LiDAR) methods and instruments that are used in remote sensing data acquisition, such as ground-based, airborne, and kinematic (mobile) scanners. LiDAR is a method for measuring distances by illuminating the target with laser light and measuring the reflection or the return of the pulse with a sensor at a particular GPS coordinate (Lim et al., 2003). Principally, differences in laser return times can then be used to make digital 3-D representations of the target (Liu, 2008; Kukko et al., 2020) based on a point cloud dataset. In the Canadian High Arctic, the speed and repeatability of LiDAR scanning corresponds to: (1) more area covered, which allows for study of the relationships between different morphologic features and processes, (2) time efficient, which allows researchers to do different experiments or measurements, and (3) the possibility of inter-season or year-on-year change detection, which allows for the determination of rates-of-change and the effects of small perturbations not captured in long-duration investigations.



**Figure 1.7. (A)** 2016 field team member (Michael Zanetti) traversing with the Akhka-R3 Kinematic Lidar System (KLS) in the Houghton Impact Structure on Devon Island in the Canadian High-Arctic **(B)** Prof. Antero Kukko traversing with the AkhkaR4DW Backpack mobile laser scanning system in the Mokka Fiord Valley on Axel Heiberg Island in the Canadian High-Arctic in 2018.

This study utilizes two generational types of kinematic backpack LiDAR's for data acquisition dubbed the (1) *Akhka-R3 Kinematic Lidar System (KLS)*, used in Devon Island, Nunavut, Canada (**Table 1.2**) and (2) *AkhkaR4DW Backpack mobile laser scanning system*, used in Axel Heiberg, Nunavut, Canada (Kukko et al., 2020; **Table 3**). These largely dense datasets were collected and assembled by Dr. Michael Zanetti (in 2017) Prof. Antero Kukko (in 2019) in collaboration with the Finnish Geospatial Research Institute, in Finland (**Figure 1.7**).

Due to their extreme ease in capturing comprehensive high-resolution 3D topographic data at a moderate walking speed, mobile LiDAR systems are frequently used for



3D mapping applications along various platforms. The *Akhka-R3* and *AkhkaR4DW* systems are used and overlain on top of geologic satellite imagery as well as lower resolution topography data in order to constrain area coverage and smaller-scale features. For example, the 2 cm LiDAR overlain on top of a 2 m ArcticDEM image footprint is used to map finer and smaller-scale features (i.e. pebbles) at smaller area coverage, while the ArcticDEM is used to provide context and overall larger coverage of the study areas.

**Table 1.2.** Akhka-R3 backpack Kinematic LiDAR System (KLS)

Sensor	Type/Function	Specific	Data rate
<b>NovAtel Flexpak6</b>	GNSS receiver	GPS, GLONASS	5Hz
<b>NovAtel GGG-703</b>	Antenna		
<b>NovAtel UIMU</b>	UIMU – Inertial system	FOG, MEMS	200Hz
<b>Trimble R10</b>	GNSS base station	GPS, GLONASS	5Hz
<b>Riegl VUX-1HA</b>	laser scanner	1550 nm, pulse	1017kHz
<b>FLIR Ladybug5+</b>	Camera	panoramic	0.5Hz

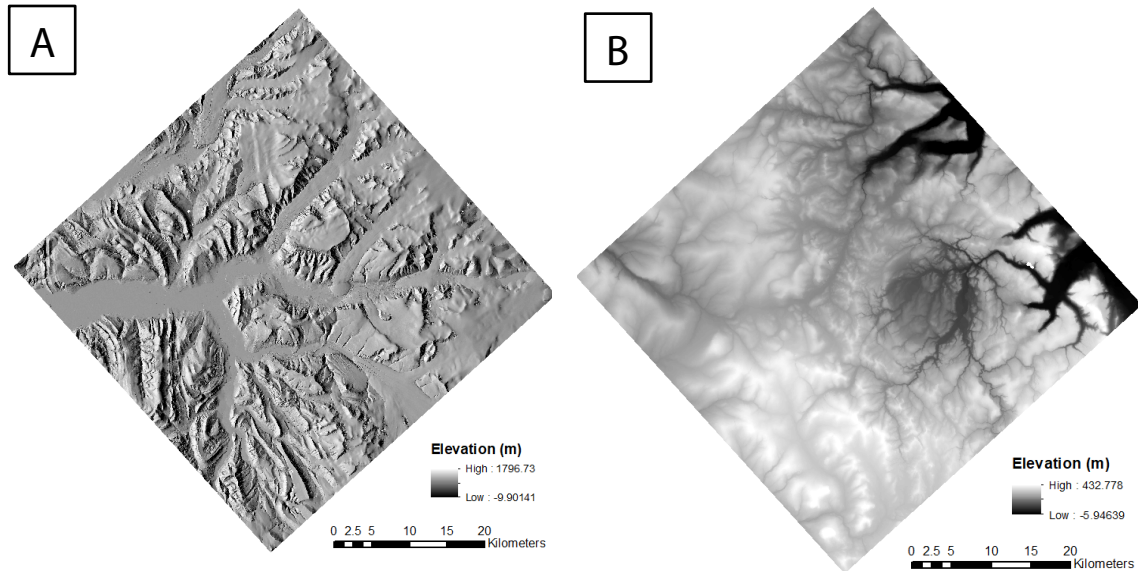
**Table 1.3.** AkhkaR4DW backpack mobile laser scanning system components

Sensor	Type/Function	Specific	Data rate
<b>NovAtel Pwrpak7</b>	GNSS receiver	GPS, GLONASS	5Hz
<b>NovAtel GNSS-850</b>	Antenna		
<b>NovAtel ISA-100C</b>	IMU	FOG, MEMS	200Hz
<b>Trimble R10</b>	GNSS base station	GPS, GLONASS	5Hz
<b>Riegl VUX-1HA</b>	laser scanner	1550 nm, pulse	1017kHz
<b>Riegl miniVUX-1UAV</b>	laser scanner	905 nm, pulse	100kHz
<b>FLIR Ladybug5+</b>	Camera	panoramic	0.5Hz

### 1.5.2 Arctic DEM

The ArcticDEM project is a response to the need for high quality digital elevation model (DEM) data in inaccessible, remote locations in northern latitude regions, in particular the arctic polar circle. ArcticDEM datasets also answer to the lack of availability of technology to process big data and the need for accurate measurement of topographic change. Specifically, ArcticDEM strips are files that correspond to the overlapping area of the input stereopair image swaths as they are collected by the *DigitalGlobe* constellation of polar-orbiting satellites. ArcticDEM strip dimensions vary according to the satellite sensor that acquired the images and the off-nadir angle of collection. Most strips range from 16-18 km in width, and 110-120 km in length (Porter et al., 2018). Additionally, the majority of ArcticDEM data is generated from the panchromatic bands of the *WorldView-1*,

*WorldView-2*, and *WorldView-3* satellites. A small percentage of data is also generated from the *GeoEye-1* satellite sensor. In total, ArcticDEM strips have a resolution of 2m/pixel, which is an unprecedented scale of resolution amongst DEM datasets worldwide (**Figure 1.8**).



**Figure 1.8.** ArcticDEM (A) hillshaded 2m-DEM of Axel Heiberg at 79.16°, -90.23° (B) raw 2m-DEM of Haughton Crater at 75.37°, -89.53°.

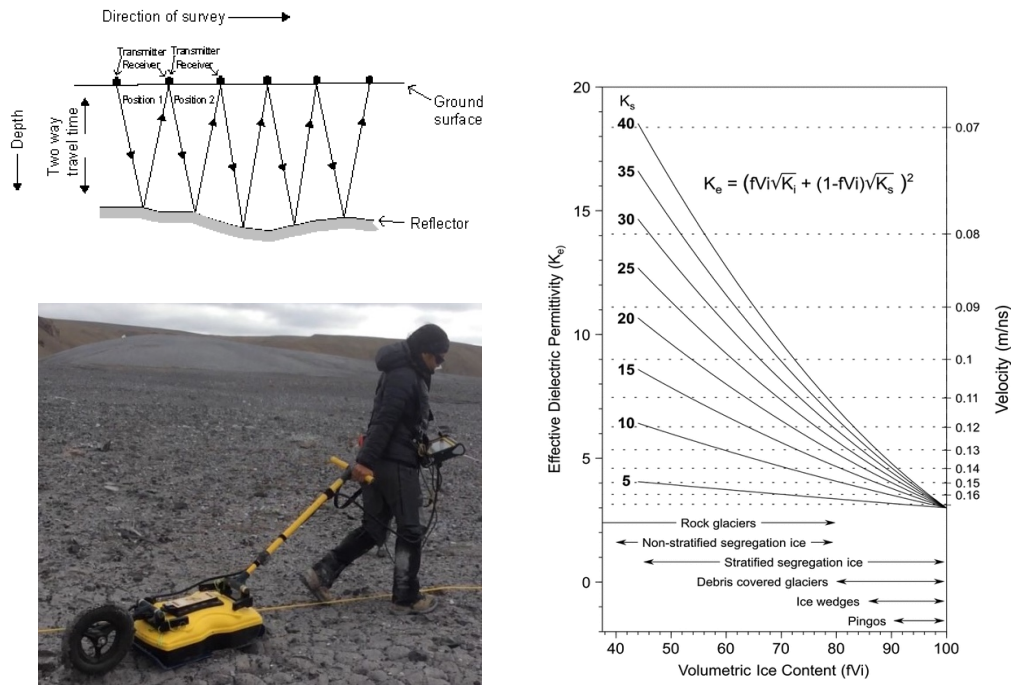
ArcticDEM is one of the only data sets that allows users to access high level data in an unrestricted manner. In the present, ArcticDEM proves to be the best, free, and accessible digital elevation model data source for Arctic studies.

## 1.6 Ground Penetrating Radar in Periglacial Environments

### 1.6.1 Principles of Ground Penetrating Radar (GPR)

Ground penetrating radar (GPR) is a geophysical technique that allows high-resolution and non-destructive stratigraphic imaging of the subsurface. The GPR method records the two-way travel time of electromagnetic (EM) waves reflected at boundaries between subsurface layers with contrasting relative permittivity (**Figure 1.9**). Dielectric contrasts develop due to variations in sediment grain size, water content, and mineral composition (Jol, 2008). Moreover, GPR can optimally be used to look for signs of past or present water

in the subsurface. Specifically, this can be done by studying geological formations made by water or finding signs of ice or brines in the subsurface with contrasting dielectric properties. GPR studies in periglacial environments include fieldwork data collection, data processing, and the generation of signal processing algorithms to model the architecture of ice in permafrosted ground.

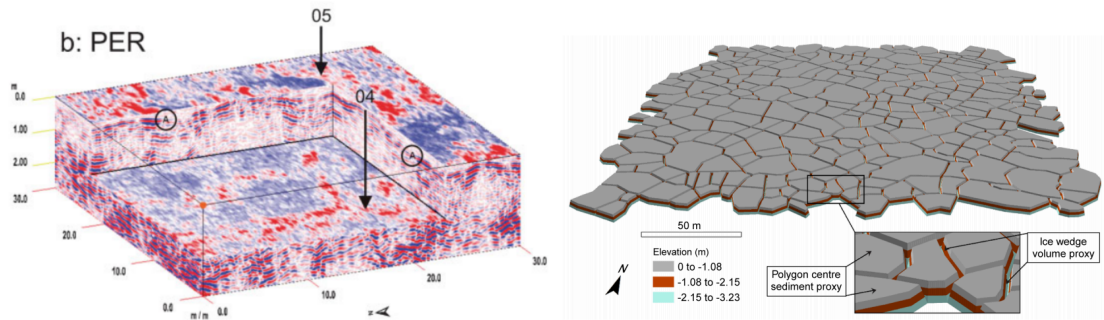


**Figure 1.9.** Concept of GPR survey setup and image of the Sensors and Software Noggin™ 250MHz ground penetrating radar (left). Dielectric permittivity calculations for various types of ground ice in periglacial environments (from Thompson et al., 2012).

### 1.6.2 3D-GPR Modelling of Ground Ice Systems

Three-dimensional ground-penetrating radar (3D GPR) is an up and coming novel method to model, quantify, compile, and visualize GPR radargram datasets. Studies using 3D GPR have been able to delineate subsurface ice networks such as ice wedges, active layer depths, subsurface ice distribution, etc. with high fidelity (Munroe et al., 2007; Ulrich et al., 2014; Couture and Pollard, 1998; Schennen et al., 2015). When supplemented by analysis of soil cores and/or other geophysical techniques, 3D GPR offers considerable potential for imaging, interpreting and 3D mapping of near-surface soil and ice structures in permafrost

environments. Along with these capabilities, 3D GPR enables the calculation of the potential total cubic volume and water content given a certain area.



**Figure 1.10.** 3D GPR cube model of Footprint Lake to image ice-wedge networks in Lake Manitoba, Canada (left; Munroe et al., 2007). 3D Model of ice wedge volume estimates for a High Arctic polar desert environment, Fosheim Peninsula, Ellesmere Island (right; Bernard-Grand’Maison and Pollard; 2018).

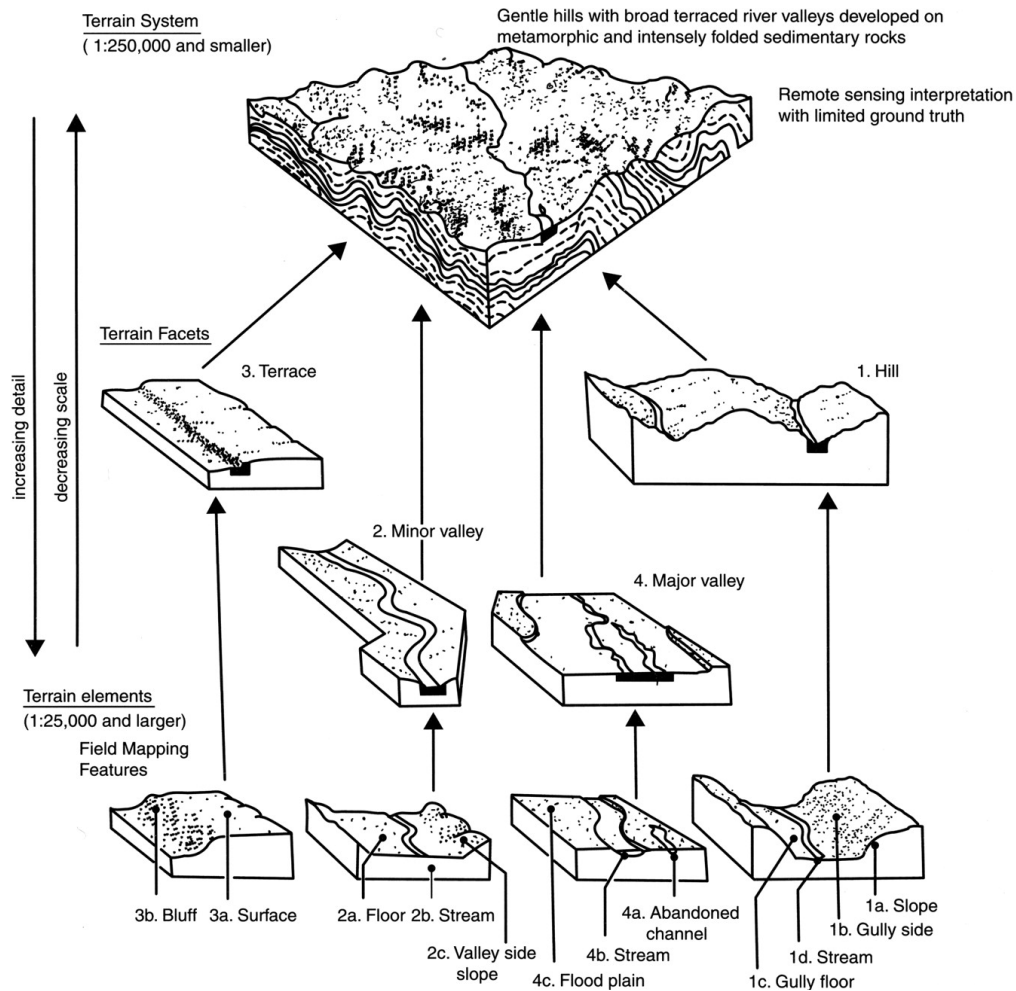
Several studies have demonstrated the potential of GPR for exploring permafrost environments, e.g., to estimate active-layer thickness (Arcone et al., 1998), to detect ground-ice bodies and ice layers (Yoshikawa et al., 2006; Brandt et al., 2007; De Pascale et al., 2008; Schwamborn et al., 2008), or to image specific periglacial morphologies (Doolittle et al., 1992; Moorman et al., 2003). Although in many different GPR applications (i.e. in archaeology, sedimentology, groundwater contamination), the benefits of 3D data collection and analysis have been acknowledged (e.g., Leckebusch, 2003; Grasmück et al., 2004; Tronicke et al., 2006; Bradford and Wu, 2007; Harper et al., 2010; Schmelzbach et al., 2011; Böniger and Tronicke, 2012), such 3D strategies have not yet been fully exploited in permafrost environments. Up to now, only a limited number of case studies have been published. For example, Brosten et al. (2009) investigate active-layer characteristics beneath arctic streams using 3D GPR, whereas Munroe et al. (2007) study the near-surface geometry of ice-wedge polygons also using a 3D exploration strategy. GPR data are also a valuable component when correlating geologic and geomorphic patterns within a given spatial distribution. GPR can be used as a powerful tool to show the reflection of the top-of-the-surface expression in the subsurface as the characteristic landscape evolves.

## 1.7 Landsystem Analysis

### 1.7.1 The Development of the Landsystem Concept

Landsystem analysis is a methodology of evaluating and classifying terrain based on the documentation of landforms and sediments and an understanding of the depositional processes that created them (Cooke and Doornkamp, 1990). Landsystem analysis has developed over the past 40 years as a commonly applied methodology particularly in glacial landscapes to understand process-form relationships and the distribution of sediments where there are several confounding components involved (Evans and Twigg 2002). The value of this method lies not only in its ability to classify and simplify complex terrain (Christian 1958; Evans 2003), but also in its application to the understanding and delineating subsurface deposits (Cooke and Doornkamp, 1990; Eyles, 1983). Landsystems analysis was first popularized in environmental assessment as a method of evaluating the land use of large areas of undeveloped land with Commonwealth Scientific and Industrial Research Organization (CSIRO, Australia) (Christian, 1958; Cooke and Doornkamp, 1990; Evans, 2003). The landsystem survey was used to document, classify, and map large areas of land which lacked scientific information to determine potential agricultural usage (Christian, 1958).

Landsystem analysis (**Figure 1.11**) is a hierarchical method which classifies a region into areas that contain a recurring pattern of topography, landform, sediment and vegetation known as a landsystem, which represents a natural unit (Evans, 2003). To be considered a landsystem it must have internal consistency while being distinct and recognizable from the surrounding systems (Christian, 1958; Eyles, 1983a). A landsystem is further divided into land units, also referred to as system tracts, which are components of the land surface that have similar physical attributes and were created by similar depositional processes (Christian, 1958; Cooke and Doornkamp, 1990). Land units are further classified into elements which represent a single uniform component of the landscape (Christian, 1958; Eyles, 1983).



**Figure 1.11** A hierarchal overview of landsystem terrain elements. This diagram illustrates the relationship between different system tracts: (1) the terrain system, (2) terrain facet, and (3) terrain element (Cooke & Doornkamp 1990).

### 1.7.2 Utility of Landsystem Analysis in Periglacial Environments

Landsystem analysis has been successfully employed as a methodology for understanding the process-form relationships to determine the genetic origins of sediment (Evans and Twigg, 2002). Understanding the temporal and the spatial evolution of ice-rich landscapes is key in order to predict the potential distribution of sediments in conjunction with freeze-thaw processes (French, 2017). The value of the landsystem methodology is in its potential use in areas of permafrost, such as the Canadian High Arctic Archipelago, where it can serve as a tool for mapping and modelling of the subsurface. It is most easily applied to surficial deposits and to the interpretation of deposits created by active freeze-thaw

mechanics, although it can be applied to more deeply buried deposits through the use of subsurface investigative techniques and cryostratigraphy (French and Shur, 2010). Successful interpretation of periglacial deposits is reliant on an appropriate understanding of the characteristics of modern frozen ground (i.e. depth variation, thermal attributes, etc.)

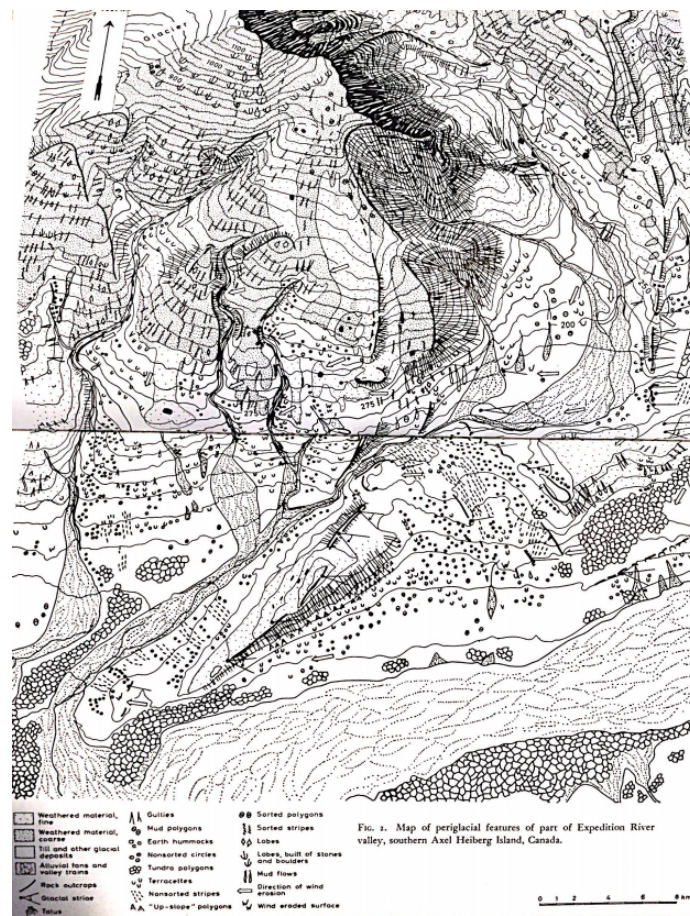
Landsystem analysis is primarily a qualitative methodology where classifications are determined by the expertise of the individual researcher; this is exemplified by the multiple interpretations of similar landsystems that are made by different researchers (i.e. differentiation in zonation of the subsurface ice interface from gully/levee systems to gully-polygon troughs). Creating parameterization or requiring additional input of quantitative data to landsystems analysis may reduce the range of interpretations made by researchers. Landsystem analysis combines sedimentology, architectural analysis, remote sensing, and geologic mapping. The landsystems approach is a holistic method of studying periglacial and landscape history that (i) makes inferences using the full suite of landform–sediment assemblages that constitute a landscape (Chapter 2), and (ii) is supported by process–form models established at active environments (Chapter 3).

Recent research at periglacial regions has further emphasized the importance of incorporating morphological, sedimentological and structural evidence into interpretation of ice processes (Giles et al., 2017). This allows for the inclusion of factors such as grain size, rheology, thermal regime, and geometry into the examination and interpretation of the processes occurring underground. Fieldwork is an important part of the landsystems analysis process and provides significant information on geomorphological and sedimentological characteristics of the significant landforms such as patterned ground. The collection of sedimentological evidence is critical to identify landsystems that can model the subsurface distribution of sediments. Beyond the physical collection of data, fieldwork also allows for contextualization of aerial imagery, providing a different perspective on DEMs and aerial images.

### *Expedition Fiord, Axel Heiberg Island*



Historically, terrestrial landsystem analysis has been a common practice in the geosciences when exploring the paleogeography of a certain region. In the Canadian High Arctic, localized areas have only been mapped with limited detail to the limited access and coverage of the field. For example, the earliest periglacial landsystem analysis model in Axel Heiberg Island can be traced back to Expedition Fiord (Rudberg, 1983; **Figure 1.12**), which outlines the various patterned ground morphologies including their lateral variability, geometry, and composition in a ~30 km wide region.



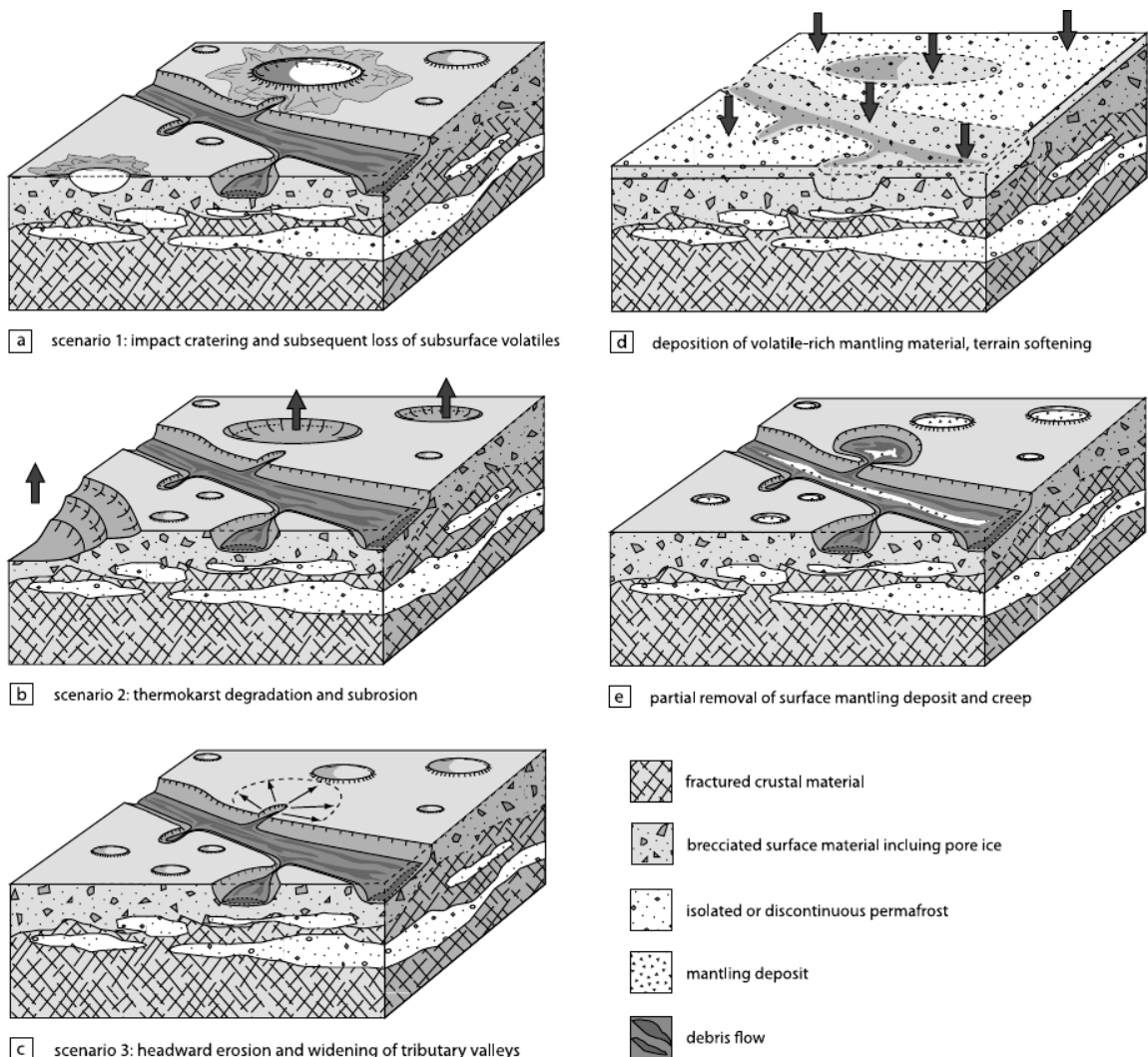
**Figure 1.12.** First geomorphologic map of Axel Heiberg. Field sketch of the north-facing Expedition Fiord landsystem (Rudberg, 1983).

### *Deuteronilus Mensae, Mars*

Planetary landsystem analyses have been prevalent in the literature most distinctly, looking at relationships and contrasts between surface units in a lineated valley fill (LVF) feature



at the Martian dichotomy boundary in Deuteronilus Mensae, Mars. Currently, there are arguments leading to a glacial environment interpretation known from terrestrial glacial systems observed in, the Canadian High Arctic Archipelago such as Ellesmere Island and other North Canadian High Arctic islands (Van Gasselt et al., 2010). The LVF in Deuteronilus Mensae is one among numerous other more or less elliptical or elongated closed depressions that are commonly observed in the “fretted” terrain, which show no distinct source area (Carr, 2001). Characteristic for most of these morphologic LVFs is an infill composed of bright and dark lineated material with either a smooth or knobby surface texture. Descriptions and observations of primary and secondary structures such as subparallel lineations and contortion patterns as well as crevasses-like fracture patterns are evident, as well as flow of different materials that roughly resemble surfaces of terrestrial valley glaciers known from terrestrial polar desert regions in the Arctic lacking any vegetation. In order to understand these various observation levels, different components of the landsystem (i.e. system tracts) need to be established to generate a step-wise landscape progression that could infer processes that may be happening on a larger scale (**Figure 1.13**).



**Figure 1.13** Landscape model for depression formation in Deuteronilus Mensae; illustrate initial formation by either (A) impact cratering, or (B) thermokarst degradation and subsequent erosion, or (C) headward erosion by thaw slumping. (D) After formation of the main depression a volatile-rich layer might have been deposited from the atmosphere at midlatitudes in the course of obliquity changes. (E) Here the atmospheric deposit has been substantially eroded, mixed with older material and moves downslope toward the North (Van Gasselt et al., 2010).

## 1.8 Chapter Summary

This chapter introduces the principle concepts of periglacial geology that have significant implications to the study of landsystem analysis in the Canadian High Arctic Archipelago

and Mars. These two planetary bodies share analogous geomorphologic features of patterned ground that encompasses mechanical processes, geothermal regimes, and climatic controls of permafrost or frozen ground. The periglacial environment is relatively well-defined on Earth in comparison to Mars as this frozen ground interface has not been explored using tools such fieldwork, sedimentology, and ground-truthing techniques along with a variety of remote sensing methods. LiDAR, Digital Elevation Models (DEM), optical satellite imagery and ground penetrating radar (GPR) are used to further expand on the processes dominating periglacial patterned ground formation in order to define the components and interactions of a novel periglacial landsystem model.

A periglacial landsystem analysis is a hierarchical methodology of evaluating and classifying permafrost-influenced terrain based on the identification and documentation of landforms and sediments and an understanding of the depositional processes that created them in frozen ground conditions. The Canadian High Arctic provides two examples of these periglacial landsystems namely in Axel Heiberg Island and Devon Island. One half of Canada's land surface is underlain by permafrost (Permafrost - Open Government Portal, 1978) and the Canadian High Arctic lies within the continuous permafrost zone with ground ice content in the upper 10-20 m of 10-20%. These two study areas will be respectively examined in Chapter 2 and Chapter 3.

## 1.9 Introduction to Thesis

This thesis aims to provide some insight regarding the interactions of Arctic periglacial landsystems and the various types of patterned ground using fieldwork measurements, sedimentology, geographic information system (GIS) mapping, geophysical methods, and remote sensing techniques on topographical datasets. The first body chapter, Chapter 2, focuses on breaking down the periglacial landsystem into its components using sedimentology and GPR to better understand ice-wedge polygons in Axel Heiberg Island, NU. The unique study region in Strand Fiord on the western portion of the island houses an alluvial "fossil" fan that has been dominated by periglacial processes in a desert-like environment. With polygonal networks covering the surface of the Strand Fiord Fossil Fan, the sizes and geometries of primary, secondary, and tertiary cracking in these polygons are

also explored in great detail including the confounding factors that may be affecting their formation and evolution (i.e. slope, grain size distribution, ice wedge presence, etc.). Chapter 3 introduces a quantitative analysis of patterned ground geomorphology using hyper-resolution LiDAR in Devon Island, NU. In the Houghton River Valley, Houghton Impact Structure, there are a variety of patterned ground that occur at a small and constrained locale. This method uses the kernel density estimation (KDE) algorithm as well as cumulative sorting plots in order to quantify the geomorphologic differences in 4 types of patterned ground: (1) stone circles (including asymmetric/crenulated closed ridges), (2) mud boils or frost-shattered hummocks, (3) stone stripes, and (4) polygons. This thesis therefore contributes to the overall dynamics and inventory of permafrost landforms in the Canadian High Arctic Archipelago, as well as its response to ongoing climate change. It not only investigates the impacts of the rapidly melting ground ice, but also proposes planetary analogue applications that may serve useful in future mission concepts regarding water-ice in-situ resource utilization (ISRU).

## 1.10 References

- Andres, C., Eyles, C., Jara, H. and Narro-Pérez, R., 2018. Sedimentological Analysis of Paleolake Jircacocha, Cojup Valley, Cordillera Blanca, Peru. *Revista de Glaciares y Ecosistemas de Montaña*, (5), pp.1-18.
- Ballantyne, C.K., 2018. *Periglacial geomorphology*. John Wiley & Sons.
- Ballantyne C.K. 2013. Patterned ground. In: Elias S.A. & Mock C.J. (eds) *Encyclopedia of Quaternary Science*. 2nd edn. Elsevier, Amsterdam, 3, 452–463.
- Bigras C, Bilz M, Grattan DW, Gruchy C. 1995. Erosion of the geodetic hills fossil forest, Axel Heiberg Island, Northwest Territories. *Arctic* 48(4): 342–353.
- Boike, J. and Yoshikawa, K., 2003. Mapping of periglacial geomorphology using kite/balloon aerial photography. *Permafrost and periglacial processes*, 14(1), pp.81-85.
- Boynton, W.V., Feldman, W.C., Squyres, S.W., Prettyman, T.H., Brückner, J., Evans, L.G., Reedy, R.C., Starr, R., Arnold, J.R., Drake, D.M. and Englert, P.A.J., 2002. Distribution of hydrogen in the near surface of Mars: Evidence for subsurface ice deposits. *science*, 297(5578), pp.81-85.
- Bramson, E.I., Bain, Z.M., Putzig, N.E., Morgan, G.A., Mastrogiuseppe, M., Perry, M.R. and Smith, I.B., 2019, March. Mars Subsurface Water Ice Mapping (SWIM): Radar Subsurface Reflectors. AM. In *Lunar and Planetary Science Conference (Vol. 50)*.
- Brown, R.J., 1970. *Permafrost in Canada: its influence on northern development*. University of Toronto Press.
- Brown, R.J.E., 1960. The distribution of permafrost and its relation to air temperature in Canada and the USSR. *Arctic*, 13(3), pp.163-177.
- Burn, C.R. and Kokelj, S.V., 2009. The environment and permafrost of the Mackenzie Delta area. *Permafrost and Periglacial Processes*, 20(2), pp.83-105.
- Byrne, S., 2009. The polar deposits of Mars. *Annual Review of Earth and Planetary Sciences*, 37.
- Callaghan, T.V., Björn, L.O., Chapin Iii, F.S., Chernov, Y., Christensen, T.R., Huntley,

- B., Ims, R., Johansson, M., Riedlinger, D.J., Jonasson, S. and Matveyeva, N., 2005. Arctic tundra and polar desert ecosystems. Arctic climate impact assessment, 1, pp.243-352.
- Carr, M.H., 2001. Mars Global Surveyor observations of Martian fretted terrain. Journal of Geophysical Research: Planets, 106(E10), pp.23571-23593.
- Christian, C.S., 1958. The concept of land units and land systems, in: Proceedings of the Ninth Pacific Science Congress, 20. pp. 74–81.
- Cooke, R.V. and Doornkamp, J.C., 1990. Geomorphology in environmental management: a new introduction. Oxford University Press (OUP).
- Couture, N.J. and Pollard, W.H., 1998, June. An assessment of ground ice volume near Eureka, Northwest Territories. In Permafrost–Seventh International Conference (Proceedings) (Vol. 55, pp. 195-200).
- Creameens, D.L., Darmody, R.G. and George, S.E., 2005. Upper slope landforms and age of bedrock exposures in the St. Francois Mountains, Missouri: A comparison to relict periglacial features in the Appalachian Plateau of West Virginia. Geomorphology, 70(1-2), pp.71-84.
- Cross, T.A. and Homewood, P.W., 1997. Amans Gressly's role in founding modern stratigraphy. Geological Society of America Bulletin, 109(12), pp.1617-1630.
- Davies, Bethan, et al. "Periglacial Environments." AntarcticGlaciers.org, 01 June 2020, [www.antarcticglaciers.org/glacial-geology/glacial-landform/antarctic-periglacial-environments/](http://www.antarcticglaciers.org/glacial-geology/glacial-landform/antarctic-periglacial-environments/).
- Douglas R. J. W. 1970. Introduction. In Geology and economic minerals of Canada. Geological Survey of Canada Economic Geology Report 1, edited by Douglas R. J. W. Ottawa: Geological Survey of Canada. pp. 2–8.
- Embleton, C. and King, C.A.M., 1968. Glacial and periglacial geomorphology.
- Embry, A. and Beauchamp, B., 2008. Sverdrup basin. Sedimentary basins of the world, 5, pp.451-471.
- Evans, D.J. and Twigg, D.R., 2002. The active temperate glacial landsystem: a model based on Breiðamerkurjökull and Fjallsjökull, Iceland. Quaternary science reviews, 21(20-22), pp.2143-2177.
- Evans, D.J.A., 2003. Introduction to Glacial Landsystems, in: Evans, D.J.A. (Ed.),

- Glacial Landystems. Hodder Arnold, London, p. 531.
- Eyles, N., 1983. Glacial geology: a landystems approach. In *Glacial geology* (pp. 1-18). Pergamon.
- Eyles, N., Eyles, C.H. and Miall, A.D., 1983. Lithofacies types and vertical profile models; an alternative approach to the description and environmental interpretation of glacial diamict and diamictite sequences. *Sedimentology*, 30(3), pp.393-410.
- French, H. and Shur, Y., 2010. The principles of cryostratigraphy. *Earth-Science Reviews*, 101(3-4), pp.190-206.
- French, H.M., 2017. *The periglacial environment*. John Wiley & Sons.
- Frisch T. and Thorsteinsson R. 1978. Haughton astrobleme: A mid-Cenozoic impact crater, Devon Island, Canadian Arctic Archipelago. *Arctic* 31:108–124
- Gallagher, D., Bergstrom, J., Day, J., Martin, B., Reed, T., Spuhler, P., Streetman, S. and Tommeraasen, M., 2005, August. Overview of the optical design and performance of the high resolution science imaging experiment (HiRISE). In *Current Developments in Lens Design and Optical Engineering VI* (Vol. 5874, p. 58740K). International Society for Optics and Photonics.
- Giles, D.P., Griffiths, J.S., Evans, D.J.A. and Murton, J.B., 2017. Geomorphological framework: glacial and periglacial sediments, structures and landforms. *Geological Society, London, Engineering Geology Special Publications*, 28(1), pp.59-368.
- Greiner H. R. 1963. Haughton Dome and area southwest of ThomasLee Inlet. In *Geology of the north–central part of the Arctic Archipelago, Northwest Territories (Operation Franklin)*, Geological Survey of Canada Memoir 320, edited by Fortier Y. O., Blackadar R. G., Glenister B. F., Greiner H. R., McLaren D. J., McMillan N. J., Norris A. W., Roots E. F., Souther J. G., and Thorsteinsson R. Ottawa: Geological Survey of Canada. pp.208–216
- Grieve R. A. F. 1988. The Haughton impact structure: Summary and synthesis of the results of the HISS project. *Meteoritics* 23:249–254.
- Hale AS, Bass DS, Tamppari LK. 2005. Monitoring the perennial martian northern polar cap with MGS MOC. *Icarus* 174:502–12

- Hallet B. 1990. Spatial self-organization in geomorphology: from periodic bedforms and patterned ground to scale-invariant topography. *Earth-Science Reviews*, 29, 57–75, [https://doi.org/10.1016/0012-8252\(0\)90028-T](https://doi.org/10.1016/0012-8252(0)90028-T)
- Harrington, E.M., Shaposhnikova, M., Neish, C.D., Tornabene, L.L., Osinski, G.R., Choe, B.H. and Zanetti, M., 2019. A Polarimetric SAR and Multispectral Remote Sensing Approach for Mapping Salt Diapirs: Axel Heiberg Island, NU, Canada. *Canadian Journal of Remote Sensing*, 45(1), pp.54-72.
- Harris, S.A., 1982. Identification of permafrost zones using selected permafrost landforms. In *Proc. 4th Canadian Permafrost Conf., Alberta* (pp. 49-58).
- Haughton S. H. 1860a. On the fossils brought home from the Arctic regions in 1859, by Captain Sir F. L. M'Clintock. *Journal of the Royal Dublin Society* 3:53–58
- Haughton S. H. 1860b. Geological account of the Arctic Archipelago, drawn up from the specimens collected by Captain F. L. M'Clintock, R. N. from 1849 to 1859. *Journal of the Geological Society of Dublin* 8:196–213
- Heldmann, J.L., Pollard, W.H., McKay, C.P., Andersen, D.T. and Toon, O.B., 2005. Annual development cycle of an icing deposit and associated perennial spring activity on Axel Heiberg Island, Canadian High Arctic. *Arctic, Antarctic, and Alpine Research*, 37(1), pp.127-135.
- Hjort, J. and Luoto, M., 2006. Modelling patterned ground distribution in Finnish Lapland: an integration of topographical, ground and remote sensing information. *Geografiska Annaler: Series A, Physical Geography*, 88(1), pp.19-29.
- Hund, A.J. ed., 2014. *Antarctica and the Arctic Circle: A Geographic Encyclopedia of the Earth's Polar Regions* [2 volumes]. ABC-CLIO.
- Hutchinson J.N. 1991. Periglacial and slope processes. In: Forster A., Culshaw M.G., Cripps J.C. & Moon C.F. (eds) *Quaternary Engineering Geology*. Geological Society, London, *Engineering Geology Special Publications*, 7, 283–331, <https://doi.org/10.1144/gsl.eng.1991.007.01.27>
- IPCC, 2019: Summary for Policymakers. In: *IPCC Special Report on the Ocean and Cryosphere in a Changing Climate* [H.-O. Pörtner, D.C. Roberts, V. Masson-Delmotte, P. Zhai, M. Tignor, E. Poloczanska, K. Mintenbeck, A. Alegría, M. Nicolai, A. Okem, J. Petzold, B. Rama, N.M. Weyer (eds.)]. In press.



- Jackson, M.P.A. and Harrison, J.C., 2006. An allochthonous salt canopy on Axel Heiberg Island, Sverdrup Basin, Arctic Canada. *Geology*, 34(12), pp.1045-1048.
- Jol, H.M. ed., 2008. *Ground penetrating radar theory and applications*. Elsevier.
- Katasonov, E., 1969. The typical features of cryogenic eluvium on slopes. *Biuletyn Peryglacjalny*, pp.11-14.
- Karte J. 1979. Raumliche Abgrenzung und regionale Differenzierung des Periglaziars. *Bochumer Geographische Arbeiten*, 35 (211 pp.).
- Karte J, Liedtke H. 1981. The theoretical and practical definition of the term 'periglacial' in its geographical and geological meaning. *Biuletyn Peryglacjalny*, 28:123±135
- King, R.B., 1971. Boulder polygons and stripes in the Cairngorm Mountains, Scotland. *Journal of Glaciology*, 10(60), pp.375-386.
- Kessler, M.A., Murray, A.B., Werner, B.T. and Hallet, B., 2001. A model for sorted circles as self-organized patterns. *Journal of Geophysical Research: Solid Earth*, 106(B7), pp.13287-13306.
- Kukko, A., Kaartinen, H., Osinski, G. and Hyypä, J., 2020. MODELLING PERMAFROST TERRAIN USING KINEMATIC, DUAL-WAVELENGTH LASER SCANNING. *ISPRS Annals of the Photogrammetry, Remote Sensing and Spatial Information Sciences*, 2, pp.749-756.
- Lachenbruch, A.H., 1962. *Mechanics of thermal contraction cracks and ice-wedge polygons in permafrost* (Vol. 70). Geological Society of America.
- Lalich, D.E. and Holt, J.W., 2017. New Martian climate constraints from radar reflectivity within the north polar layered deposits. *Geophysical Research Letters*, 44(2), pp.657-664.
- Leslie, D.M. and McGlone, M.S., 1973. Relict periglacial landforms at clarks junction, Otago. *New Zealand Journal of Geology and Geophysics*, 16(3), pp.575-583.
- Lev, A. and King, R.H., 1999. Spatial variation of soil development in a high arctic soil landscape: Truelove Lowland, Devon Island, Nunavut, Canada. *Permafrost and Periglacial Processes*, 10(3), pp.289-307.
- Levy, J.S., Marchant, D.R. and Head, J.W., 2010. Thermal contraction crack polygons on Mars: A synthesis from HiRISE, Phoenix, and terrestrial analog studies. *Icarus*, 206(1), pp.229-252.

- Lim, K., Treitz, P., Wulder, M., St-Onge, B. and Flood, M., 2003. LiDAR remote sensing of forest structure. *Progress in physical geography*, 27(1), pp.88-106.
- Liu, X., 2008. Airborne LiDAR for DEM generation: some critical issues. *Progress in physical geography*, 32(1), pp.31-49.
- Lozinski, W.V., 1909. Über die mechanische Verwitterung der Sandsteine im gemässigten Klima.
- Kieffer HH. 1979. Mars south polar spring and summer temperatures—A residual CO<sub>2</sub> frost. *J. Geophys. Res.* 84:8263–88
- Mackay, J.R., 1972. The world of underground ice. *Annals of the Association of American Geographers*, 62(1), pp.1-22.
- Malin MC, Edgett KS. 2001. Mars Global Surveyor Mars Orbiter Camera: Interplanetary cruise through primary mission. *J. Geophys. Res.* 106:23429–570
- Mangold, N., Maurice, S., Feldman, W.C., Costard, F. and Forget, F., 2004. Spatial relationships between patterned ground and ground ice detected by the Neutron Spectrometer on Mars. *Journal of Geophysical Research: Planets*, 109(E8).
- Matthews, J.A., Shakesby, R.A., Berrisford, M.S. and McEwen, L.J., 1998. Periglacial patterned ground on the Styggedalsbreen glacier foreland, Jotunheimen, southern Norway: micro-topographic, paraglacial and geocological controls. *Permafrost and Periglacial Processes*, 9(2), pp.147-166.
- Miall, A.D., 1985. Architectural-element analysis: a new method of facies analysis applied to fluvial deposits. *Earth-Science Reviews*, 22(4), pp.261-308.
- Munroe, J.S., Doolittle, J.A., Kanevskiy, M.Z., Hinkel, K.M., Nelson, F.E., Jones, B.M., Shur, Y. and Kimble, J.M., 2007. Application of ground-penetrating radar imagery for three-dimensional visualisation of near-surface structures in ice-rich permafrost, Barrow, Alaska. *Permafrost and Periglacial Processes*, 18(4), pp.309-321.
- Murton, J.B. and French, H.M., 1994. Cryostructures in permafrost, Tuktoyaktuk coastlands, western arctic Canada. *Canadian Journal of Earth Sciences*, 31(4), pp.737-747.
- Open.canada.ca. 1978. Permafrost - Open Government Portal. [online] Available at: <<https://open.canada.ca/data/en/dataset/ab0c22c6-bbc2-5838-9b6e-7d83c61ba91d>> [Accessed 2 June 2020].
- Murton J.B. 2013a. Ice wedges and ice-wedge

- casts. In: Elias S.A. & Mock C.J. (eds) Encyclopedia of Quaternary Science. 2nd edn. Elsevier, Amsterdam, 3, 436–451.
- Natural Resources Canada (NRCan). “Canada’s Changing Climate Report.” Natural Resources Canada, / Gouvernement Du Canada, 2019, [www.nrcan.gc.ca/maps-tools-publications/publications/climate-change-publications/canada-changing-climate-reports/canadas-changing-climate-report/21177](http://www.nrcan.gc.ca/maps-tools-publications/publications/climate-change-publications/canada-changing-climate-reports/canadas-changing-climate-report/21177)
- Osinski G. R. and Spray J. G. 2005. Tectonics of the Haughton impact event, Devon Island, Canadian High Arctic. *Meteoritics & Planetary Science* 40.
- Osinski, G.R., Lee, P., Spray, J.G., Parnell, J., Lim, D.S., Bunch, T.E., Cockell, C.S. and Glass, B., 2005. Geological overview and cratering model for the Haughton impact structure, Devon Island, Canadian High Arctic. *Meteoritics & Planetary Science*, 40(12), pp.1759-1776.
- Owens, E.H. and Harper, J.R., 1977. Frost-table and thaw depths in the littoral zone near Peard Bay, Alaska. *Arctic*, pp.155-168.
- Paquette, M., Fortier, D., Lafrenière, M. and Vincent, W.F., 2020. Periglacial slopewash dominated by solute transfers and subsurface erosion on a High Arctic slope. *Permafrost and Periglacial Processes*.
- Péwé, T.L. ed., 1969. *The Periglacial Environment: past and present*. McGill-Queen's Press-MQUP.
- Peterson, J.A., Scott, J.J. and Derbyshire, E., 1983. Sorted stripes of periglacial origin. *Australian Geographer*, 15(5), pp.325-328.
- Popov, A.I., 1974. Problems of Cryolithology. COLD REGIONS RESEARCH AND ENGINEERING LAB HANOVER NH.
- Porter, Claire; Morin, Paul; Howat, Ian; Noh, Myoung-Jon; Bates, Brian; Peterman, Kenneth; Keeseey, Scott; Schlenk, Matthew; Gardiner, Judith; Tomko, Karen; Willis, Michael; Kelleher, Cole; Cloutier, Michael; Husby, Eric; Foga, Steven; Nakamura, Hitomi; Platson, Melisa; Wethington, Michael, Jr.; Williamson, Cathleen; Bauer, Gregory; Enos, Jeremy; Arnold, Galen; Kramer, William; Becker, Peter; Doshi, Abhijit; D’Souza, Cristelle; Cummins, Pat; Laurier, Fabien; Bojesen, Mikkel, 2018, “ArcticDEM”, <https://doi.org/10.7910/DVN/OHHUKH>, Harvard Dataverse, V1, [21 October 2019].

- Price, L.W., 1972. The Periglacial Environment, Permafrost, and Man.
- Putzig, N.E., Morgan, G.A., Sizemore, H.G., Baker, D.M.H., Bramson, A.M., Petersen, E.I., Bain, Z.M., Hoover, R.H., Perry, M.R., Mastrogiuseppe, M. and Smith, I.B., 2019, July. Results of the Mars Subsurface Water Ice Mapping (SWIM) Project. In 9th Intl. Mars Conf., Pasadena, CA, July (pp. 22-25).
- Ramsdale, J.D., Balme, M.R., Gallagher, C., Conway, S.J., Smith, I.B., Hauber, E., Orgel, C., Séjourné, A., Costard, F., Eke, V.R. and van Gasselt, S.A., 2019. Grid Mapping the Northern Plains of Mars: Geomorphological, Radar, and Water-Equivalent Hydrogen Results From Arcadia Plantia. *Journal of Geophysical Research: Planets*, 124(2), pp.504-527.
- Ricketts, B., Osadetz, K.G. and Embry, A.F., 1985. Volcanic style in the Strand Fiord Formation (Upper Cretaceous), Axel Heiberg Island, Canadian Arctic Archipelago. *Polar Research*, 3(1), pp.107-122.
- Robertson P. B. and Mason G. D. 1975. Shatter cones from HaughtonDome, Devon Island, Canada. *Nature* 255:393–394
- Robertson P. B. and Sweeney J. F. 1983. Haughton impact structure:Structural and morphological aspects. *Canadian Journal ofEarth Sciences* 20:1134–1151
- Rodríguez-Ochoa, R., Olarieta, J.R., Santana, A., Castañeda, C., Calle, M., Rhodes, E., Bartolomé, M., Peña-Monné, J.L. and Sancho, C., 2019. Relict periglacial soils on Quaternary terraces in the Central Ebro Basin (NE Spain). *Permafrost and Periglacial Processes*, 30(4), pp.364-373.
- Rossbacher, L.A. and Judson, S., 1981. Ground ice on Mars: Inventory, distribution, and resulting landforms. *Icarus*, 45(1), pp.39-59.
- Rudberg, 1969, Distribution of small-scale periglacial and glacial geomorphological features on Axel Heiberg Island, Northwest Territories, Canada.
- Schennen, S., Tronicke, J., Wetterich, S., Allroggen, N., Schwamborn, G. and Schirmermeister, L., 2016. 3D ground-penetrating radar imaging of ice complex deposits in northern East Siberia. *Geophysics*, 81(1), pp.WA195-WA202.
- Schwerdtner, W.M. and Van Kranendonk, M., 1984. Structure of Stolz Diapir--A Well-Exposed Salt Dome on Axel Heiberg Island, Canadian Arctic Archipelago. *Bulletin of Canadian Petroleum Geology*, 32(2), pp.237-241.

- Seu, R., Phillips, R.J., Biccari, D., Orosei, R., Masdea, A., Picardi, G., Safaeinili, A., Campbell, B.A., Plaut, J.J., Marinangeli, L. and Smrekar, S.E., 2007. SHARAD sounding radar on the Mars Reconnaissance Orbiter. *Journal of Geophysical Research: Planets*, 112(E5).
- Sharp, R.P., 1974. Ice on Mars. *Journal of Glaciology*, 13(68), pp.173-185.
- Shur, Y.L. and Jorgenson, M.T., 1998, June. Cryostructure development on the floodplain of the Colville River Delta, northern Alaska. In *Proceedings of the Seventh International Conference on Permafrost (Vol. 57, pp. 993-1000)*. Centre d'études nordiques, Université Laval, Québec: Yellowknife, Canada.
- Slomka, J.M. and Eyles, C.H., 2015. Architectural–landsystem analysis of a modern glacial landscape, Sólheimajökull, southern Iceland. *Geomorphology*, 230, pp.75
- Smith, P.H., Tamppari, L.K., Arvidson, R.E., Bass, D., Blaney, D., Boynton, W.V., Carswell, A., Catling, D.C., Clark, B.C., Duck, T. and DeJong, E., 2009. H<sub>2</sub>O at the Phoenix landing site. *Science*, 325(5936), pp.58-61.
- Smyth, H.R., Morton, A., Scott, R.A., Omma, J.E., Kelly, S.R., Rippington, S., Braham, B., Gregory, U.J. and Jolley, D., Evolution of the Sverdrup Basin: new insights from field studies, integrated biostratigraphy & sediment provenance analyses.
- Squyres, S.W. and Carr, M.H., 1986. Geomorphic evidence for the distribution of ground ice on Mars. *Science*, 231(4735), pp.249-252.
- Stuurman, C.M., Osinski, G.R., Holt, J.W., Levy, J.S., Brothers, T.C., Kerrigan, M. and Campbell, B.A., 2016. SHARAD detection and characterization of subsurface water ice deposits in Utopia Planitia, Mars. *Geophysical Research Letters*, 43(18), pp.9484-9491.
- Snowdon, A., 2016. Upscaling of Coupled Models with Topography-Driven Surface-Water/Groundwater Interactions.
- Thomson, L.I., Osinski, G.R. and Pollard, W.H., 2012. The dielectric permittivity of terrestrial ground ice formations: Considerations for planetary exploration using ground-penetrating radar. *Journal of Geophysical Research: Planets*, 117(E9).
- Thorn, C.E., Dixon, J.C. and Abrahams, A.D., 1992. Periglacial geomorphology.
- Thorsteinsson R. and Tozer E. T. 1970. Geology of the Arctic Archipelago. In *Geology*

and economic minerals of Canada, Geological Survey of Canada Economic Geology Report 1, edited by Douglas R. J. W. Ottawa: Geological Survey of Canada. pp. 547–590

Ulrich, M., Grosse, G., Strauss, J. and Schirmer, L., 2014. Quantifying wedge-ice volumes in Yedoma and thermokarst basin deposits. *Permafrost and Periglacial Processes*, 25(3), pp.151-161.

Van Gasselt, S., Hauber, E. and Neukum, G., 2010. Lineated valley fill at the Martian dichotomy boundary: nature and history of degradation. *Journal of Geophysical Research: Planets*, 115(E8).

Washburn, A.L., 1980. *Geocryology: a survey of periglacial processes & environments*. Wiley.

## Chapter 2

# 2 A Periglacial Landsystem Analysis of Strand Fiord, Axel Heiberg Island, Nunavut: *A Polar Desert Case Study on Polygonal Terrain Evolution*

## 2.1 Introduction

The periglacial domain refers to a cold climate and the widespread gradation between environments that are specifically dominated by frost processes, which are characteristically subject to intense freeze-thaw cycles of superficial sediments (French, 1976). The Canadian High Arctic Archipelago houses one of the most abundant repositories of periglacial landforms on Earth giving rise to the expansion of periglacial geomorphology and geocryology studies in high latitude regions (Dutilleul et al. 2009; Haltigin et al. 2012; Bernard-Grand Maison and Pollard 2018). With a mean annual temperature of approximately  $-15^{\circ}\text{C}$  and an annual precipitation rate of less than 250 mm (water equivalent), certain periglacial regions in the Canadian High Arctic are classified as polar deserts (Heldmann et al., 2005; Paquette et al., 2020; Callaghan et al., 2005; Lee and Osinski, 2005). Polar deserts are characterized by their hyper-aridity, low humidity, low precipitation (rain or snow), and variable water supply, thus, moisture availability within the substrate is one of the most prevalent concerns. Based on elevation, insolation, and temperature, high Arctic environments in polar latitudes have little to no diurnal patterns, strong seasonal contrasts, and disproportional daily-annual temperature ranges compared to other climate zones (French, 2018). Characteristic periglacial climate, topography, ground substrate type, and other confounding factors contribute to the formation of periglacial landforms such as patterned ground under permafrost conditions. Perennially frozen ground or permafrost is highly constrained by temperature. It is defined by ground that remains at the freezing point, equal to or below  $0^{\circ}\text{C}$  for a minimum of two consecutive years (MacKay 1972; French 2007; Dobiński 2011). In terms of physical properties of permafrost, the main factors that play a significant role in shaping periglacial terrain are moisture content, density and porosity of sediments, and ground thermal properties (Washburn 1980; French, 2018; French and Shur 2010).

The periglacial environment is composed of many units or system tract components (i.e. polygonal patterned ground, freeze-thaw kettle lakes, gullies, aggradational permafrost landforms, and thermokarst features, etc.). This study emphasizes the importance of investigating spatial variability, landform interconnectivity, and substrate properties to validate the evolution particularly of polygonal patterned ground landforms. Ice-wedge polygon networks are formed via thermal contraction cracks typically in the colder, winter season and have a variety of phenotypes (Billings and Peterson, 1980; Mackay, 1990). As they are actively growing and replenished each season, the area in which most ice wedges remain active is along the permafrost zone as they experience prolonged cracking overtime. More specifically, there have been many studies regarding ice-wedge polygon formation and evolution (i.e., Fortier and Allard, 2004; Haltigin et al., 2012; McKay, 1972; Lachenbrauch, 1962), yet their spatial distribution, classification (i.e. secondary, tertiary, and n<sup>th</sup> order polygons), and subsurface characteristics have not been well-constrained on a large-scale in correlation with other associated periglacial features as a landsystem (French and Shur 2010; Matthews et al, 1998).

In High Arctic environments, polygons display a variety of phenotypes. Polygonal patterned ground in the Arctic is dominated by thermal contraction processes that form networks of contraction cracks extending through frozen ground. These primary cracks are initiated by stresses in permafrost from a rapid cooling (Lachenbruch 1962). Over time, these thermal contraction cracks may propagate forming (younger) secondary, tertiary, and n<sup>th</sup> order polygon troughs, which contribute to the preferential redirection of drainage within the permafrost basin and therefore, the entire periglacial landsystem. The formation of these multiplicative polygon troughs is not well constrained. From the initial subset of thermal contraction polygons, ice-wedge polygons can be further classified by the way the ice-wedge grows over time in three distinct categories: *epigenetic*, *syngenetic*, and *anti-syngenetic ice-wedge polygons*. *Epigenetic ice-wedge polygons* form in pre-existing permafrost, meaning they are much younger than the surrounding material, while *syngenetic ice-wedge polygons* form at the same time as the surrounding material – anti-syngenetic on the other hand, grew in conditions opposite to those of syngenetic ice wedges where there is a net loss of eroded materials rather than accumulation. The focus of this



study is on *high centre, syngenetic polygons*, which are defined by ice-wedge growth when the permafrost table rises due to sediment deposition or organic accumulation on the ground surface. This overall downward replenishment of the ice-wedge as the polygon begins to degrade (in an older and inactive state), leaves behind sunken troughs and polygon centres that consequently appear raised above the lee-slope positions of polygon edges – ice-wedges are largely eroded and truncated as this usually is not the primary state of polygons (Washburn 1980a; Mackay 2000, Mckay 1990).

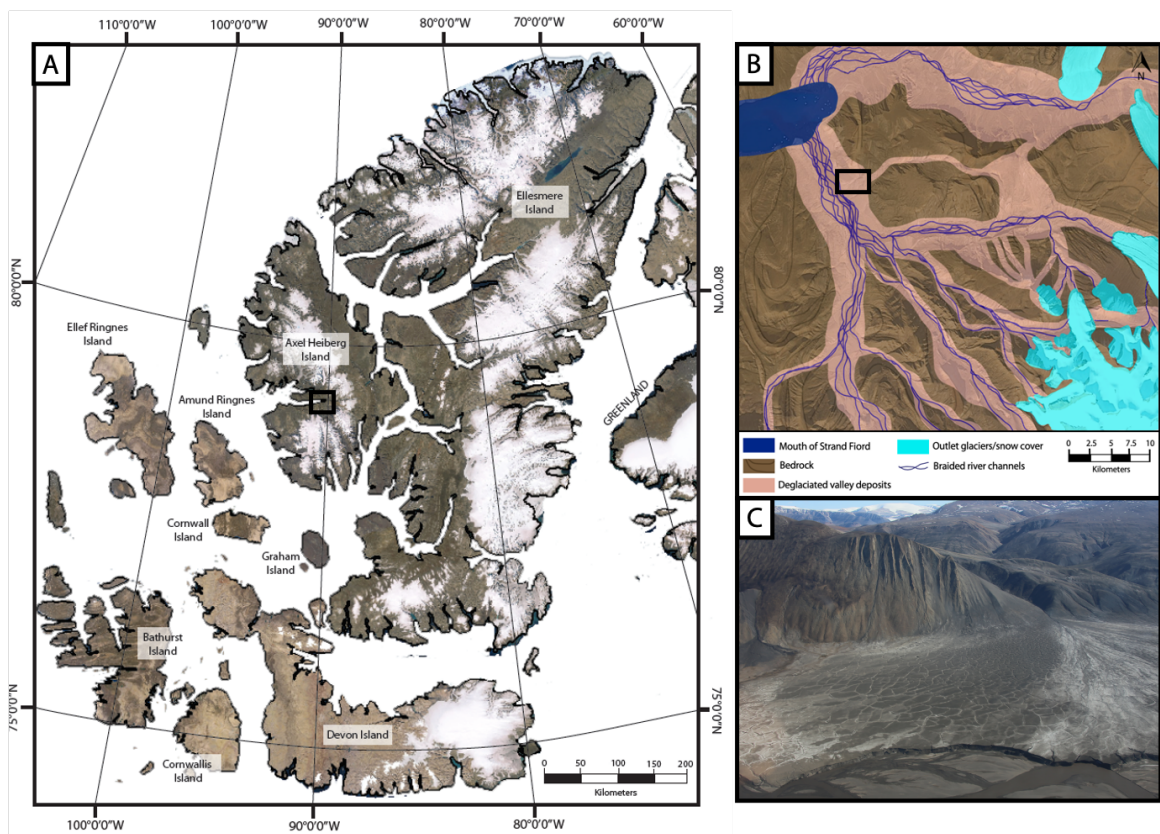
One of the major contributors for ice-wedge polygon morphology is the permafrost active layer thaw depth (Brown 1970), which thaws in the warmer months of the summer season and freezes again in the winter season. Additionally, cracking also occurs along polygon shoulders and troughs and contributes at larger depths well below the active layer and particularly during the winter season, when the entire profile is frozen (Lachenbruch, 1962). The active layer is a dynamic zone that will range in thickness year to year depending on local factors such as air temperature, snow cover, vegetation and ground material (French 2007). Amongst others, factors that affect ice-wedge polygon formation and n<sup>th</sup> order trough propagation include: (i) *dissolved salts*, (ii) *capillarity and/or sediment grain size*, (iii) *adsorption of sediments*, (iv) *latent heat*, (v) *thermal properties of soil*, (vi) *topography*, and (vii) *moisture input*.

In this study, the high Arctic periglacial environment was characterized using a landsystem analysis approach, which is a commonly applied methodology when investigating process-form relationships in depositional environments in order to determine the genetic origins of sediment and simplify complex terrain (Cooke and Doornkamp, 1990, Giles et al., 2017; Christian 1958). The overarching goal of this work is to understand the origin and evolution of ice-wedged polygonal patterned ground by characterizing their surficial expression/evolution, sedimentological architecture, potential ice content, and subsurface stratigraphies in which polygonal landforms are preserved. By investigating the behaviour of subsurface permafrost and sediment type, patterned ground morphology may be used to associate a depositional environment in correlation with temporal change as well as in-situ subsurface permafrost dynamics.



visible ice with an extrapolated permafrost thickness of 300-500 m (Natural Resources Canada, 2016).

The study site is located in Strand Fjord (79.16°, -90.23°), towards the western seaward portion of Axel Heiberg Island. It comprises an alluvial “fossil” fan deposit along a tributary valley draining into Strand Fjord. Due to the relative inactivity of this fan, it has been overprinted with polygonal patterned ground as well as dominated by periglacial processes (**Figure 2.1c**). On satellite and aerial imagery, different tonalities of the “fossil” fan are prominent features that represent hydrological signatures of the past seasonal flow of water in this region. Axel Heiberg houses the second highest concentration of salt diapirs globally, which may result to the prominent salt staining, as it appears as a white-ish colour on the fossil fan (**Figure 2.1c and 2.3**; Harrington et al., 2019). At the present day, landscape modification and evolution processes in Strand Fjord is dominantly driven by periglacial landscape processes.



**Figure 2.1.** (A) Map of a portion of the Canadian High Arctic Archipelago highlighting Axel Heiberg Island and the study site located in Strand Fiord (*Sources: Esri, DigitalGlobe, GeoEye, i-cubed, USDA FSA, USGS, AEX, Getmapping, Aerogrid, IGN, IGP, swisstopo, and the GIS User Community*) (B) A subset map of the study site (outlined in the black box) and valley networks to provide contextual setting of the fiord system. *Source is same as (A).* (C) An oblique aerial photograph of the study site of the polygonized “fossil” fan on Strand Fjord, Axel Heiberg Island. The high albedo or light colour-toned features on the fan are water-marker indicators of mineral deposits (i.e. gypsum). There is a smaller, more recently active fan to the left-most of the image. *Image by: 2017 field team*

## 2.3 Methods

In order to characterize the widespread subsurface dynamics of polygonal terrain in general, a two-day helicopter-enabled field campaign was executed at the study site in early July 2019 as part of a longer campaign on Axel Heiberg Island. In tandem with taking field notes and field measurements, aerial images were also collected at different airborne vantage points of the study sites along with drone data/images to support 3D terrestrial photogrammetry models. Prior to fieldwork, remote sensing datasets from ArcticDEM, Worldview, and Landsat 8 were also used as reconnaissance tools for the area. It should also be noted that a previous fieldwork campaign with both field and helicopter observations was conducted in 2017. In general, sedimentological, geophysical, and remote sensing field methods were used to collect robust information and data for understanding the periglacial landsystem of Strand Fiord.

### 2.3.1 Sedimentological Logging and Description

Sediment grain size and characteristics were determined by manual hand-logging and using a grain size card measurement to approximately quantify the grain size. Facies types were described using a standard facies coding scheme (Miall 1983, Eyles et al., 2010). In this study, 8 facies types, across 7 sediment pits were identified. Pits were excavated each at a polygon trough (*PT*) and at a polygon centre (*PC*) taken from each of the proximal (*PTP*, *PCP*; 15N 556512 m E, 8792487 m N), medial (*PTM*, *PCM*; 15N 555050 m E, 8792487

m N), distal (*PTD, PCD*; 15N 554893 m E, 8793573 m N; **Figure 2.4**), and *fan edge* areas of the study area. While the excavation of the pits was limited to the depth of the frozen active layer of permafrost, fieldwork also involved the documentation of sediment characteristics, sediment facies structure, and landform characteristics to enable reconstruction of the depositional history of this portion of Strand Fiord. These facies logs were all digitized to showcase the variability in each zone in the alluvial fan with respect to depth to the active layer, grain size, and polygon size using sediment facies logs.

### 2.3.2 LiDAR

The AkhkaR4DW Light Detection and Ranging (LiDAR) system was also used in the field to create an unprecedented centimeter scale resolution digital elevation model (DEM) of the study area. This instrument is a backpack mobile (LiDAR) scanning system, built by the Finnish Geospatial Research Institute, that can collect high precision 3D topographic data kinematically (Kukko et al., 2020). Mapping is carried out in walking speeds, typically 3-5- km/h depending on the terrain. Raw LiDAR point cloud data were then batch processed using a combination of CloudCompare Raster tools (2.12.alpha) and ESRI's ArcGIS 10.7.1 Spatial Analyst Toolbox and LAS Dataset toolset. While collected at the same time, the LiDAR scan was collected independent of the GPR and sediment pit excavation sites due to the time-constraint and mobility in data collection as well as geographic calibration errors taken into account pre-/post-processing.

### 2.3.3 Geophysical Survey: Ground Penetrating Radar (GPR)

A 25m x 25m ground penetrating radar (GPR) grid survey was carried out with a total of 52 transects and ~180 depth slices while following the common offset gather method in addition to the “zamboni” setup/method making a zigzag pattern with a step-size of 1 m intervals. This coverage encompasses two secondary polygons split by a secondary trough with a primary trough bordering the outer edges. This grid is named GPR\_G1; 25 lines were oriented north-south and 25 lines were oriented in the west-east direction in the Mid-fan/Transition Zone in order to encompass and characterize ice-wedge variability after initial reconnaissance of the subsurface (**Figure 2.4**). Three GPR lines named GPR\_L1, GPR\_L2, and GPR\_L3 were also collected at the Apex, Mid-fan, and Distal zones

respectively. A frequency of 250 MHz was used to obtain near-surface, high resolution radar data (Noggin 250 MHz, Sensors and Software™). Using the Ekko\_Project software, a mean velocity propagation was calibrated to be 0.064 m/ns through the Hyperbola Velocity Calibration (hyperbola-fitting) tool in LineView, which indicates a wet clay/sand subsurface assuming the presence of a point scatterer in the subsurface. Additionally, where velocity varies horizontally and vertically (as it frequently does), numerous (and clearly defined) scatterers may be required for an accurate estimate. This is used to convert two-way travel time to depth. In more detail, the travel time is converted to *position* versus *apparent depth* ( $d_a$ ) via the equation:

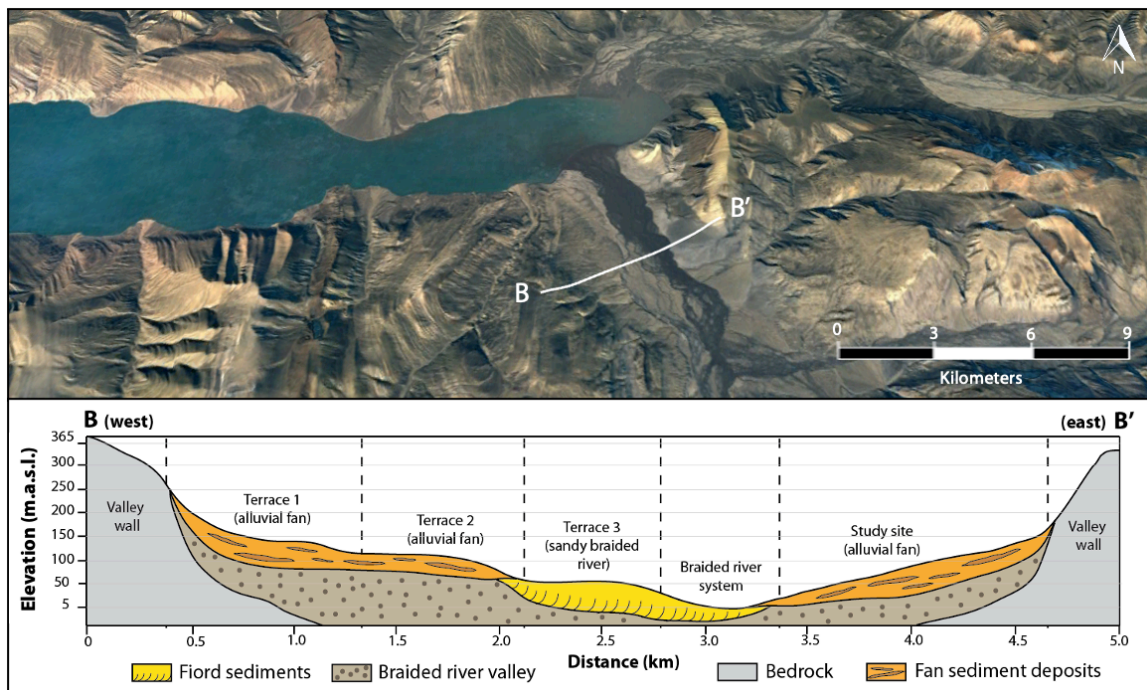
$$d_a = \frac{vt}{2} \quad (1)$$

where  $d_a$  is the apparent depth,  $v$  is the propagation velocity (sometimes left as the speed of light ( $c = 3.00 \times 10^8$  m/s), only true in a vacuum) and  $t$  is the two-way travel time. It is important to note that this is an automated calculation done by the Ekko\_Project software.

Reflectors on the profile are identifiable up to an approximate depth of 0.9 m, thereby providing general stratigraphic and structural context. Due to stratigraphic heterogeneity, the top section of the depth profile is susceptible to signal attenuation due to the presence of the permafrost active layer. In order to filter the noise from the dataset and further extrapolate, respective processing elements were used such as the dewow filter, background subtraction (total background), gain (with a signal attenuation of 16db/m), envelope filter, and migration filter (frequency-wave number). Post-processed data were then compiled into Voxler 4 to render an isosurface thus, a 3D model of subsurface ice-wedges that can be used not only as a morphologic visualization tool but also as a calculator for subsurface ice volume. Volume calculations are generated from voxels (3D pixels) that are either partially or fully included in the isosurface. The goal of the GPR reflection survey is to determine valuable amplitude traces that can potentially be mapped to locate the position/saturation of ice-wedges in the subsurface and to distinguish probable stratigraphic boundaries in frozen ground.

## 2.4 Results

From the surface morphology of this polygonal and periglacially dominated terrain, to its subsurface components (i.e. GPR, sedimentology), results were analyzed in the form of (1) digitized periglacial sediment logs for correlation, facies association, and depositional environment interpretation, (2) GPR radargram facies with a description of radar signatures, and (3) 3D-GPR models of subsurface ice in order to estimate ice volume.

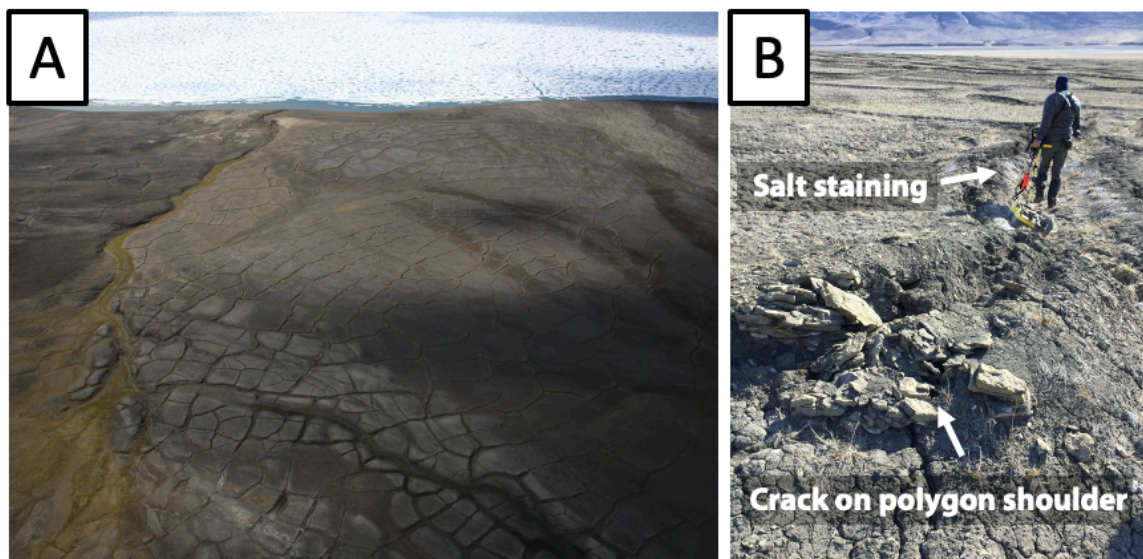


**Figure 2.2.** Sediment overlaying bedrock cross-section of deglaciated trunk river valley encompassing the study site. The top is an Operational Land Imager (OLI) Landsat 8 satellite image showing a 5-km profile of the cross section from point B to B' with elevation values extracted from Google Earth i.e. combination of a range of topographic datasets from OpenTopography, USGS National Elevation Dataset (NED), and/or Shuttle Radar Topography Mission (SRTM) (meters above sea level or m.a.s.l.). The bottom is a schematic and interpreted landsystem diagram highlighting various physiographic features of the valley estimated through bedrock depth (exposed through the valley walls) and the depth of overlying sediment and active layer.



### 2.4.1 Field Observations

The alluvial fossil fan is dominated by polygonal terrain. Bordering the edges of the valley are bedrock valley walls overlain by sediments from both west and east directions (**Figure 2.2**). The valley wall to the west is located at 365 m.a.s.l and the valley wall to the east is located at 325 m.a.s.l. To the west of the river valley, there are three river terrace levels with a stepped terrace topography (Terrace 1, 2, and 3) from an alluvial fan transitioning into the sandy braided river system at the base of the deglaciated valley (**Figure 2.2**). Eastward, the valley has been widely dominated by an alluvial fan from a sub-valley incision to the east of the fiord with a smooth, continuous elevation change and a slope of  $\sim 15^\circ$ .



**Figure 2.3.** (A) Aerial (taken in summer 2017 via helicopter) and (B) ground images of polygons at the Strand Fiord alluvial fan looking towards the west.

The alluvial fossil fan was roughly classified into three zones based on polygon size and morphology (i.e. whether there was a presence of either primary or secondary polygons). Along the cross-section from the *Apex/Proximal Zone* (Zone 1), then *Medial Zone* (Zone 2), to the *Distal Zone* (Zone 3) of the fan, there is an obvious increase in polygon size (**Table 1.1**; **Figure 2.3**, **Figure 2.4**), which was the basis of the zonal subdivision. Specifically, Zone 2 had an abundance of secondary polygons, while Zones 1 and 3 are



characterized by primary polygons. It is important to note that although there are three classified zones, boundaries between each zone are estimated boundaries, which are not clearly defined because there seems to be some intermixing of morphology in some areas of cross-over. These high centre polygon morphologies have varying trough depths in different zones of the fan. Although they lack raised shoulders, cracks are present at the polygon shoulders indicating an active state as well as salt staining along the edges of the troughs (**Figure 2.3**). Thaw depths were measured on July 6<sup>th</sup> 2019. At Zone 1 or the *Apex/Proximal Zone*, the thaw depth of the permafrost active layer is at 0.30 m at the proximal polygon centre (PPC) and situated at 0.35 m at the proximal polygon trough (PPT) following a gradual topographic dip of the alluvial fan down slope. At Zone 2 or the *Transition/Medial Zone*, the thaw depth of the permafrost is at 0.40 m at the medial polygon centre (MPC) and situated at 0.32 m at the medial polygon trough (MPT). The thaw depth is relatively shallower at medial polygon trough, which could be due to subsurface upwelling. Finally, at Zone 3 or the *Distal Zone*, the thaw depth at distal polygon centre (DPC) is at 0.45m and distal polygon trough (DPT) at 0.5 m following the down-dip of the fan.

There are also very unique polygon features in Zone 2 as shown in **Figure 2.5**, whereby using high resolution LiDAR, we are able to see delineate a possible downstream flow feature downslope towards possible ice-wedge replenishment (**Figure 2.5**). The mean area of polygons in the *Apex Zone* is 3,525 m<sup>2</sup> (n=351) with trough depths averaging 0.60 m (n=18). This zone has the deepest trough depths ranging from up to 0.85 m. The mean area of polygons in the *Transitional/Medial Zone* is 3,241.96 m<sup>2</sup> (n=690), inclusive of the secondary and tertiary polygons. This zone has the lowest trough depths with a mean depth or 0.27 m, and depth ranging from 0.15 to 0.40 m (n=13). The mean area of polygons in the *Distal Zone* is 28,721.69 m<sup>2</sup> (n=326). This zone has trough depths of 0.42 m on average, ranging from 0.25 to 0.60 m (n=12).

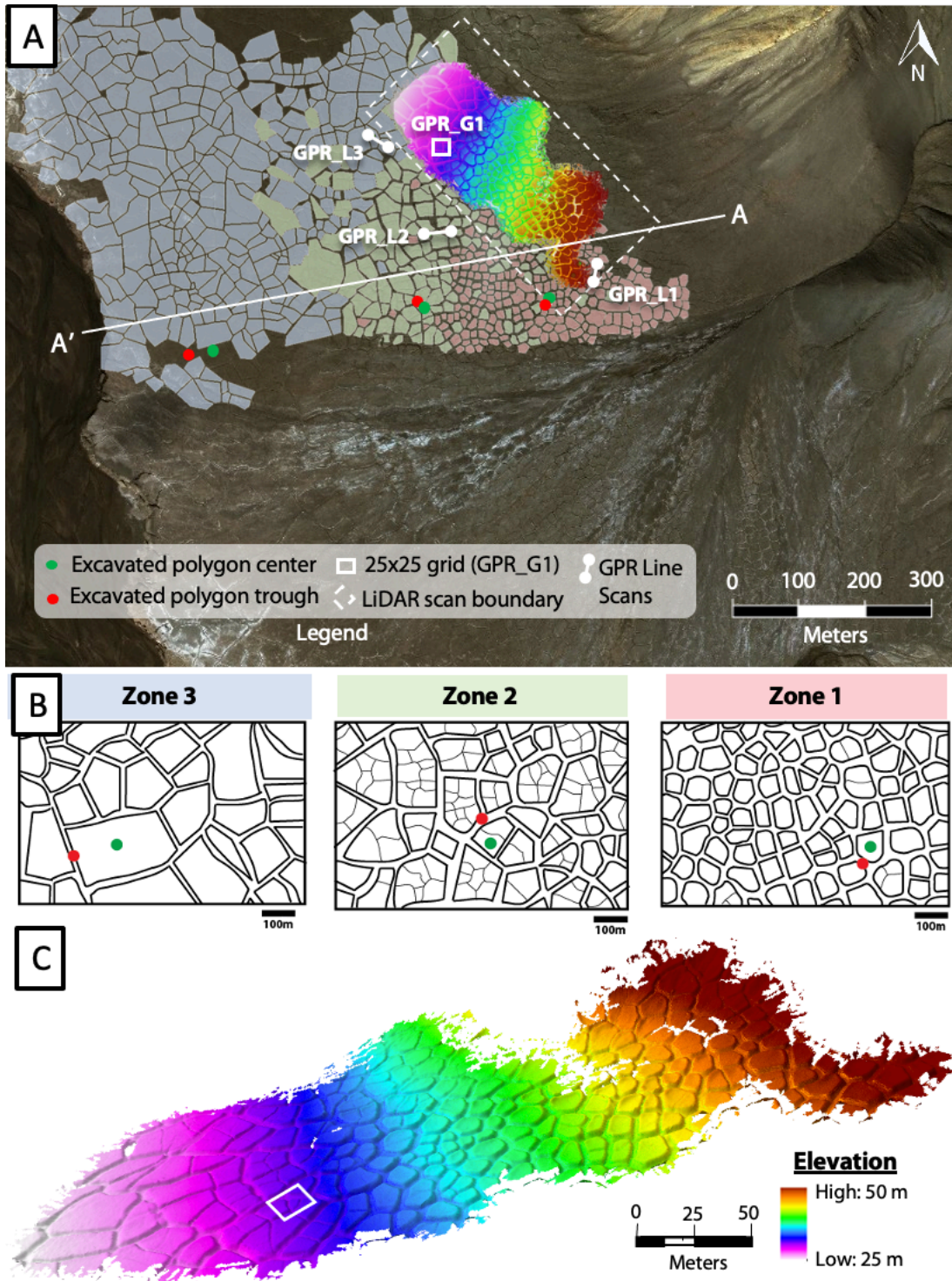
**Table 2.1.** Statistics for length, width, area, and diameter of polygons in all zones measured in meters from satellite imagery (i.e Worldview) observations. Vector shapes

were digitized for each polygon and statistics were extracted using the *Calculate Statistics* tool in ArcGIS 10.8.

<b>LENGTH (m)</b>	<b>Min</b>	<b>Max</b>	<b>Sum</b>	<b>Mean</b>	<b>Std. Dev</b> <i>1-sigma</i>
Apex/Proximal Zone (n=351)	30.37	139.12	26,720.86	76.13	20.39
Transitional/Medial Zone (n=690)	27.58	259.62	53,335.99	77.30	30.21
Distal Zone (n=326)	62.71	669.53	75,349.47	231.13	94.15
<b>WIDTH (m)</b>	<b>Min</b>	<b>Max</b>	<b>Sum</b>	<b>Mean</b>	<b>Std. Dev</b>
Apex/Proximal Zone (n=351)	22.69	132.05	19,991.17	56.95	16.49
Transitional/Medial Zone (n=690)	17.55	146.73	36,048.26	52.25	20.66
Distal Zone (n=326)	32.08	370.65	50,781.31	155.77	61.72
<b>AREA (m<sup>2</sup>)</b>	<b>Min</b>	<b>Max</b>	<b>Sum</b>	<b>Mean</b>	<b>Std. Dev</b>
Apex/Proximal Zone (n=351)	581.04	13,261.11	1,237,393.48	3,525.34	1,868.01
Transitional/Medial Zone (n=690)	322.02	30,042.47	2,236,949.91	3,241.96	2,783.26
Distal Zone (n=326)	2,044.89	119,271.91	9,363,273.68	28,721.69	20,933.27
<b>DIAMETER (m)</b>	<b>Min</b>	<b>Max</b>	<b>Sum</b>	<b>Mean</b>	<b>Std. Dev</b>
Apex/Proximal Zone (n=351)	24.10	115.16	1,112.38	59.37	43.22
Transitional/Medial Zone (n=690)	17.94	173.33	1,495.64	56.94	52.76
Distal Zone (n=326)	45.22	345.36	3,059.95	169.47	144.68
<b>TROUGH DEPTH (m)</b>	<b>Min</b>	<b>Max</b>	<b>Sum</b>	<b>Mean</b>	<b>Std. Dev</b>
Apex/Proximal Zone (n=18)	0.40	0.85	10.85	0.60	0.12
Transitional/Medial Zone (n=13)	0.15	0.40	3.45	0.27	0.10
Distal Zone (n=12)	0.25	0.60	5.0	0.42	0.12

The source of the sediments in the study area is a combination of fluvial and/or fiord type deposits. A topographic cross-section (B-B') of the deglaciated trunk river valley was characterized into various facies zones in order to better understand the origin of these fiord sediments with respect to the study site (**Figure 2.2**). Overall, these sediments infilling this

deglaciated valley were generally released by glaciofluvial action from tributary glacial valleys and the study site is mainly composed of outwash sands and fine-grained fluvial sediments from the drainage of the fiord upstream resulting to fine clays/muds suspended and propped up in the middle of the braided river system.



**Figure 2.4.** Context image of the study area. (A) Aerial photograph of study area showing sedimentological excavation, GPR and LiDAR sites. (B) Strand Fiord alluvial fossil fan classification zones projected onto (A) at identical zoom scales to show

consistency. Green dots show sites of polygon centre excavation and red dots show sites of polygon trough excavation. (C) Partial LiDAR coverage map of the alluvial fan (covering 350m horizontal scale). Partial LiDAR coverage of the study area is also shown in Figure 3 with a 25m x 25m white box within the LiDAR image that represents the GPR grid. Additionally, six pits were excavated throughout the alluvial fossil fan composed of two sediment pits per zone located on the polygon troughs and centres shown by the red and green dots respectively. A profile cross-section of the fan was acquired using A-A' coordinates shown in Figure 2.6. With relevance to the thaw depth of the active layer, it should be mentioned that these excavated pits were dug on July 4<sup>th</sup> and 6<sup>th</sup> 2019.

## 2.4.2 Sedimentology

The Strand Fiord alluvial fossil fan sediments are dominated by fine- to medium- grained sands and silty clays and consists of a series of coarsening-upward successions with intervening units of deformed, fine-grained sediment. Facies descriptions and active layer depths are summarized in **Table 2.2** and **Figure 2.6**. These facies types were classified following the previously defined four distinct stratigraphic zones (*Apex/Proximal Zone*, *Transition/Medial Zone*, *Distal Zone*, and *Fan Edge Zone*) that may be used to reconstruct temporal changes in depositional and paleoenvironmental conditions.

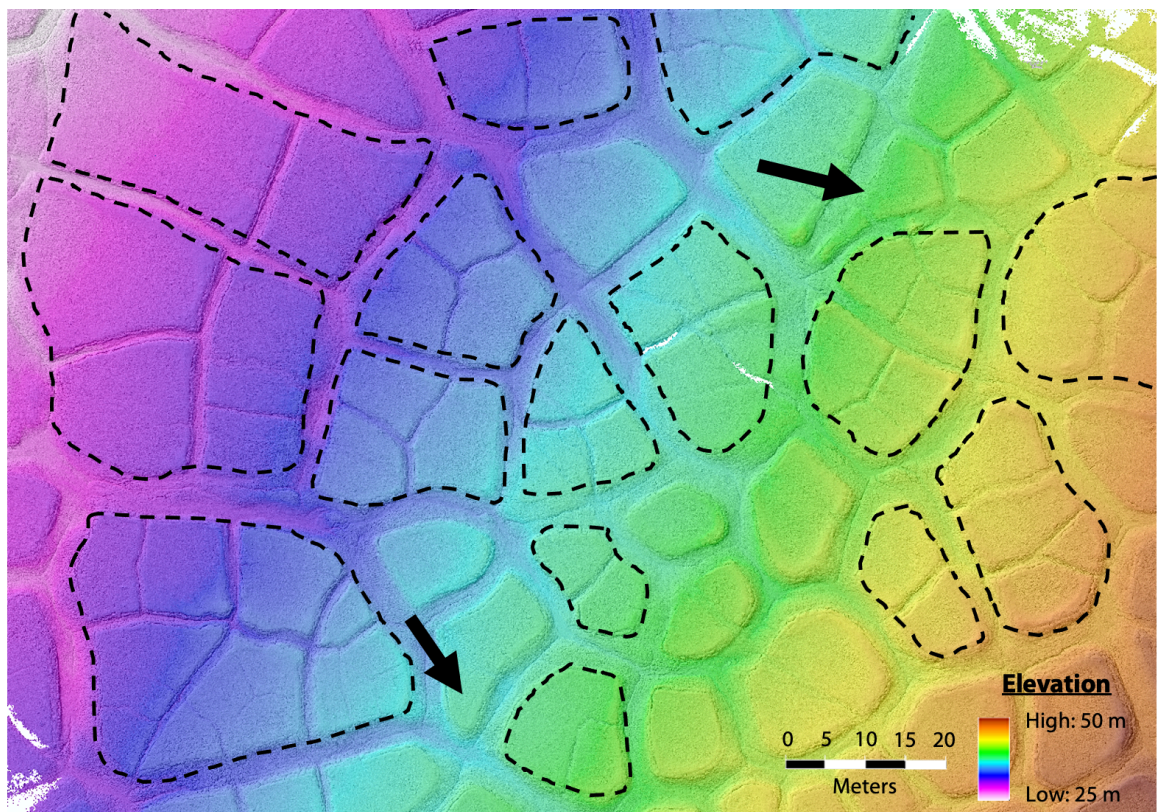
### *Zone 1 – Apex/Proximal Zone*

The proximal-polygon centre (PPC) and proximal polygon trough (PPT) are the uppermost sedimentary section in the alluvial fan and shows a coarsening upward sequence of horizontally laminated and massively deformed sands with scattered clasts, common organic matter, sand lenses (~2.5mm) and inter-laminated silts (Sm, Sd, Sh; **Table 2.2**, **Figure 2.4**, **Figure 2.6**). This sediment package shows a low degree of textural heterogeneity and PPC is the shallowest sediment unit recorded in the alluvial fan. Ice within sediment grains is present in these two units however, they are more prominent at the base of the PPT and melt abruptly upon exposure to air. There are no ice wedges present in these two units. The average slope of this zone is ~10.5 degrees.



## *Zone 2 – Transition/Medial Zone*

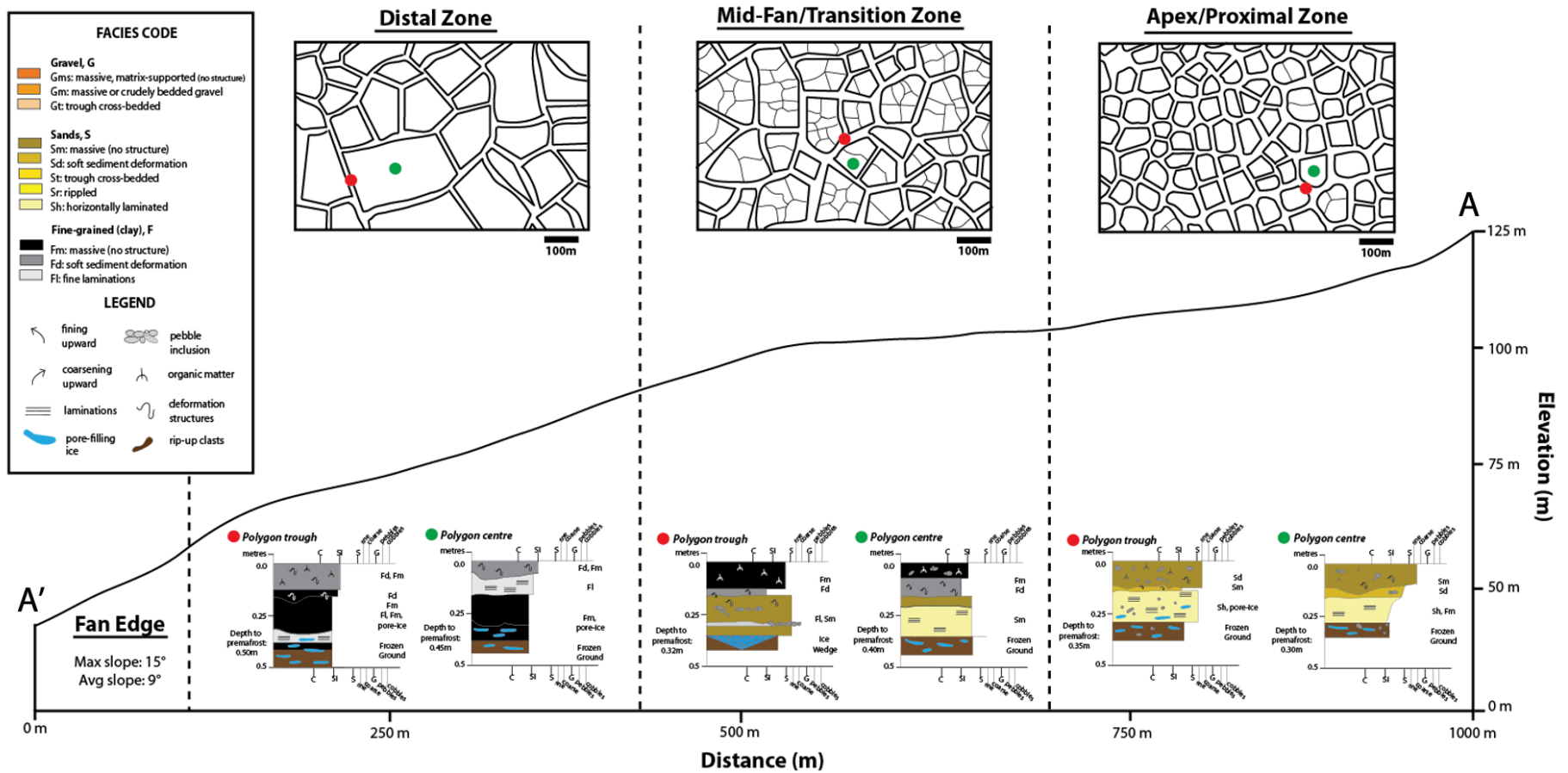
The medial-polygon centre (MPC) and medial-polygon trough (MPT) are two highly variable units that are composed of massive and deformed fine silts that coarsen downwards towards the base of deformed fine-medium grained sands with thin silty-clay laminated inclusions (Fm, Fd, Fl, Sm; **Table 2.2, Figure 2.4, Figure 2.6**). This zone is the most heterogeneous out of all three zones. MPT consists of a very distinctive active layer horizon as there is an ice wedge present at the base of this unit as well as a saturation zone at ~0.30m. The average slope of this zone is ~8.5 degrees.



**Figure 2.5.** 3cm LiDAR DEM showing clustering of secondary polygons (i.e. polygons that have undergone more cracking). There is also a distinct polygon ridge that may indicate the outward movement of sediment from polygons towards the ice wedges (troughs) shown by the black arrows, which could be possible downstream flow features downslope towards possible ice-wedge replenishment.

### *Zone 3 – Distal Zone*







The distal-polygon centre (DPC) and distal-polygon trough (DPT) consists predominantly of fine to very fine silty clays. Included in this unit are thin units of fine laminated silts with common organic matter and small pebble inclusions 5-8 mm in diameter. This unit also illustrates soft-sediment deformation in horizons where silts and clays immediately cap coarser silt boundaries (Fd, Fm, Fl; **Table 2.2, Figure 2.4, Figure 2.6**). DPC and DPT both show an abundant evidence for pore-ice at the base of each unit. Areas of DPC and DPT are often dominated by accumulated water in troughs due to the fan topography. Small thaw lakes are also present in areas of ponding. The average slope of this zone is ~10.0 degrees.



**Figure 2.6.** Sedimentological log of the six sediment pits/excavations throughout Strand Fiord alluvial fossil fan sediments. Sedimentary facies types are grouped into units (PPC/PPT, MPC/MPT, DMC/DMT) depending on their location on the fan. Profile A-A' follows the exact topography of the fan illustrating the transition of the fan sediments from fine-medium sands (Apex/Proximal Zone) to fine silty clays (Distal Zone). The facies codes and symbols are shown in the legend. No data are available regarding the nature of sediments beneath these sediment pits due to the frozen nature of the ground.



**Table 2.2.** Stratigraphic units and facies types identified in the Apex/Proximal, Transition/Medial, and Distal Zones of the Strand Fiord alluvial fossil fan (see Figure 6 for facies codes).

Region	Name	Depth to permafrost (m)	Facies codes	Facies Descriptions	Facies
Apex/ Proximal	polygon-centre (PPC)	0.30	Sm, Sd, Sh, Fm	Coarsening upward succession of massive, deformed sand with fine, horizontal sand lenses (~2.5mm) and inter-laminated silts.	
	polygon-trough (PPT)	0.35	Sd, Sm, Sh	Massive and deformed fine-medium sands with horizontal laminations (~3-5mm).	
Transition/ Medial	polygon-centre (MPC)	0.40	Fm, Fd, Sm	Massive and deformed medium silts and sands.	
	polygon-trough (MPT)	0.32	Fm, Fd, Fl, Sm, Ice-wedge	Massive, deformed and laminated fine-grained silty clays and sands. A saturation boundary at 0.12m is observed along with an ice-wedge lens (clear ice).	
Distal	polygon-centre (DPC)	0.46	Fd, Fm, Fl	Massive fine silty clays with deformed laminations. Pore-ice is observed at 0.30m through to the active layer.	
	polygon-trough (DPT)	0.50	Fd, Fm, Fl	Massive fine silty clays with deformed laminations. A saturation boundary at 0.41m is observed along with pore ice inclusions through to the active layer.	

## *Fan Edge Zone*

The 12.5m outcrop at the edge of the fan is composed of subdivided units that gradually change to a higher proportion of sand and gravelly detritus farther down the succession (**Figure 2.7; Table 2.3**). These facies types were grouped into eight distinct stratigraphic units (*Unit A – H*) that may be used to reconstruct temporal changes in depositional and paleoenvironmental conditions specifically looking at the stages of polygon development.

Starting at the base of the section, *Unit H* is the thickest stratigraphic unit composed entirely of massive and crudely bedded medium-grained sands. Due to its close proximity to the edge of the braided river system, there are erosional surfaces and features along this part of the outcrop as well as frequent slump falls from the sloped sediment lying atop of *Unit H* such as, *Unit G, F, and E*. This unit is highly influenced by the braided river as well as abrupt sediment deposition events as these fluvial fiord deposits are found uniformly within this unit with no particular structure.

*Unit G* and *F* form a coarsening upwards succession comprising fine to medium grained massive and deformed sands and sub-rounded gravels containing clay rip-up clasts (Sm, Sd, Gms; **Table 2.3, Figure 2.7**). The gravel horizon capping these units indicates a high velocity deposition event that may have been contributed by either a high velocity trunk braided river event or cyclic over wash deposition from the surficial fan feeder streams or straight channels. The presence of rip-up clasts indicates that these sediments were deposited by relatively high velocity and erosive flows (Benito, Sánchez-Moya and Sopeña, 2003).

*Unit E* consists of slumped, discontinuous ice tilted at a slope of approximately 20° along with massive and structureless fine sands that appear to be frozen surrounding this ice block/lens inclusion. This block of ice is situated in the middle of this stratigraphic zone and thereby, disrupts the continuous massive sand matrix.

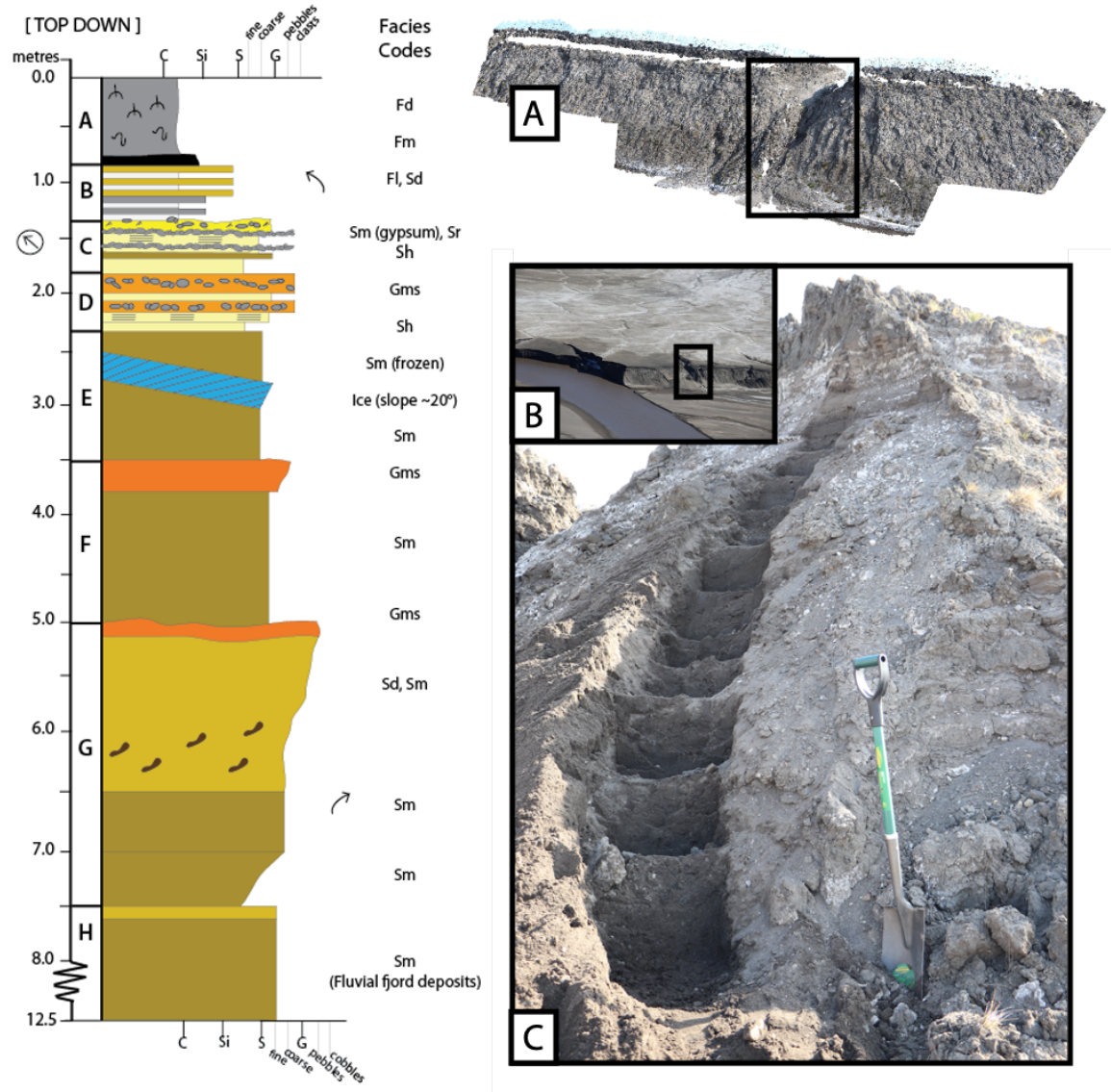
The most texturally heterogenous stratigraphic is *Unit D*. In this zone, horizontally laminated fine to medium grained sands comprise the base while transitioning to crudely

bedded, massive gravel layers (Sh, Gms; **Table 2.3; Figure 2.7**). Included in this up-sectional unit are several clasts indicative of high energy depositional conditions. Clast sizes are highly variable (20mm-14.5 cm) and the unit contains some larger boulders (up to 15 cm in diameter). This zone contains the coarsest material recorded in the outcrop.

*Unit C* is a highly variable unit that consists of horizontally bedded sands at the base, through rippled sands with thin silty clay beds, into coarse-grained, massive at the top (Sh, Sr, Sm; **Table 2.3, Figure 2.7**). The presence of fine-grained laminated deposits at the base of this zone indicates deposition in low energy (low sediment influx) conditions, which transition into higher energy fluvial conditions up-section. The massively bedded sands also show evidence of salt precipitate, in particular gypsum, which can be used as a signature of water transport and permafrost seepage. This change in depositional energy may relate to changes in the active layer depth/activity within the Strand Fiord fossil alluvial fan (i.e. seasonal), or to variable amounts of sediment input (low to high). This sediment package shows a high degree of textural heterogeneity and is the thinnest single unit recorded in the outcrop (0.30 m, **Figure 2.7**).

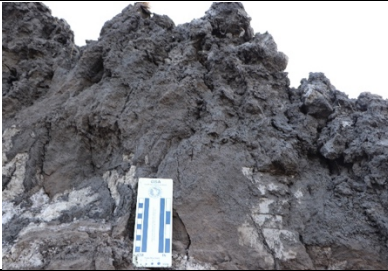




*Unit B* forms a fining upwards succession made of laminated fine-grained silts and clays to fine-medium sands. This zone also shows evidence of soft-sediment deformation (interpreted as water escape structures) in horizons where silts and clays immediately cap coarser sands. This deformation within this interlayering sequence is probably caused by dewatering due to the rapid deposition of fine- over coarse-grained sediment (Cheel and Rust, 1986).

*Unit A* is the uppermost sedimentary unit exposed in the outcrop and shows a fining upward sequence of massive and crudely bedded fine grained sediments with no structure (Fm, Fd; **Table 2.3, Figure 2.7**). The topmost surface is dominated by common organic matter.






**Figure 2.7.** (A) Sedimentological log of the 12.5-meter-high exposure through the Strand Fiord alluvial fossil fan sediments. Sedimentary facies types are grouped into units (A-H). The facies codes and symbols are shown in the legend. No data are available regarding the nature of sediments beneath those exposed in outcrop. (A) An 3D image rendering of the Fan Edge Zone showing an incision from a fan feeder stream along a polygon trough where (B) is located. This model was made using terrestrial photogrammetric techniques. (C) 12.5-meter-high outcrop of Strand Fiord alluvial fossil fan sediments in the Fan Edge Zone.

**Table 2.3.** Stratigraphic units and facies types identified in the Fan Edge Zone outcrop (see Figure 2.7 for facies codes)

Units	Unit thickness (m)	Facies codes	Facies Descriptions	Facies
A	0.80	Fd, Fm	Deformed, massive sands with convolute release cracking features and white coloured mineral (i.e. salt/gypsum) signature.	
B	0.60	Fl, Sd	Fining upward succession of fine silts with convolute lamination and deformed sands with dewatering structures. This zone is consistent with the active layer horizon (no ice) with gypsum-rich signatures (due to permafrost seepage).	
C	0.35	Sm, Sr, Sh	Massive, ripple-laminated, fine-grained sands with sub-rounded to rounded clast inclusions/horizons, ~10mm-10cm diameter.	
D	0.55	Gms, Sh	Massive to crudely bedded gravel interbedded with a horizontally laminated coarse sand matrix with clast inclusions, ~20mm-15cm diameter.	
E	1.20	Sm, Ice	Massive, fine-medium sands and rip-up clasts with massive ice block inclusion at a slope angle of ~20°.	



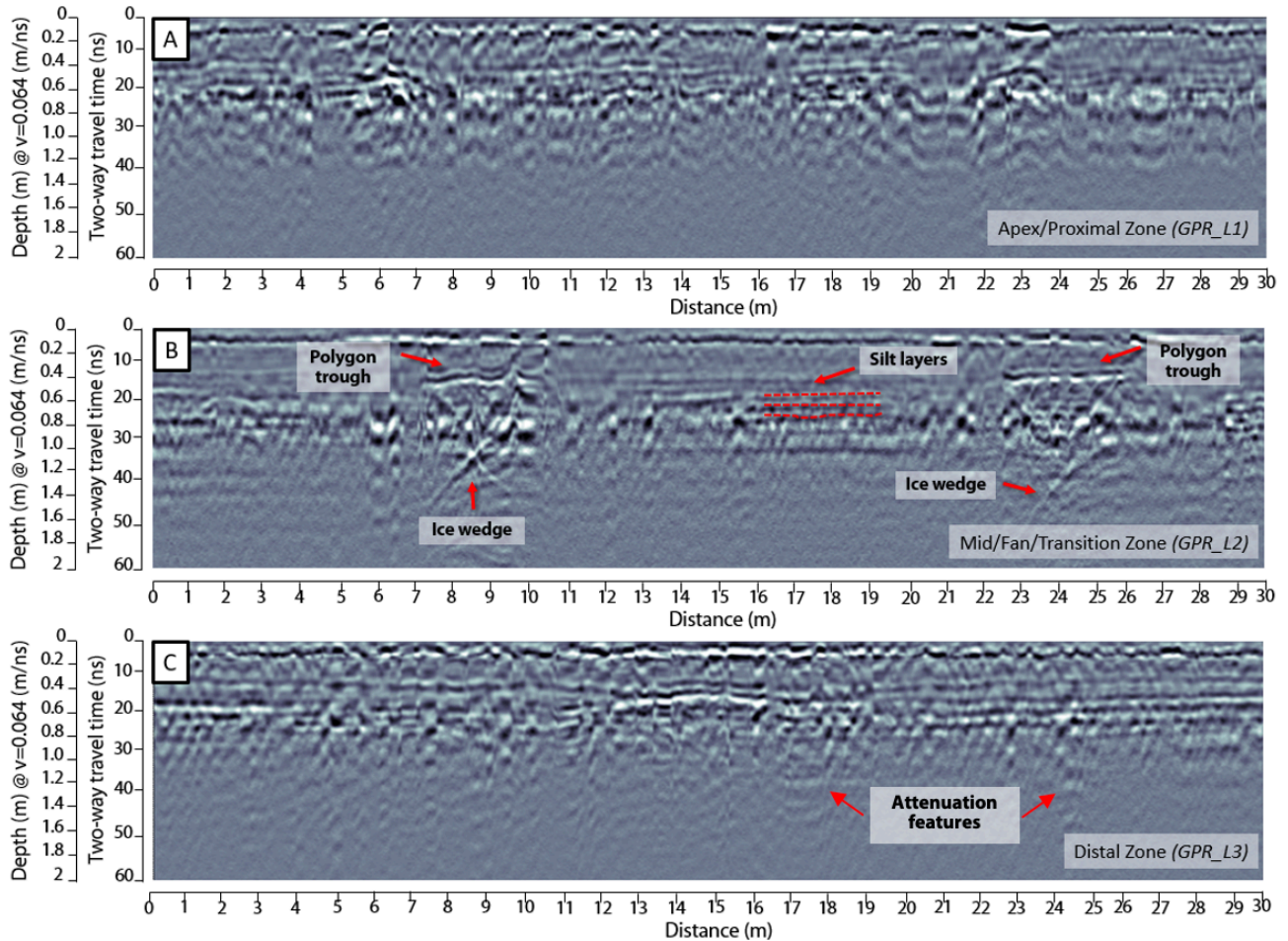
F	1.50	Gms, Sm	Massive to crudely bedded gravel with massive, fine-medium sands. Gravel horizon with sub-rounded rip-up clasts and pebble inclusions ~1-5cm in diameter.	
G	2.50	Gms, Sd, Sm	Coarsening upward succession of coarse gravelly massive sand with pervasive soft sediment deformation structures with pebble inclusions ~1.5-7cm diameter.	
H	5.0	Sm	Massive, slumped fine-medium sands at the base of fluvial terrace.	

### 2.4.3 Radargram Facies & 3D-GPR Modelling of Subsurface Ice

To investigate various subsurface properties for a larger reference area, we used non-invasive GPR techniques to image the subsurface in various survey set-ups. After the synthesis of field observations and data processing of GPR data, GPR\_G1, taken at the *Transition Zone/Medial*, served as a basis of analysis in order to corroborate the sediment stratigraphy (**Figure 2.9**, **Figure 2.6**). Three radargram lines, GPR\_L1, GPR\_L2, and GPR\_L3 (**Figure 2.3**) were also taken respectively from the *Apex*, *Transition*, and *Distal Zones* of the Strand Fiord polygon network (**Figure 2.8**).

Radargram line scans show the stratigraphic variation in each zone. Most notably, in **Figure 2.8b**, ice-wedges are a prominent feature in the subsurface of polygon throughs specifically at depths of 1.0- 1.2 m in the Transition Zone only. In contrast, in the Apex and Distal Zones, no ice wedges were detected in GPR data (**Figures 2.8a**, **2.8c**). In all radargrams, layered sediments are shown in the stratified traces in all line scans concentrated at the first 0 to 0.25 m of the soil as well as attenuation features that may be

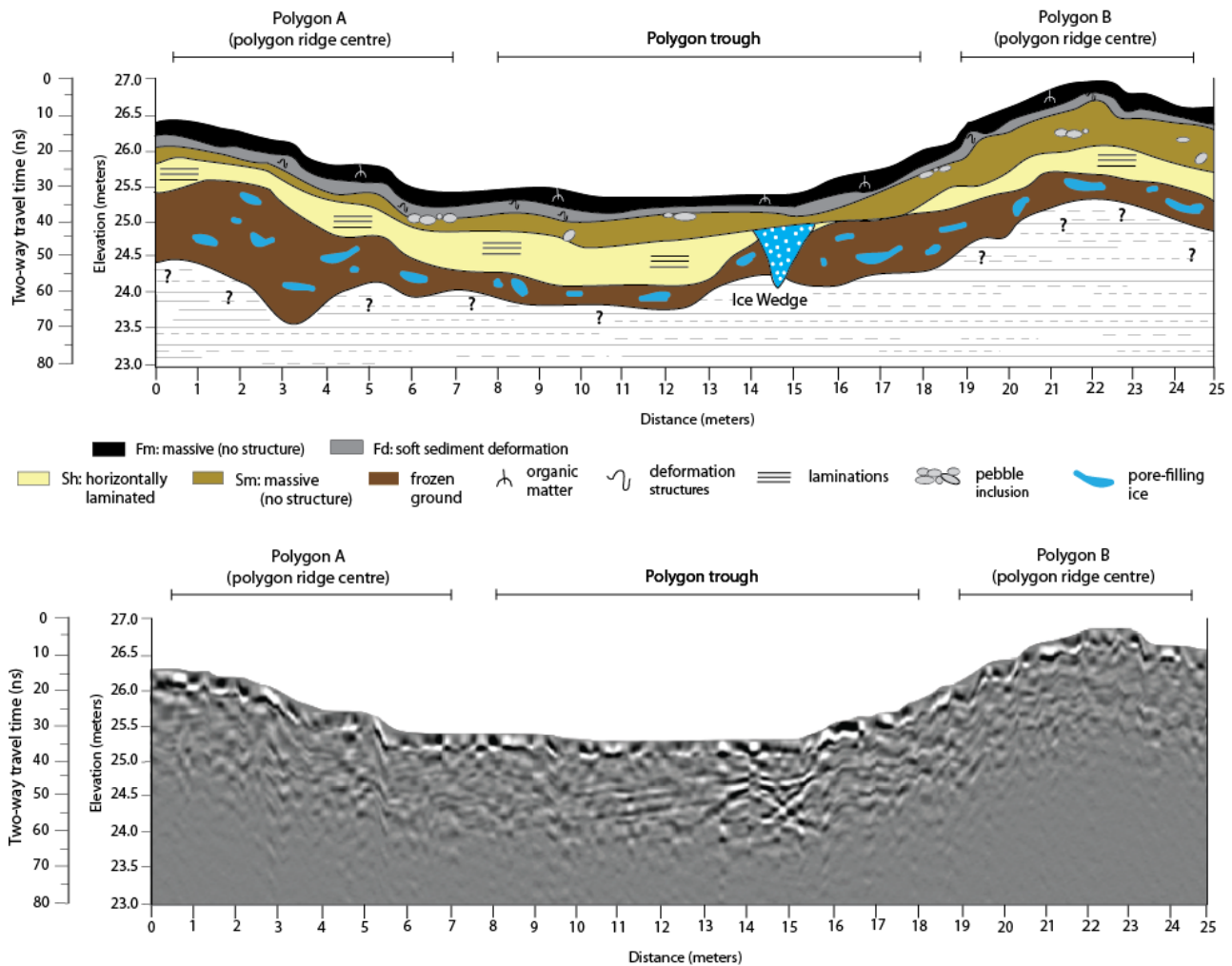
linked to water saturation and/or melting of the upper limit of the permafrost active layer. These three radargrams in adjacent zones within the study site corroborated details that were seen in the sedimentological pits and logs (**Figure 2.6**).



**Figure 2.8** Zonal GPR line radargrams for each designated fan region, locations are labeled in Figure 2.3. (A) Apex/Proximal Zone (GPR\_L1) showing subdued stratigraphy, collected up slope with no ice-wedges present. (B) Annotated Mid-Fan/Transition Zone (GPR\_L2) showing a cross-section of two ice-wedges below two polygon troughs. (C) Distal Zone (GPR\_L3) showing a continuous stratigraphic cross-section, no ice-wedges present.

In addition to the GPR lines in **Figure 2.8**, a detailed 25 m x 25 m GPR grid scan of GPR\_G1 in tandem with sedimentological ground-truthing of sediment pits were acquired to show more stratigraphic detail. The topographically corrected radargram in **Figure 2.9**

shows a single 25 m line profile within GPR\_G1 straddling two secondary high-centre polygons showing radar signatures of a single ice wedge inside the trough. At the first ~0.5-0.75 m, we see chaotic and oblique (non-parallel) radar signature returns that equate with deformed and massive fine silts with some organic matter/plant inclusions confirmed from trench excavations. The next 1.10 m (0.75 to 1.85 m) is composed of moderately continuous and wavy radar signatures that represents a combination of massive sands atop horizontally laminated fine-medium grained sands.

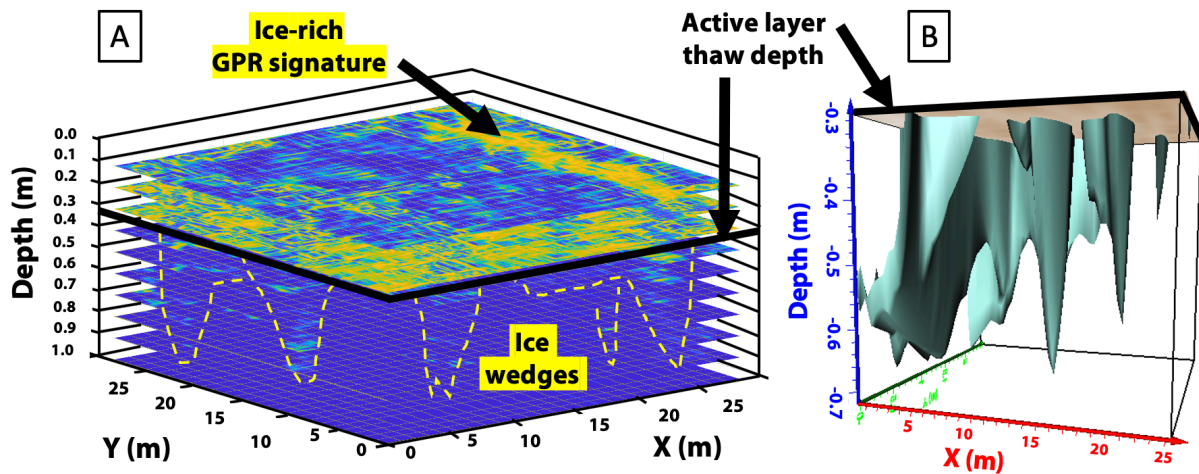


**Figure 2.9.** (Top) Stratigraphic reconstruction of an ice-wedge-polygon system within the Transition/Medial Zone using data from cross sections, GPR profiles and sedimentological



analyses. (Bottom) 25m GPR profile conducted at 250 MHz straddling polygons A and B within the 25m x 25m grid. Radargram interpretation has been incorporated into (Top)

In the study area (i.e., Transition Zone specifically), ice-wedge geometry and volume are of interest. Using a grid GPR array, in order to model the radar data in 3D, we present the results in two ways: (1) using a stacked MATLAB cube of 2-dimensional GPR depth slices down-stratigraphy and (2) using a Voxler isosurface/isovolume model with ice-wedge signals isolated and displayed (**Figure 2.4**).



**Figure 2.10.** (A) Stacked GPR depth slices rendered using MATLAB. Probable ice-rich areas and ice-wedges are highlighted in yellow mostly saturated in polygon troughs. (B) Voxler model of ice-wedge isosurfaces using isolated data from GPR radargrams. The active layer thaw depth is illustrated by the black bolded line in both images.

In **Figure 2.10a**, the strongest signals are found to be situated along polygon troughs, specifically radar returns on primary polygon troughs with secondary troughs showing the strongest returns. GPR signals are cross-cutting since this survey was done in an overlapping, bidirectional grid manner from E-W and N-S. Radargram signals in this stacked model abruptly stop at a depth of 0.3 cm, which is the depth range and location of common organic matter. Below 0.3 cm, radar signals gradually continue to travel in asymmetric, pyramidal forms until they reach signal attenuation at depths deeper than 1.0 m. These pyramidal forms are ice-wedges within primary and secondary cracks with

discontinuous morphologies that are correlated to the Transition/Medial Zone of the Strand Fiord alluvial fossil fan.

In **Figure 2.10b**, an isosurface was created in order to illustrate 3D shaded renderings from lattice files. An isosurface reflects the concept of a contour line (2D) and frames it in 3D space using matrices. Isosurfaces also display constant data values for a component that dissects a 3D volume, which in this case are the highest returns (filtered for ice-rich GPR signals). Using the Voxler 4 software, a 3D simulation of ice-wedges was modelled not only as a visualization tool but also as a calculator for subsurface ice volume (**Figure 2.10**). Volume calculations were generated from voxels (3D pixels) that are either partially or fully included in the isosurface. The total volume (isovalue) is the sum of the individual volumes from these voxels. Using this approach, the volume of the ice-rich isosurface within the 25 m x 25 m GPR survey grid has been calculated to contain 43.28 m<sup>3</sup> of ice. It is important to note that in both 3D-GPR subsurface ice-wedge models that ice-wedge morphology is complex.

## 2.5 Discussion

### 2.5.1 Surface Evolution: *Polygon Size Variation*

The size of polygons within this periglacial landsystem changes drastically from smaller sizes in the *Apex/Proximal Zone* to larger polygons in the *Distal Zone* (**Table 2.1**). We considered several possible explanations for the size variability between the two zones. First, this could be due to changes in grain size as mechanically, finer-grained material is more susceptible to contraction and cracking. Along with this, size distribution across the fan with bigger polygons situated in the *Distal Zone* could be due to their proximity to a thermal source (i.e. water in fiord or tributary). The larger polygons in the *Distal Zone* (**Table 2.1**, **Table 2.2**) may reflect slower thermal change (as the slowing kinetic river is a constant heat source), combined with the presence of finer material and the retention of moisture. Additionally, considering the thermal contraction rate at each zone, since the *Apex/Proximal Zone* is the oldest part of the alluvial fossil fan, sediments that have been deposited first at this zone are subject to thermal contraction given an earlier time frame of freezing and

contracting as opposed to the *Distal Zone*, which would have still been undergoing active flows. The freezing rate and contraction shape of sediments in each designated zone of the fan is directly related to the mechanical properties of the sediment.

Based on sedimentology and GPR evidence in all three zones of the fan, we suggest that in terms of age, the development of the polygonal network began in the uppermost sandy alluvial bars (**Unit B and C; Table 2.3; Figure 2.8**) of the alluvial plain after a high velocity event (i.e. mass wasting or change in seasonal flux in the tributary valley) that formed the alluvial fan. The presence of a heterogeneous mixture of both fine silts and medium-grained sands throughout these units indicate a deposition in a transition from a high to low energy condition, which transition into a lower energy fan conditions down-section. This change in heterogeneity relates to sediments exiting the feeder stream of the fan allowing sediment to no longer be confined to the channel walls. With this unconfinement, the sediments begin to naturally fan out especially at the *Transition/Medial Zone* allowing the shape of the fan to be influenced by other local factors other than merely topological features. In this outcrop, *Unit B*, is interpreted to be the general area where active layer thickening and permafrost melting are occurring due to exposure and edge thawing along the alluvial outwash plain. In this topographic setting and from analysis, a coarsening upwards sequence comprises the prograding fan with down-fan fining from fine- to medium-grained sands to fine silty clays. However, according to the bedrock cross-section of the valley (**Figure 2.2**), it can be delineated from the terraced topography of the valley that the braided river is receding and these terraces are steps of recession and thereby differential slopes. These differences in slope in a small, constrained locale (i.e. microtopography) not only control the preferential paths of polygon trough erosion via feeder streams in the spring, but also affects the drainage pathways for each of the three polygons zones depending on their position on the fan.

Since the *Fan Edge Zone* occurs at the far end of the alluvial fan, this in turn directly affects polygons within the distal slope of the fan (*Distal Zone*) as they are directly adjacent into various inputs from the trunk river. Polygon troughs at the distal zone are not only the largest in size but they also act as pathways for levees to incise the fan edge zone as shown in the exposed outcrop in **Figure 2.7**. By investigating the sedimentology of this ice-rich alluvial

fan, it helps to answer major questions in periglacial science: 1) *Is the size of the polygon indicative of grain size?* and (2) *Does underlying (bedrock) microtopography affect polygon formation via the existence of a “pseudobasin”?* In the context of this study, a pseudobasin is defined as a generalized concept of an underlying/re-routed hydrologic basin as a result of previous bedrock/sediment topography that has been overlain by sediment. From this study, it is interpreted that the size of polygons is fundamentally related to sediment grain size. In fact, due to the presence of finer material (silts/clays) in the *Distal Zone* where the largest polygon networks occur, this means that more moisture can be retained due to low sediment permeability, that enables ponding water to infiltrate directly. It is important to observe and determine material and mechanical sediment properties that are allowing the surface to either maintain sediment coherence or produce successive cracking and investigate the paleogeography of Strand Fiord with geotechnical surveying to confirm the presence of a pseudobasin underlying the *Transition/Medial Zone* that may be causing the formation of higher order polygons.

### 2.5.2 Surface Evolution: *Secondary Polygon Formation*

It is known that secondary polygon formation is a result of thermal contraction and a mixture of differential geothermal and substrate characteristics. Yet, the dynamics in higher order polygon networks (i.e. secondary, tertiary,  $n^{\text{th}}$  order polygons) such as in the *Transition/Medial Zone* in Strand Fiord helps to ask the question whether polygon network development is influenced by a feedback loop of causative factors enacting on the landsystem as a whole. It is important to not only consider the isolated study area, but a holistic approach to characterizing individual subsystem forefields and tracts, which contribute to the evolution of the alluvial fan and polygon system over time such as a possible pseudobasin microtopography (Snowdon, 2016), sediment facies associations, and 3D-GPR ice heterogeneity.

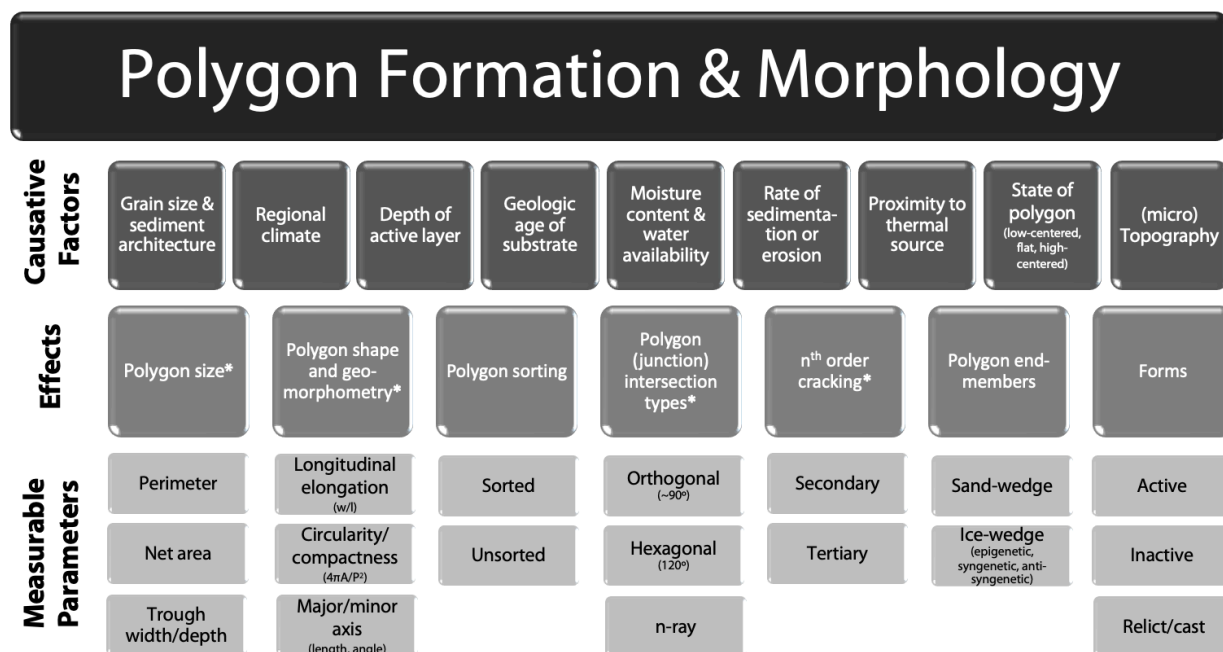
Out of all three classified zones within the Strand Fiord alluvial fossil fan, it is within the *Transition/Medial Zone* that the process of  $n^{\text{th}}$  order polygon trough subdivision is most prevalent in these high-centre (syngenetic) polygons, which could be due to a variety of causative factors. The *Transition/Medial Zone* of the fan experienced multiple episodes of

cracking and thermal contraction regimes resulting to the abundance of secondary, tertiary, and  $n^{\text{th}}$  order cracks at the present day (**Figure 2.3, Figure 2.6**). As cracking by primary wedges becomes progressively less frequent or ceases, new wedges initiate within a network to relieve the thermal stresses, forming secondary and even tertiary polygons (Mackay, 1974, 1992, 2000; Burn, 2004; Morse and Burn, 2012). At the study site, we theorize that secondary, tertiary, and  $n^{\text{th}}$  order polygon thermal contraction troughs are likely correlated with the presence and abundance of ice-wedges in the subsurface.

The *Apex/Proximal Zone* of the fan experienced a major thermal contraction event, which caused the deposited alluvial fan sediment to crack upon polygon formation due to thermal contraction regimes. This is evidenced through the Apex Zone polygon troughs in **Table 2.1** having only primary polygons present with the deepest troughs (i.e. the depths of the troughs may be associated with rapid cooling.) Thermal cracking is evidently generated by a combination of low temperature systems and by rapid cooling processes and could also be heavily influenced by differential snowpack cover in various parts of the fan, especially in the winter (Lachenbruch, 1962).

The *Transition/Medial Zone* is situated in the middle of an underlying bedrock terrace platform and has the lowest slope out of all zones. Another factor influencing the formation of secondary polygons in this zone is the underlying topography of the valley. This part of the fan is quite unique as it contains the largest amount of  $n^{\text{th}}$  order polygon trough subdivisions in the entire fan. We suggest that higher order polygon formation may be caused by the subtle microtopography, forming a permafrost pseudobasin inducing an environment for ice-wedges to form. To the west, we see a 3-step terrace from the fluvial regression of the valley trunk river however, to the east, at our study site, we see a smoothed slope from the alluvial fan deposition overlaying this 3-step topographic terrace, which could have some underlying microtopographic controls given its bedrock morphology (**Figure 2.2**). Overtime, successive cracking may have been due to the initiation of ice-wedge formation and replenishment within a trough allowing for prolonged thermal stress and rapid cooling to circumvent the polygon. Since, this zone is on a shallow-dipping stepped platform, it provides a more stable environment within the fan to attain high polygon cracking, growth,

and propagation velocities through time, thereby experiencing multiple episodes of trough incision and cracking (**Figure 2.6**). According to Fortier and Allard, 2004, the initiation of higher-order ice wedges may also be due to a change in the thermal-contraction coefficient of the ground as sediments are deposited. Furthermore, polygon formation and morphology in the Strand Fiord alluvial fossil fan is influenced by several factors. Although the aforementioned factors, are unique to this study area, **Figure 2.11** summarizes other key drivers of polygon evolution using a landsystem analysis approach. We will be exploring the surface formation and evolution of secondary polygons in relation to ice-wedge occurrence as well as an in-depth facies association in tandem with interpretations regarding the heterogeneity of ice in the subsurface.



**Figure 2.11.** A schematic flowchart of plausible polygon evolution. This chart outlines causative factors, effects, and measurable parameters when analyzing the formation and morphological processes of polygonal terrain. *\*Not limited to outlined measurable parameters. **NOTE:** Causative factors and effects are all independent of one another and can influence polygon morphology depending on their prominence/dominance in an environment.*

We suggest that another working hypothesis that controls polygon geomorphology is proximity to a thermal gradient (i.e. lateral thermal fluxes) within the periglacial landsystem. From the *Apex* to the *Distal* zone, the *Distal Zone* is closest in proximity to a large thermal source – the braided river basin that drains into Strand Fiord. This allows the subsurface closest to the river to distribute heat differently throughout the fan. The *Fan Edge Zone* outcrop occurs on an erosional slope as the alluvial fan would have been farther out upon deposition (**Figure 2.8; Table 3**). This unit exemplifies that the trunk valley river is a major contributor in terms of sediment load. *Units F and G* are of particular interest as the gravel horizons that these two units have are not only stratigraphically similar in grain size but also its deposition capping the fiord sand unit. *Units F and G* are likely sourced from fan deposition of modified fluvial deposits that represents the interface between the major braided river system and the alluvial fan that is more locally supplied with sediment by a smaller drainage basin of the fan. The gravel horizons represent pulses of fan activity in a cyclic manner that likely triggered surface flows of fine-medium sands and gravels. *Units E to G* are interpreted to be part of the trunk braided river system or a slumping event although no olistostromes or folded units of horizontal beds are present.

### 2.5.3 Heterogeneity of Distribution of Ice

Previous work has only been able to estimate and/or derive the amount of ice from GPR data using 2D profiles and numerical model propagations of the ice-wedge surface geometries (Munroe et al., 2007; Brosten et al., 2009; Schennen et al., 2016). Often, the term “3D-GPR” is used to define stacking several 2D radargram depth slices to form and interpolate a cube such as in **Figure 2.10a** without using a precise isosurface 3D software to encompass these strong isolated signals (e.g. ice-wedge body). The two 3D-GPR models presented in this study show that ice-wedge morphology is complex (**Figure 2.10**). Although situated in the continuous permafrost zone, limits and depths at which ice-wedges begin to form, grow, and pinch out need further investigation.

As mentioned in the methods, reflectors on the profile are identifiable at depths of ~1.0 m, thereby providing general stratigraphic and structural context. The radargram does not illustrate farther depths accurately as this is the thaw depth of the active layer, which is

most susceptible to signal attenuation due to the presence of the permafrost table. Although in planview the radargram profiles appear as chevron-shaped intersections (**Figure 2.8b** and **Figure 2.9**), there is a clear three-dimensional asymmetry to these forms that are highly dependent on *slope*, *sediment matrix permeability* (for water seepage), as well as *stratigraphic discontinuities* for preferential sites of ponding, in which ice-wedges could begin to grow larger and assume expansive and more complex morphologies (**Figures 2.8** **2.10**). Syngenetic, epigenetic, and anti-syngenetic ice-wedges have commonalities in which, they are all dependent on permafrost dynamics during warm and cool periods (MacKay 1990; French 2007). As a result of a cold climate, permafrost degrades and, therefore, ice-wedge truncation and cessation of cracking dominates. In addition, 3D-ice-wedge asymmetry may be associated with cold periods during the wintertime when permafrost aggrades, cracks, and ice wedges are rejuvenated via preferential polygon trough pathways (Kasper and Allard, 2001). The chevron-shaped vertical cross section of an ice wedge is also a function of both horizontal and vertical growth that covers three axes of rejuvenation or decay (Mackay, 1990, 2000; Morse and Burn, 2012). It is important to note that through 3D-GPR, ice-wedge morphology is modelled as a complex V-shaped mass of subsurface ice within polygon troughs, specifically more prominent on secondary and tertiary high centre polygons, that are asymmetric and laterally discontinuous in geometry.

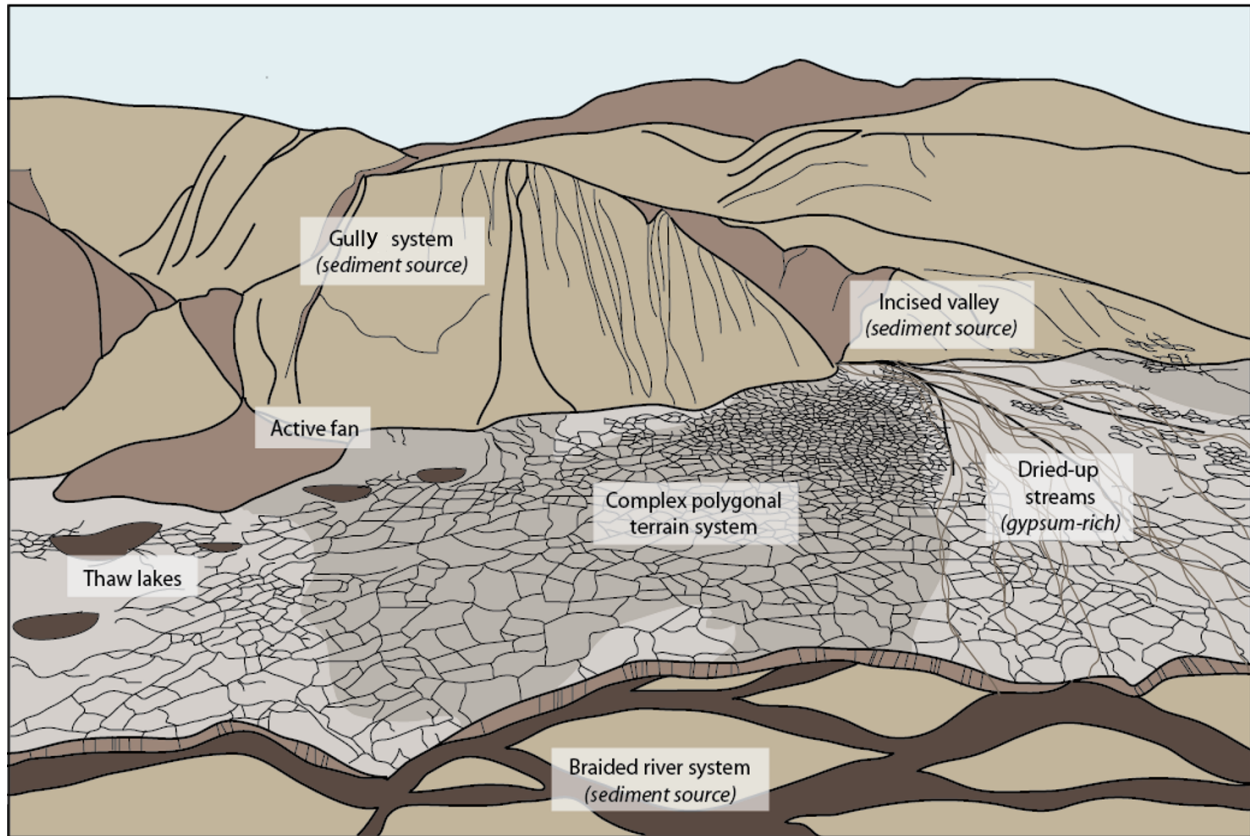
3D modelling of GPR data can be limited by several factors, two of which are near-surface water and mineral concentration. Due to the soil's conductive nature, the GPR signals get attenuated before they can return to the antenna when travelling through damp or wet soils, especially when they have high salt content. GPR data is a crucial tool to validate cored-and-cached samples that may be indicative of paleoenvironments. To validate these GPR models it is supplemented with sedimentological evidence such as sedimentological log of the *Fan Edge Zone* along with the rest of the zonal sediment pits in order to ground truth features present on the GPR scan (**Figure 2.7**, **Figure 2.8**). The sedimentological columns strongly validate the depth of the active layer at 0.6 m and the ice-wedge at 0.8 m as seen on both 3D-GPR models in the *Transition/Medial Zone*. Thus, further subsurface investigations must be done in order to determine whether polygon surface expression can



be indicative of ice-wedge volume due to the fact that the polygon morphology and sedimentology variations in the three zones within the Strand Fiord alluvial fossil fan, may or may not be ice-rich.

#### 2.5.4 Periglacial Landsystem Model

We have identified three distinct zones with differing polygon morphologies that occur in a relatively small and constrained locale of the alluvial fossil fan. At the Strand Fiord alluvial fossil fan, differences among these zones are driven by confounding processes, namely (i) slope, (ii) sediment grain size/permeability, (iii) trough depth and continuity, (iv) moisture content, (v) state and age of polygon, and (v) lateral thermal flux source that play a significant role in polygon morphology and evolution (**Figure 2.11**). This can be used as a process-form proxy to analyze individual polygonal forms as they appear in different morphologies in various landsystem environments, implying different evolution regimes. Although, different landsystems, composed of smaller landsystem units or tracts differ in environmental constituents, there are also a variety of controlling factors that affect the temporal evolution and development of each landsystem (**Figure 2.11; Figure 2.12**).



**Figure 2.12.** Schematic diagram to illustrate landsystem constituents which are characteristic of a periglacial, alluvial-dominated landsystem. This is the current stage of sedimentation and evolution of Strand Fiord alluvial fossil fan.

Trough depth is of high importance due to the fact that these well-developed troughs are preferential sites of accumulation and precipitation flow/pooling. As an ice-wedge builds up within the troughs of these high-centred polygons, snow will stay in the *Apex/Proximal Zone* longer due to topographic location. Additionally, the slight bowing of troughs in other regions such as the *Transition/Medial Zone* may be related to where ice-wedges may be found. The valley walls of Strand Fiord are also north-facing, meaning that there may be prominent shadow near the walls close to the *Proximal/Apex Zone* that allow for prolonged snow coverage and minimal sun coverage. Despite having well-developed ramparts on either side of polygons, the continuity of these troughs allows the rerouting of feeder streams into inclined topographic troughs.

At the Strand Fiord alluvial fossil fan, as cracking by primary wedges becomes progressively less frequent or ceases, new episodic network cracking initiates within that primary polygon in order to relieve the thermal stresses, forming higher order polygons (Mackay, 1974; Mackay, 1992, Mackay 2000; Burn, 2004). With widened troughs, these secondary and tertiary polygon troughs form a positive feedback loop system enabling precipitation and accumulation to preferentially seep into the subsurface forming ice-wedges. The *Transition/Medial Zone* shows an increased initiation of ice-wedges, which may not only be due to the trough depth, but also changes in the thermal-contraction coefficient of the ground as sediments of various grain sizes are deposited and transported into the feedback system (Fortier and Allard, 2004). The coefficient of thermal expansion describes how the grain size can change responding to a change in temperature. Specifically, it measures the fractional change in size per degree change in temperature at a constant pressure.

We suggest that slope, sediment grain size, proximity to lateral thermal flux sources, and permeability are among of the most significant controlling factors in the Strand Fiord alluvial fossil fan. As the fan progrades from coarser sands to finer silts and clays (*Apex/Proximal Zone* to *Distal Zone*), this also means that sediment permeability decreases down-fan. Precipitation in any form is then able to soak into substrate more easily at the *Apex/Proximal Zone* and more water ponding occurs in the *Distal Zone*. Thus, less moisture percolates down as you go down-fan. Since the *Apex/Proximal Zone* is more permeable (sands), there is more infiltration into the subsurface. Since the *Distal Zone* is less permeable (fine silty clay), there is more ponding water that is not able to infiltrate the subsurface directly affecting the delivery and availability of moisture. With this, it can be deduced that sediment grain size may perhaps be directly correlated to polygon size.

## 2.6 Conclusions

A comprehensive methodology combining the use of sedimentological, geophysical, and remote sensing techniques allowed a robust periglacial landsystem analysis of the Strand Fiord alluvial fossil fan. The Strand Fiord alluvial fossil fan has an abundance of primary, secondary, and  $n^{\text{th}}$  order networks of syngenetic, high centre polygonal patterned ground.

The distribution and scale of landsystem tracts within the study site resembles active, cold and dry environments commonly found within the Canadian High Arctic.

Our study demonstrated major findings that the primary network of contraction cracks and ice wedge polygons originated in the sand and gravel bars of the alluvial outwash plain (*Unit B*; **Figure 2.8**). From coarser sands to finer silty-clays (*Apex/Proximal, Mid-fan/Transition, to Distal Zones*), the size of the polygons increases inversely proportional to the grain size downslope of a well-sorted alluvial fan. With this, 3D-GPR modelling of ice-wedges also revealed the discontinuity and asymmetry of ice-wedge morphology and geometry and calculated a total ice volume of 43.28 m<sup>3</sup> within GPR\_G1 which has an areal size of 625 m<sup>2</sup> (**Figures 2.8, 2.9, and 2.10**). While the *Transition/Medial Zone* revealed the presence of ice-wedges; ice-wedges were absent in the Apex and Distal zones.

Multiple characteristics of the polygons, bedrock and their topography contribute to the distinctive differences between the morphologies and evolution of the three closely located polygonal zones. The moisture and content availability, depth of active layer, grain size, and proximity to a thermal source play a significant role in the response of a polygonal system to climate, and therefore their formation as distinctive zones. In fact, the underlying terraced bedrock topography reset and overlain by the alluvial fan, may be a major driving factor to polygon formation due to its potential topographic source of drainage as a pseudobasin for precipitation seepage and pooling.

These periglacial landsystems can be used as analogues for the interpretation of ancient mass deposits of a flow on the margins and slopes of Holocene to Pleistocene deglaciated valleys. The landsystem at Strand Fiord alluvial fossil fan does not conform to that of other sloped periglacial landscapes (i.e. Mackenzie delta), though it shares similarities with ice-wedge systems in independent climate zones (Morse and Burn, 2012; Fortier and Allard, 2005; Allard and Kasper, 1998). The classification code used in this study created consistency between the periglacial analysis of the sedimentology of three different polygonal zones. This system can be applied in future landsystems studies to improve the consistency of terminology to describe geocryology with a more substrate-focused

approach and therefore increasing the comparability of studies completed in different research locations and by different researchers.

This study gives insight to periglacial landsystems and their significance not only for high Arctic and planetary analogue science but hopes to bridge some gaps between planetary science and periglacial geomorphology. Periglacial geomorphology is quite complex due to the long and slow active processes occurring in the subsurface scale as well as the inability to openly access the subsurface and investigate these processes with high resolution, non-invasive techniques. To date, there has been no record of ice-wedge polygon ice volume calculation using isosurface generation using 3D-GPR let alone modelling the size and shape morphology of the ice wedges themselves. Along with stratigraphic correlation and landsystem analysis techniques, a proposition of a periglacial landsystem hypothesis is presented with implications for near-surface permafrost ice dynamics and in-situ resource utilization with a specific focus on polygonal patterned ground networks.

## 2.7 References

- Ballantyne, C.K. and Matthews, J.A., 1983. Desiccation cracking and sorted polygon development, Jotunheimen, Norway. *Arctic and Alpine Research*, 15(3), pp.339-349.
- Bawden, M.P., 1967. Applications of aerial photography in land system mapping. *The Photogrammetric Record*, 5(30), pp.461-464.
- Benito, G., Sopena, A., Sánchez-Moya, Y., Machado, M.J. and Pérez-González, A., 2003. Palaeoflood record of the Tagus River (central Spain) during the Late Pleistocene and Holocene. *Quaternary Science Reviews*, 22(15-17), pp.1737-1756.
- Billings, W.D. and Peterson, K.M., 1980. Vegetational change and ice-wedge polygons through the thaw-lake cycle in Arctic Alaska. *Arctic and Alpine Research*, 12(4), pp.413-432.
- Brosten, T.R., Bradford, J.H., McNamara, J.P., Gooseff, M.N., Zarnetske, J.P., Bowden, W.B. and Johnston, M.E., 2009. Estimating 3D variation in active-layer thickness beneath arctic streams using ground-penetrating radar. *Journal of Hydrology*, 373(3-4), pp.479-486.
- Burn, C.R., 2004. A field perspective on modelling 'single-ridge' ice-wedge polygons. *Permafrost and Periglacial Processes*, 15(1), pp.59-65.
- Burn, C.R. and O'Neill, H.B., 2015. Subdivision of ice-wedge polygons, western Arctic coast. *Canadian Geotechnical Society*, Quebec, QC.
- Cheel, R.J. and Rust, B.R., 1986. A sequence of soft-sediment deformation (dewatering) structures in Late Quaternary subaqueous outwash near Ottawa, Canada. *Sedimentary Geology*, 47(1-2), pp.77-93.
- Cooke, R.V. and Doornkamp, J.C., 1990. *Geomorphology in environmental management: a new introduction*. Oxford University Press (OUP).
- Dostovalov, B.N. and Popov, A.I. 1966. Polygonal systems of ice-wedges and conditions of their development, Permafrost International Conference 1963, Lafayette, Indiana. National Academy of Sciences – National Research Council, Washington, DC. Publication 1287: 71-76.
- French, H.M., 2017. *The periglacial environment*. John Wiley & Sons.

- Fortier, D. and Allard, M., 2004. Late Holocene syngenetic ice-wedge polygons development, Bylot Island, Canadian arctic archipelago. *Canadian Journal of Earth Sciences*, 41(8), pp.997-1012.
- Giles, D.P., Griffiths, J.S., Evans, D.J.A. and Murton, J.B., 2017. Geomorphological framework: glacial and periglacial sediments, structures and landforms. Geological Society, London, *Engineering Geology Special Publications*, 28(1), pp.59-368.
- Haltigin, T.W., Pollard, W.H., Dutilleul, P. and Osinski, G.R., 2012. Geometric evolution of polygonal terrain networks in the Canadian High Arctic: Evidence of increasing regularity over time. *Permafrost and Periglacial Processes*, 23(3), pp.178-186.
- Lachenbruch, A.H., 1962. Mechanics of thermal contraction cracks and ice-wedge polygons in permafrost (Vol. 70). Geological Society of America.
- Levy, J., Head, J. and Marchant, D., 2009. Thermal contraction crack polygons on Mars: Classification, distribution, and climate implications from HiRISE observations. *Journal of Geophysical Research: Planets*, 114(E1).
- Kasper, J.N. and Allard, M., 2001. Late-Holocene climatic changes as detected by the growth and decay of ice wedges on the southern shore of Hudson Strait, northern Québec, Canada. *The Holocene*, 11(5), pp.563-577.
- Mackay, J.R., 1974. Ice-wedge cracks, Garry Island, Northwest Territories. *Canadian Journal of Earth Sciences*, 11(10), pp.1366-1383.
- Mackay, J.R., 1990. Some observations on the growth and deformation of epigenetic, syngenetic and anti-syngenetic ice wedges. *Permafrost and Periglacial Processes*, 1(1), pp.15-29.
- Mackay, J.R., 1992. The frequency of ice-wedge cracking (1967–1987) at Garry Island, western Arctic coast, Canada. *Canadian Journal of Earth Sciences*, 29(2), pp.236-248.
- Mackay, J., 2000. Thermally induced movements in ice-wedge polygons, western Arctic coast: a long-term study. *Géographie physique et Quaternaire*, 54(1), pp.41-68.
- Morse, P.D., Burn, C.R. and Kokelj, S.V., 2012. Influence of snow on near-surface

- ground temperatures in upland and alluvial environments of the outer Mackenzie Delta, Northwest Territories. *Canadian Journal of Earth Sciences*, 49(8), pp.895-913.
- Munroe, J.S., Doolittle, J.A., Kanevskiy, M.Z., Hinkel, K.M., Nelson, F.E., Jones, B.M., Shur, Y. and Kimble, J.M., 2007. Application of ground-penetrating radar imagery for three-dimensional visualisation of near-surface structures in ice-rich permafrost, Barrow, Alaska. *Permafrost and Periglacial Processes*, 18(4), pp.309-321.
- Mutch, T.A., Binder, A.B., Huck, F.O., Levinthal, E.C., Liebes, S., Morris, E.C., Patterson, W.R., Pollack, J.B., Sagan, C. and Taylor, G.R., 1976. The surface of Mars: The view from the Viking 1 lander. *Science*, 193(4255), pp.791-801.
- Schennen, S., Tronicke, J., Wetterich, S., Allroggen, N., Schwamborn, G. and Schirrmeister, L., 2016. 3D ground-penetrating radar imaging of ice complex deposits in northern East Siberia. *Geophysics*, 81(1), pp.WA195-WA202.
- Teltewskoi, A., Beermann, F., Beil, I., Bobrov, A., De Klerk, P., Lorenz, S., Lüder, A., Michaelis, D. and Joosten, H., 2016. 4000 years of changing wetness in a permafrost polygon peatland (Kytalyk, NE Siberia): A comparative high-resolution multi-proxy study. *Permafrost and Periglacial Processes*, 27(1), pp.76-95.
- Washburn, A.L., 1973. *Periglacial processes and environments*. London: E. Arnold



## Chapter 3

### 3 Utility of Hyper-Resolution LiDAR for Patterned Ground Geomorphometry in the Houghton River Valley, Devon Island, Nunavut

#### 3.1 Introduction

The formation of patterned ground is common in periglacial environments where the ground undergoes recurrent freezing and thawing producing various morphologies. The term *patterned ground* is used to describe terrain that exhibits regular (sorted) or irregular (unsorted) surface patterning and geometry. Patterned ground is one of the most evident characteristics of cold regions – it is one of the most particularly less-understood phenomena of sediment/rock self-arrangement (Blau, 2003). Patterned ground has been documented in numerous domains on Earth namely, on *recently glaciated terrain* (i.e. the Canadian High Arctic; Ballantyne and Matthews, 1982, 1983; Matthews et al., 1998; Haughland, 2004, 2006), *proximal to late lying snow patches* (Kling 1997), in *supraglacial debris covers* and even *frontal glacial moraines* (Ballantyne, 1997; Kerguellec, 2014), on *seasonally flooded ground*, and *under shallow water* (Lauriol et al., 1985) and even on *other planets* such as Mars (Mangold et al., 2004; Levy et al., 2009). In this study, relationships and constituent mechanisms of patterned ground formation along with their role in landscape evolution are explored with periglacial geomorphology. The patterned ground complex is uniquely distributed in permafrost environments, and only a few studies have explored modelling the distribution, development, and spatial relationship/evolution of these features in a constrained local environment (i.e. Hjort and Luoto, 2016; Heilbronn, DWH Walton, 1984; Boike and Yoshikawa, 2003). The transition and relationships amongst these differing patterned ground morphologies is important on a landsystem level in order to further characterize the changes and processes that are occurring on the top of the surface and subsurface. It is uncommon to find various types of patterned ground in a small and constrained locale or environment.

Different types of patterned ground in active periglacial environments include sorted and unsorted patterned ground. Sorted patterned ground has been proposed to form through

differential frost heave generated by recurrent freezing and thawing of moist, frost-susceptible soil containing abundant clasts (Washburn 1956; Ballantyne, 2013). Non-sorted patterned ground is also formed through differential frost heave of moist, frost-susceptible soil, but without concentration of clasts (Giles et al., 2017; Washburn, 1956; Hallet, 1990; Hutchinson, 1991; Ballantyne, 2013; Murton, 2013). The shape of patterned ground occurs either as patches of cryoturbated, frost-heaved bare soil and/or as sorted arrangements of distinctly coarse and fine sediment. Patterns may occur as single units or as groups of units. Nonetheless, cryoturbation is one of the dominant periglacial processes that involve frost heaving and up-freezing of soil, increase in cryostatic pressure, and thaw settlement (Van Vliet-Lanoë, 1988; van Huissteden, 2020). Subsurface water and its redistribution during freezing and thawing cycles, along with the formation of ice lenses, results to the tendency for different particle sizes to heave at different rates (Hallet, 1990). The presence of frost-susceptible sediment lithologies in correlation with tensile stress also plays an important role in the redistribution of soil moisture during freezing and segregated ice lens formation. However, for the purposes of this study only, *polygons*, *stone circles/closed crenulations*, *sorted networks/mud boils*, and *stripes*, are the main patterned ground morphology types of focus.

*Polygons* are macroscale, honeycomb like patterns that are produced by thermal contraction cracking in continuous permafrost zones, which are often associated with the formation of intersecting networks and vertically oriented ice veins called *ice-wedges* (Washburn, 1980). *Stone circles* are circular arrangements of coarse-grained material associated with finer material sorted in the middle and the coarser material sorted radially outwards forming an elevated shoulder/halo. This association between stone circles and fine-/coarse- grained material is widely recognized, and reflects the fine soil texture experiencing frost heaving, which gives rise for the development of relief and the segregation of material according to size that characterizes sorted patterned ground (Washburn, 1980; Kessler et al., 2001; Hallet, 2013). It is important to note that stone circles in this study are asymmetric in shape in comparison to the conventional stone circle models, which may be due to several confounding factors (Kessler et al., 2001). *Mud boils* or *frost hummocks* are types of non-sorted circles. Current numerical models of patterned ground invoke the convection cell

mechanics theory as part of their formational process, just like stone circles. Lastly, *stone stipes* are lines of stones, vegetation, and/or sediment that typically form from transitioning steps on slopes at angles of 2-7° (Ballantyne, 2001; King, 1971). These elongated morphologies are unique to periglacial environments and are characteristic landforms in hill slope areas (Peterson, 1983). Sorted and non-sorted circles, polygons, nets occur predominantly on flat surfaces (<3° slope) and patterned ground shapes tend to become more elongated at gradients between 2-7° (Washburn, 1956). Overall, patterned ground associated with cryoturbation is common in regions of intensive frost action and occurs in both permafrost and areas of deep seasonal frost along with other contributing processes or factors in the local environment.

Patterned ground processes such as differential frost heave (uplift of soil due to volume increase; Washburn, 1980) and buoyancy-induced convection (Swanson et al., 1999) are often associated with specific patterned ground phenotypes. Consequently, there are different factors that contribute to the evolution and differing geometries of patterned ground with *topography* and *lithology* as major factors. The development of sorting involving the upward and outward movement of relatively coarser sediment radially, has been broadly used as a circulatory model to describe sorted patterned ground formation using measurements of soil and clast displacements (Kessler et al., 2001). Moreover, *differential frost heave*, *mass movement*, *buoyancy-induced convection*, and *wind activities* are major mechanical processes that highly affect the formation of patterned ground (Thorn et al., 1992; Ballantyne, 2018).

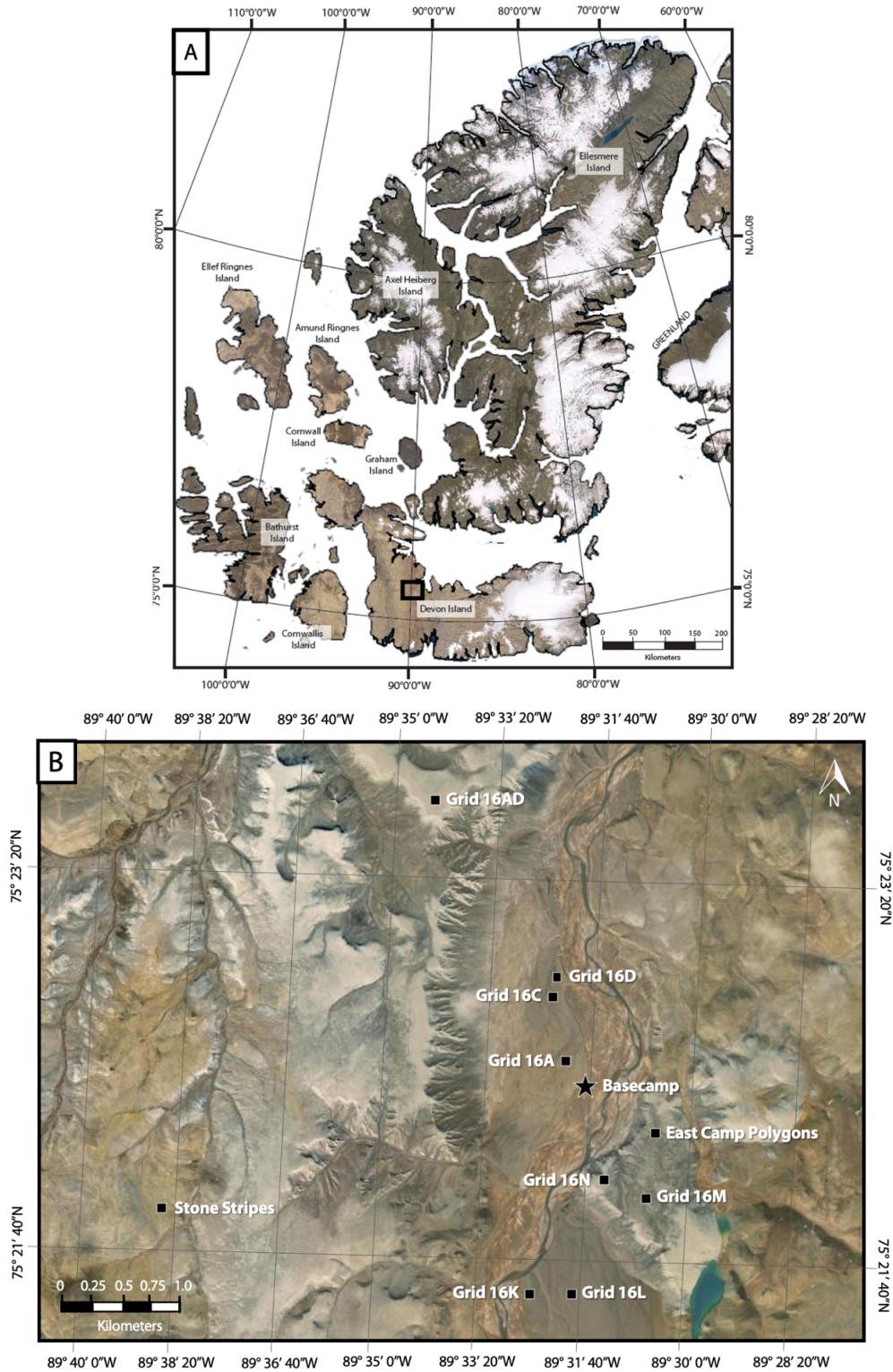
In this study, we explore the use of hyper-resolution LiDAR technology in correlation with GIS and image analysis techniques to investigate the connectivity and relationships of different types of patterned ground within different lithological settings. This study helps to answer the questions: (1) *Are different patterned ground phenotypes dependent on substrate type?* (2) *With a landsystem approach, is there a relationship of connectivity between different patterned ground morphologies?* And if so, (3) *Can variations in patterned ground sorting and surface process-evolution be derived from hyper-resolution LiDAR?* The overarching goal of this study is to characterize and quantify morphological differences in

various types of patterned ground constrained in a small locale using remote sensing and lithological sampling via fieldwork in order to build a more consistent periglacial landsystem model of the Canadian High Arctic.

## 3.2 Study Area

The region of interest is located in the Haughton River Valley (HRV) in the Haughton impact structure, Devon Island (75.37°, -89.53°; **Figure 3.1**). The Haughton Impact Structure is a 23-km diameter, 23 Myr impact crater that formed in ~1.9 km of sedimentary rocks of the Arctic Platform overlying Precambrian crystalline basement (Thorsteinsson and Tozer 1970; Douglas 1970; Osinski et al., 2005). The present-day outcrop of the Haughton structure lies entirely within carbonate strata of the Upper Ordovician Allen Bay Formation as well as volumetrically dominant crater-fill, clast-rich impact melt rock specifically containing a calcite anhydrite-silicate glass groundmass (Osinski et al., 2005).

The Haughton Impact Structure, Devon Island lies within a polar desert with a mean annual temperature of approximately -16°C and mean annual precipitation of less than 200 mm (Boon et al., 2010). Within this, the HRV is a unique locale within the eastern portion of the Haughton impact structure that houses a variety of periglacially modified patterned ground types. It is a fluvially eroded 1.5 km wide valley with gullied terraces incising the valley walls from the plateau tops with a river draining into Jones Sound. To date, the Haughton Impact Structure poses as the best preserved and best exposed complex impact structure with active periglacial processes, making it a significant planetary analogue target.



**Figure 3.1.** (A) Context map of the Haughton Impact Structure, Devon Island, Nunavut. (B) An Annotated map of the Haughton River Valley study site and grid sites within the localized zone. Basecamp in labeled in a black star for reference.

### 3.3 Methods and Data Collection

Light Detection and Ranging (LiDAR) remote sensing data was collected in summer 2016 as part of a 4-week field campaign and data was completely processed in 2017 into measurable digital elevation models (DEMs) from the raw data. Along with this, a follow-up ground-truthing and sedimentological sampling survey was undertaken in the summer of 2019.

#### 3.3.1 Remote Sensing Field Methods: Light Detection and Ranging (LiDAR)

In this study, we use a novel mobile kinematic LiDAR, named the Akkha3W system in order to achieve the highest possible topographic resolution. Using the Akkha3W system, we are able to process and generate digital elevation models (DEMs) with an unprecedented resolution of 0.1 to 0.5 meters. LiDAR data were processed using Cloud Compare and ArcMap LAS toolbox interfaces to create a total of 36 LiDAR DEM datasets. Nine grids displaying diverse patterned ground morphology were chosen for further analysis (**Table 3.3**). The shapes and forms on these LiDAR grids were then digitized following the parameter that they were sloed shapes.

**Table 3.1.** Coordinates of the nine LiDAR Grids in the Haughton River Valley used for this study. The latitudes and longitudes of the 9 grids are listed in Decimal Degrees and UTM meters and the map projection is UTM 16N, WGS 84.

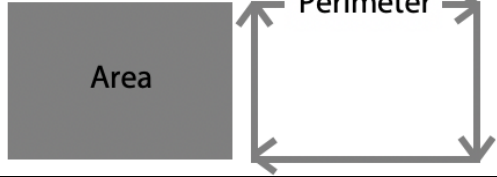
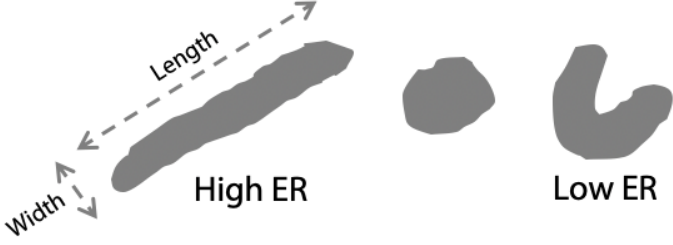
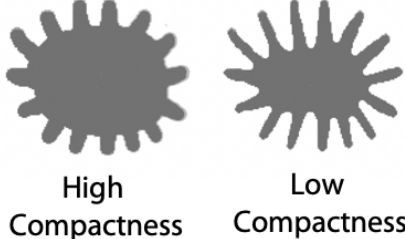
<b>Grid</b>	<b>Lat UTM</b>	<b>Long UTM</b>	<b>Creation Time</b>	<b>Elevation (m)</b>
16A (0.1m/px)	8367099	428554	2016-07-20T16:49:10Z	98.85
16C (0.1m/px)	8367504	428529	2016-07-20T17:33:27Z	94.96
16D (0.1m/px)	8367644	428565	2016-07-20T17:58:25Z	93.17
16K (0.1m/px)	8365195	428257	2016-07-22T17:04:57Z	108.77
16L (0.1m/px)	8365174	428525	2016-07-22T16:56:28Z	110.58
16N (0.1m/px)	8366051	428803	2016-07-22T18:57:25Z	134.93

16AD (0.1m/px)	8369103	427651	2016-07-27T16:40:21Z	197.52
Stone Stripes (0.5m/px)	8365883	425145	2016-07-29	176.45
East Camp Polygons (0.5m/px)	8366440	429239	2016-07-29	117.04

### 3.3.2 Geomorphometric Image Analysis

Image analysis was used to quantify and characterize the shape of various periglacial patterned ground phenotypes. Shape measurements were acquired using manual digitizing on ArcMap 10.7.1 along with the calculation of the following shape descriptors: (1) *Diameter*, (2) *Area*, (3) *Perimeter*, (4) *Elongation ratio*, and (5) *Compactness*. Equations and elementary diagrams are described in **Table 3.2** for each shape descriptor. The diameter is defined as the longest distance between two points in a closed shape; The area is defined as the number of pixels within a shape; The perimeter (or length) is the number of pixels in the boundary of the object; Elongation ratio (ER) is the ratio between the length and width of the object bounding box – If ER equals 1, then the object is roughly square or circularly shaped. As the ratio decreases from 1, the object becomes more elongated with ER equals 0 being a fully elongated straight line; the compactness (area-to-perimeter ratio) is the ratio of the area of an object to the area of a circle with the same perimeter – If the compactness equals 1, then it is a rounder feature however, measures of compactness are often insensitive to irregular and abrupt boundary changes. It is also important to note that the entire grid area had been mapped manually and that patterned ground is not evenly widespread throughout the study areas. Therefore, each grid has empty, non-mapped areas that may result in some error when producing spatial analysis maps (i.e. typically shown in black for no data; **Figures 2.3-2.11**).

**Table 3.2.** Elementary diagrams and equations for shape descriptors used for patterned ground analysis.

Shape descriptor	Definition	Schematic
Area	$4\pi r^2$ (2)	
Perimeter	$\sum_{i=1}^{N-1}  x_i - x_{i+1} $ (3)	
Elongation ratio (ER)	$\frac{\text{minor axis}}{\text{major axis}}$ (4)	
Compactness	$\frac{4\pi (\text{Area})}{(\text{Perimeter})^2}$ (5)	

### 3.3.3 Kernel Density Estimation (KDE)

Analyzing spatial and geometric variances in patterned ground is a main component of this study. Kernel density estimation (KDE) is an effective method for visualizing the distribution of event density over time and/or space but is underutilized in geomorphological data analysis (Cox, 2007; Maclachlan and Eyles, 2013; Vermeesch, 2007). Statistically, KDE is a non-parametric way to estimate the probability density function of a random variable. The distance of influence of the kernel, or area included in the density analysis, is determined by the user and is referred to as the bandwidth (Cox, 2007). Kernel estimation was used to create a map of patterned ground density values in which the density at each location reflects the concentration of points representing the geometric centres of patterned ground. Specifically, KDE plots of elongation ratio and area are plotted side-by-side in order to compare if there is a direct correlation between topography, elongation, and area.



### 3.3.4 Lithological Mapping

A geologic map was generated using ArcGIS (10.8) to correlate the nine grids to specific lithologies (**Figure 3.2**). With a combination of GIS and fieldwork techniques, the nine grid coordinate points (study areas) were also overlain on this geologic map, but further sampling was done in order to ground truth and collect grain size and permafrost active layer thaw depth measurements. Grain size and sample analysis has yet to be carried out with the collected samples using geotechnical lab protocols in order to extract: the *thermal conductivity, heat capacity, hydraulic conductivity, porosity, plastic/liquid limits, specific gravity, dry density, salinity (if any), electrical conductivity, and unfrozen water content*. These variables all play a significant role in thermal contraction-expansion, which is at the root of polygonal systems and patterned ground morphology. The occurrence of different types of patterned ground is dependent on several factors however, due to the general remote sensing scope of this chapter, and little access to grain size analysis facilities during the COVID-19 shutdowns, sedimentological analysis has been postponed.

## 3.4 Results

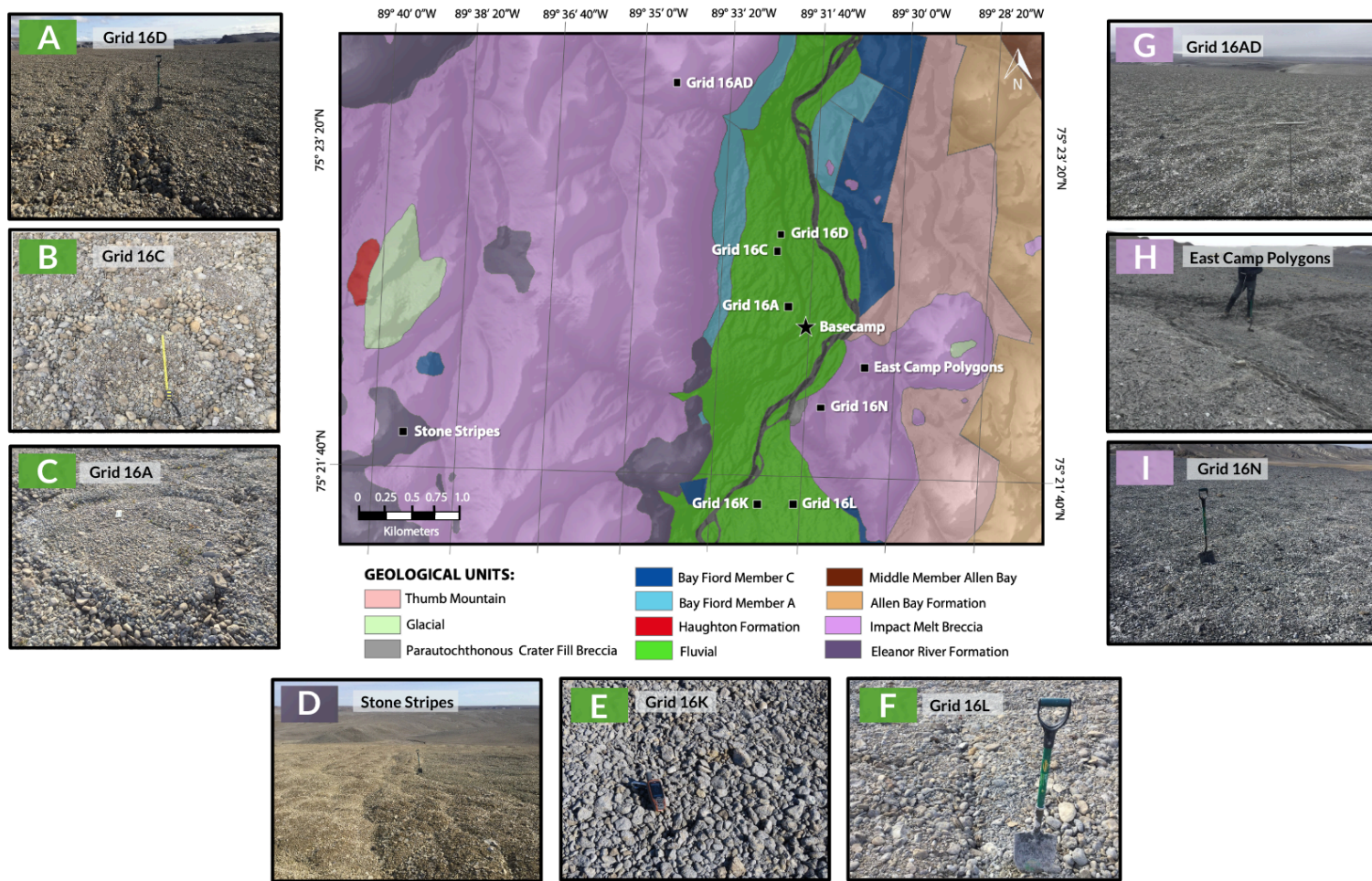
### 3.4.1 General Lithology, Remote Sensing Observations and Quantification

The nine LiDAR grids collected in 2016 are distributed across the Houghton River Valley (HRV) and were randomly targeted due to their unique surface field expression, which are situated in 3 major geologic units: Eleanor River Formation, Impact Melt Rock, and Fluvial Sediments (**Figure 3.2**). The Stone Stripes grid is the only LiDAR scan that is on the Eleanor River Formation, which consists of resistant, thick bedded limestone with recessive dolomite (Christie, Embry and Van Dyck, 2003). Grids 16AD, 16N, and the East Camp Polygons LiDAR Scan are all housed within the Impact Melt Rock lithology, while Grids 16A, 16C, 16D, 16K, and 16L are all situated in the Fluvial lithology. Geomorphometric statistics were collected and calculated (**Table 3.3**), to show the variations between the shape descriptor parameters in all the LiDAR grids as well as a robust image vector and KDE analysis of the patterned ground (**Figures 2.3-2.11**).

**Table 3.3.** Summary chart of geomorphometric statistics of patterned ground in the HRV (**Note:** Long axis azimuth values range from 0-180, 90 trending E-W and 180 trending N-S)

	Parameters	Min	Max	Sum	Mean	Std Dev.
	<b>Stone Circles Grid 16A (n=230)</b>	Diameter (m)	0.37	3.31	18.21	1.2
Area (m <sup>2</sup> )		0.14	10.96	331.59	1.44	1.49
Perimeter (m)		1.31	17.38	1055.30	4.59	2.51
Elongation ratio		0.16	1.00	167.66	0.73	0.18
Compactness		0.22	0.99	182.40	0.79	0.16
Long Axis Azimuth (°)		0	179.71	20567.02	89.42	54.98
<b>Stone Circles Grid 16C (n=1384)</b>		Parameters	Min	Max	Sum	Mean
	Diameter (m)	0.17	3.56	34.93	0.94	1.12
	Area (m <sup>2</sup> )	0.03	12.69	1220.11	0.88	1.26
	Perimeter (m)	0.69	19.28	4800.09	3.47	2.59
	Elongation ratio	0.18	1.00	1011.80	0.73	0.19
	Compactness	0.20	0.99	1104.89	0.80	0.17
	Long Axis Azimuth (°)	0	179.65	113725.80	82.17	52.35
<b>Stone Circles Grid 16D (n=912)</b>	Parameters	Min	Max	Sum	Mean	Std Dev.
	Diameter (m)	0.26	2.15	23.21	0.77	0.80
	Area (m <sup>2</sup> )	0.07	4.64	538.84	0.59	0.64
	Perimeter (m)	0.99	13.88	2610.22	2.86	1.66
	Elongation ratio	0.13	1.00	630.59	0.69	0.19
	Compactness	0.21	0.99	763.41	0.84	0.16
	Long Axis Azimuth (°)	0	179.62	67928.79	72.48	60.03
<b>Crenulations Grid 16K (n=202)</b>	Parameters	Min	Max	Sum	Mean	Std Dev.
	Diameter (m)	0.25	2.21	10.60	0.75	0.81
	Area (m <sup>2</sup> )	0.06	4.90	112.46	0.56	0.66
	Perimeter (m)	0.87	20.87	654.68	3.24	2.58
	Elongation ratio	0.14	1.00	132.52	0.66	0.21
	Compactness	0.13	0.99	143.86	0.71	0.23
	Long Axis Azimuth (°)	0	178.52	11613.88	57.49	48.17
<b>Stone Circles Grid 16L (n=1130)</b>	Parameters	Min	Max	Sum	Mean	Std Dev.
	Diameter (m)	0.22	2.71	19.47	0.58	0.58
	Area (m <sup>2</sup> )	0.05	7.32	378.92	0.34	0.34
	Perimeter (m)	0.80	14.26	2344.98	2.08	0.96
	Elongation ratio	0.17	1.00	874.62	0.77	0.17
	Compactness	0.27	0.99	1039.02	0.92	0.10
	Long Axis Azimuth (°)	0	178.59	95499.48	84.51	58.29
<b>Frost-shattered hummocks Grid 16N (n=366)</b>	Parameters	Min	Max	Sum	Mean	Std Dev.
	Diameter (m)	0.33	2.52	18.51	0.97	0.89
	Area (m <sup>2</sup> )	0.11	6.36	342.59	0.94	0.79
	Perimeter (m)	1.43	11.60	1377.24	3.76	1.57
	Elongation ratio	0.28	1.00	268.85	0.73	0.17
	Compactness	0.30	0.73	203.78	0.56	0.07
	Long Axis Azimuth (°)	0	179.14	29299.24	80.05	53.35

<b>Grid 16AD (n=392)</b>	<b>Parameters</b>	<b>Min</b>	<b>Max</b>	<b>Sum</b>	<b>Mean</b>	<b>Std Dev.</b>
	<b>Diameter (m)</b>	0.26	2.18	19.17	0.97	0.85
	<b>Area (m<sup>2</sup>)</b>	0.07	4.76	367.66	0.94	0.73
	<b>Perimeter (m)</b>	0.94	10.98	1487.63	3.79	1.80
	<b>Elongation ratio</b>	0.15	0.99	269.22	0.69	0.20
	<b>Compactness</b>	0.25	0.99	310.20	0.79	0.15
	<b>Long Axis Azimuth (°)</b>	0	179.21	27752.19	70.80	56.10
<b>Stone Stripes (n=273)</b>	<b>Parameters</b>	<b>Min</b>	<b>Max</b>	<b>Sum</b>	<b>Mean</b>	<b>Std Dev.</b>
	<b>Diameter (m)</b>	1.40	16.35	95.69	5.79	6.25
	<b>Area (m<sup>2</sup>)</b>	1.97	267.38	9156.11	33.54	39.09
	<b>Perimeter (m)</b>	5.00	152.33	8555.78	31.34	29.50
	<b>Elongation ratio</b>	0.07	1.00	136.30	0.50	0.39
	<b>Compactness</b>	0.08	0.99	170.43	0.62	0.31
	<b>Long Axis Azimuth (°)</b>	0.09	175.81	23897.84	87.54	37.09
<b>East Camp Polygons (n=55)</b>	<b>Parameters</b>	<b>Min</b>	<b>Max</b>	<b>Sum</b>	<b>Mean</b>	<b>Std Dev.</b>
	<b>Diameter (m)</b>	17.52	48.67	234.76	31.37	21.25
	<b>Area (m<sup>2</sup>)</b>	306.89	2368.82	55112.13	983.86	451.71
	<b>Perimeter (m)</b>	75.63	209.50	6911.26	125.66	31.02
	<b>Elongation ratio</b>	0.41	0.98	39.46	0.72	0.13
	<b>Compactness</b>	0.59	0.91	41.50	0.75	0.09
	<b>Long Axis Azimuth (°)</b>	11.00	176.06	3599.53	65.44	51.71



**Figure 3.2.** A general overview of the distribution and location of the nine 1cm (topographic pixel spacing) LiDAR grids that were scanned in the Haughton River Valley (HRV) showing their relative lithology. (A), (B), (C), (E), and (F) are stone circles, (G) and (I) are mud boils, (H) are polygons, and (D) are stripes. LiDAR digital elevation models are analyzed in detail in next figures following this spatial distribution. *Note:* Grids in this figure are organized based on the geologic unit and their location in the HRV.

## Stone circles: *Grids 16A, 16C, 16D, 16K and 16L*

Grids 16A, 16C, 16D, 16K, and 16L are all located along the fluvial valley of the HRV and show a wide distribution of stone circle morphologies. Amongst all the grids, these grids occur at lowest elevation being situated on the valley floor of the incised river valley. Sediments were composed of sub- to well-rounded cobbles and a light brown sandy matrix (**Figures 3.2a, b, c, e and f**). The particle size ranges from 0.5 cm to 18 cm in diameter with the most evident sorting shown with the finer clasts sorted in the middle and the larger clasts forming the ridge around the stone circles and at times arranged in crenulated patterns along polygon troughs. The active layer thaw depth was unreachable at these sites due to the abundance of pebbles and cobbles, but is estimated to be  $>1.0$  m.

Stone circles in Grid 16A were digitized and statistically quantified in order to have measurable outputs. With a total sample size of 230 stone circle morphometries, the general size of a stone circle in this grid has a mean area of  $1.44 \text{ m}^2 \pm 1.49$  along with a mean elongation ratio of  $0.73 \pm 0.18$  and a mean compactness value of  $0.79 \pm 0.16$  (**Table 3.3; Figure 3.3**). Among all the different stone circle variations within the HRV, Grid 16A exemplifies the largest stone circle sizes (**Figure 3.2 and 3.3**). Most stone circles are situated in the upper right-hand corner of the grid where there are relatively higher elevations with the larger sized stone circles situated in the lower elevations. The elevation transition or difference between the maximum (98.01 m.a.s.l.) and minimum (96.57 m.a.s.l.) is 1.44 m throughout the entirety of Grid 16A.

With a total sample size of 1384, the stone circle morphometries of Grid 16C have a mean area of  $0.88 \text{ m}^2 \pm 1.26$  along with a mean elongation ratio of  $0.73 \pm 0.19$  and a mean compactness value of  $0.80 \pm 0.17$  (**Table 3.3; Figure 3.4**). Among all the different stone circle variations within the HRV, Grid 16C has the most widespread distribution of stone circles with respect to both quantity and geometric aspects. The largest stone circles are situated in the northern part of the grid where there are relatively lower elevations, while the smallest stone circles are situated in the higher elevations. The elevation transition or difference between the maximum (96.47 m.a.s.l.) and minimum (95.62 m.a.s.l.) is 0.85 m.

throughout the entirety of Grid 16C. This indicates less than a meter change in elevation in this grid, while exemplifying different morphometric variations with such a subtle change in topography.

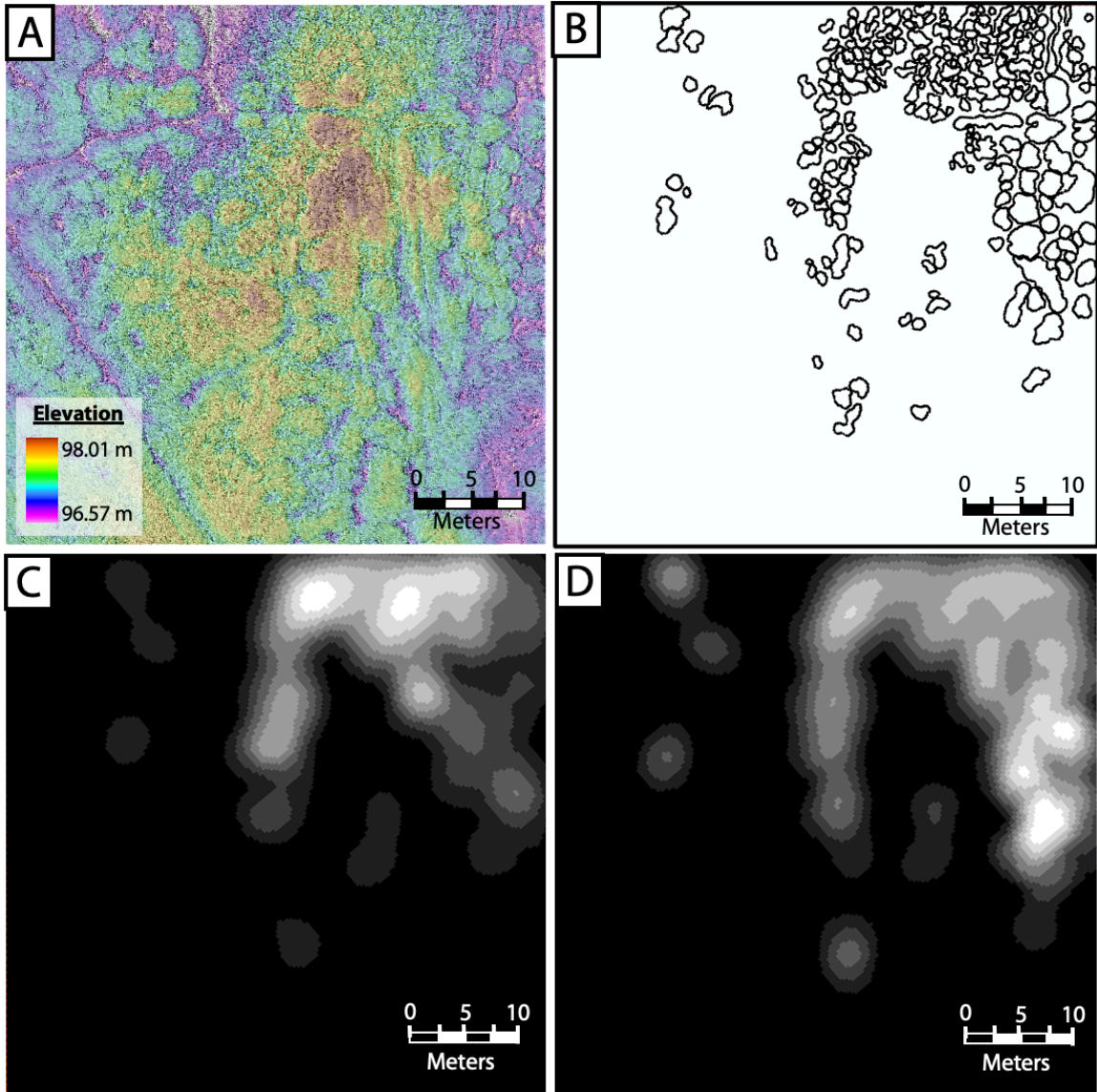
With a total sample size of 912 stone circle morphometries, Grid 16D has a mean area of  $0.59 \text{ m}^2 \pm 0.64$  along with a mean elongation ratio of  $0.69 \pm 0.19$  and a mean compactness value of  $0.84 \pm 0.16$  (**Table 3.3; Figure 3.5**). Grid 16D is one of the more unique grids in the HRV due to the fact that these digitized stone circles occur within a field of larger thermal contraction polygons or a network of tensile fractures resulting from thermal stresses in frozen ground (Harris et al. 1988) – patterned ground within patterned ground. The most elongated stone circles are situated along the edges of polygons within the grid independent of elevation. The elevation transition or difference between the maximum (96.45 m.a.s.l.) and minimum (95.06 m.a.s.l.) is 1.39 m. throughout the entirety of Grid 16D.

There is a total sample number of 202 circles within Grid 16K. The grid has a mean area of  $0.56 \text{ m}^2 \pm 0.66$  along with a mean elongation ratio of  $0.66 \pm 0.21$  and a mean compactness value of  $0.71 \pm 0.23$  (**Table 3.3; Figure 3.6**). In comparison to the rest of the grids in HRV, Grid 16K does not necessarily have fully formed and well-defined stone circles such as in Grids A, C, and D. Instead, geomorphologically, it appears more crenulated and arcuate in form with some degree of irregularity, while also being situated within polygonal terrain. The elevation transition or difference between the maximum (103.09 m.a.s.l.) and minimum (102.30 m.a.s.l.) is 0.79 m throughout the entirety of Grid 16K.

Grid 16L has a total sample size number of 1130 stone circles. The stone circles in this grid have a mean area of  $0.34 \text{ m}^2 \pm 0.34$  along with a mean elongation ratio of  $0.77 \pm 0.17$  and a mean compactness value of  $0.92 \pm 0.1$  (**Table 3.3; Figure 3.7**). Grid 16L is adjacent to Grid 16K and in comparison, to each other, Grid 16L has more defined stone circles than Grid 16K, which exemplifies some crenulated patterns. Although they are well defined, Grid 16L houses the smallest and most compact stone circles along the fluvial valley, with respect to stone circles. The elevation difference between the maximum (107.65 m.a.s.l.)

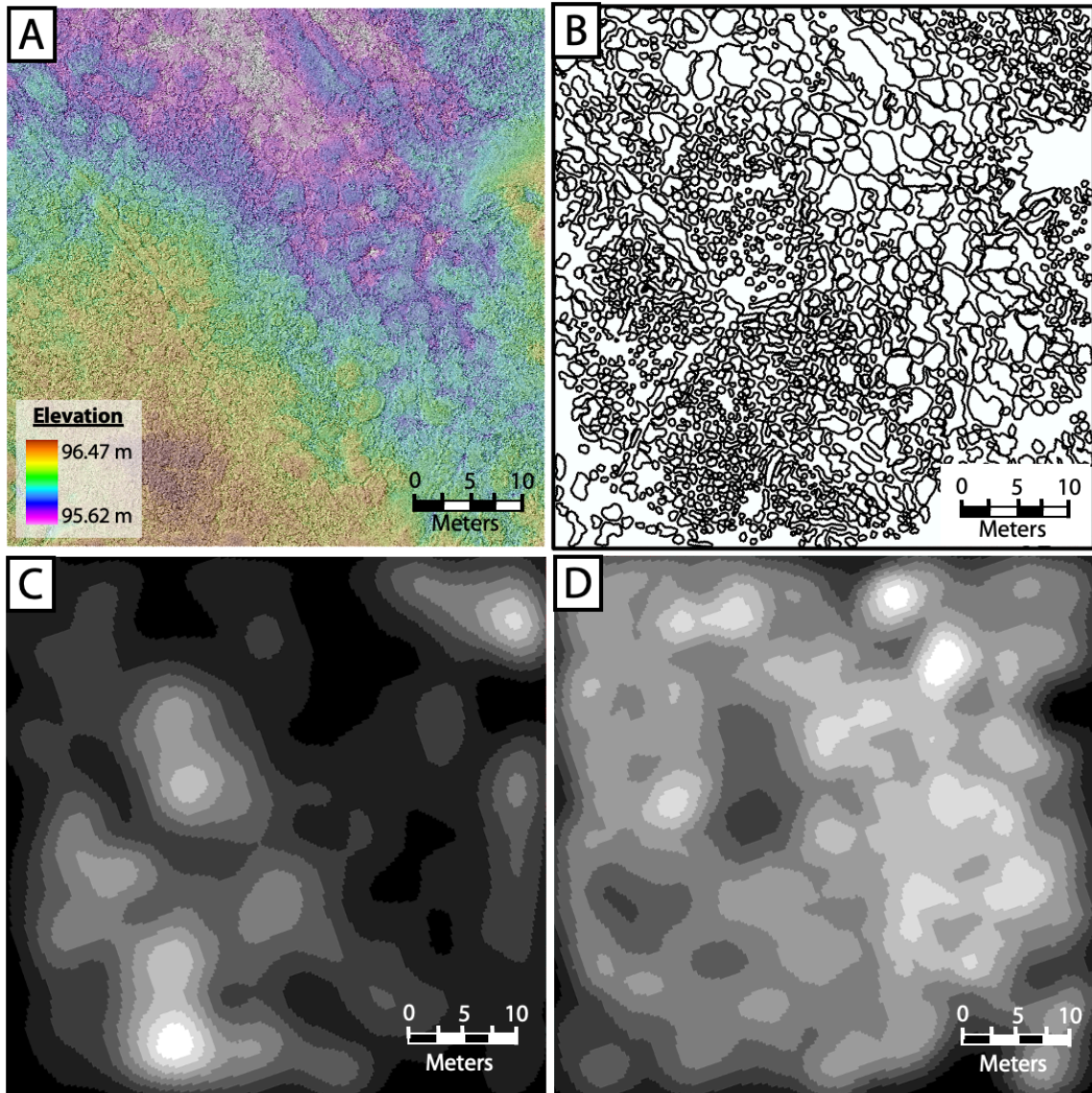


and minimum (106.89 m.a.s.l.) is 0.76 m throughout the entirety of Grid 16L. Similar to Grids 16C and 16K downstream, this indicates less than a meter change in elevation in this grid with very drastic changes in stone circle geomorphology and organization.



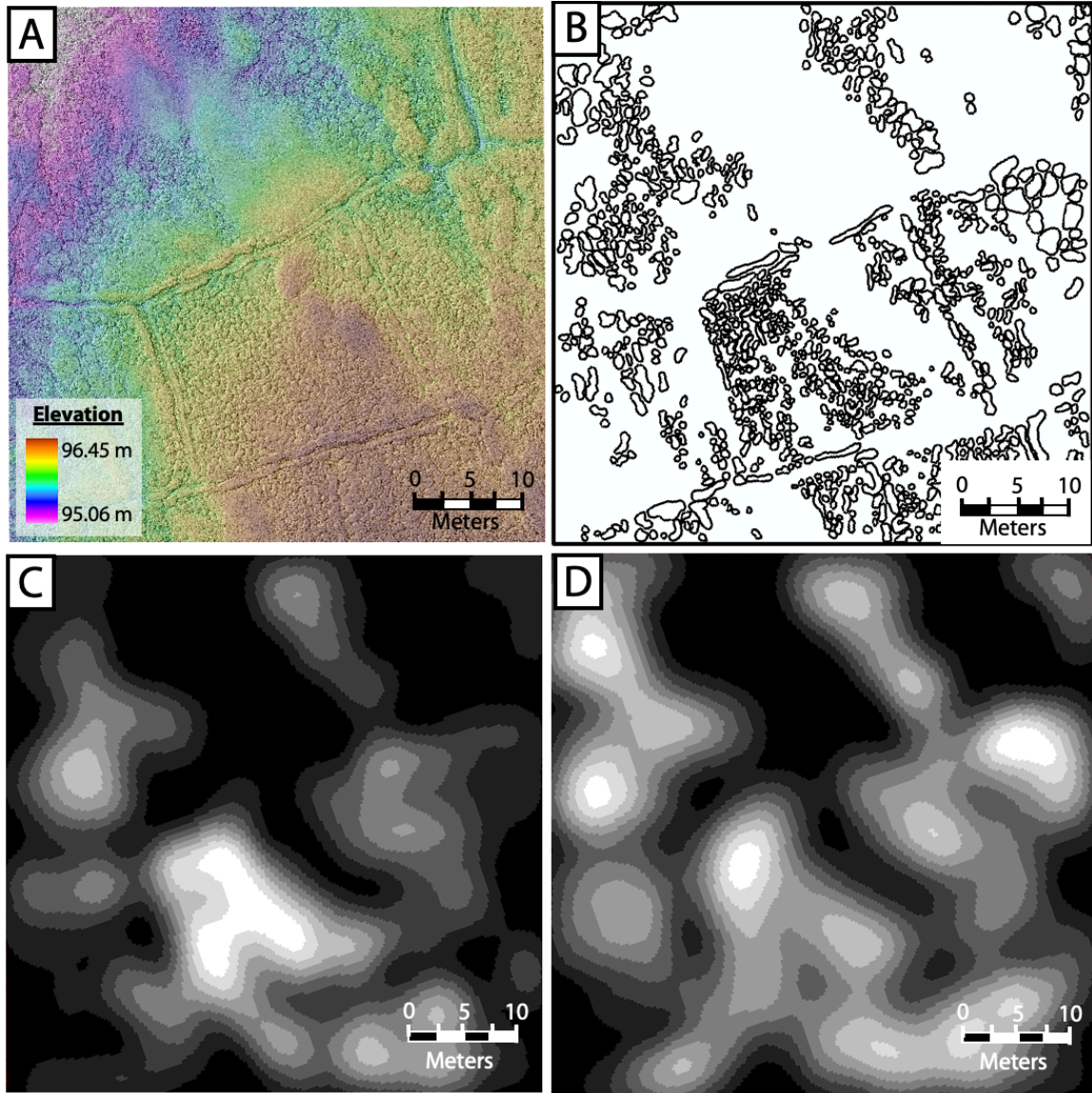
**Figure 3.3.** (A) LiDAR digital elevation map showing topographical variations on a centimeter scale for stone circles. (B) Mapped stone circle geometries in Grid 16A. (C) KDE model of the elongation ratio of Grid 16A stone circles. Lowest elongation ratio values (values closer to 0) that show more elongated features are shown in dark grey with the lighter shades signifying higher elongation ratios (values closer to 1), which are more

equally rounded features. **(D)** KDE model of the area of stone circles in Grid 16A. Larger areas are indicated by white and smaller areas are indicated by the darker shades.

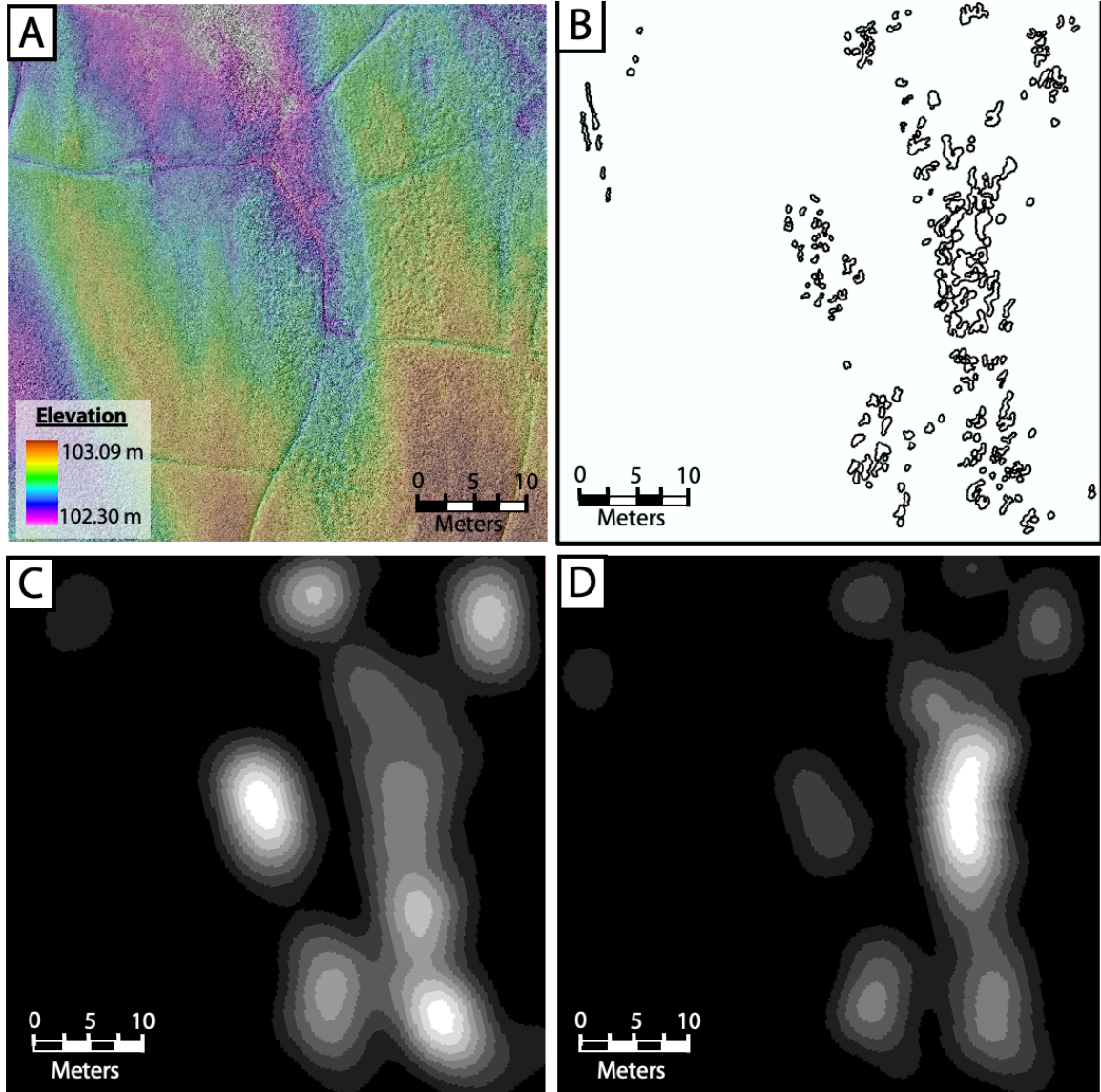


**Figure 3.4.** **(A)** LiDAR digital elevation map showing topographical variations on a centimeter scale for stone circles. **(B)** Mapped stone circle geometries in Grid 16C. **(C)** KDE model of the elongation ratio of Grid 16C stone circles. Lowest elongation ratio values (values closer to 0) that show more elongated features are shown in dark grey with the lighter shades signifying higher elongation ratios (values closer to 1), which are more equally rounded features. **(D)** KDE model of the area of stone circles in Grid 16C. Larger areas are indicated by white and smaller areas are indicated by the darker shades.

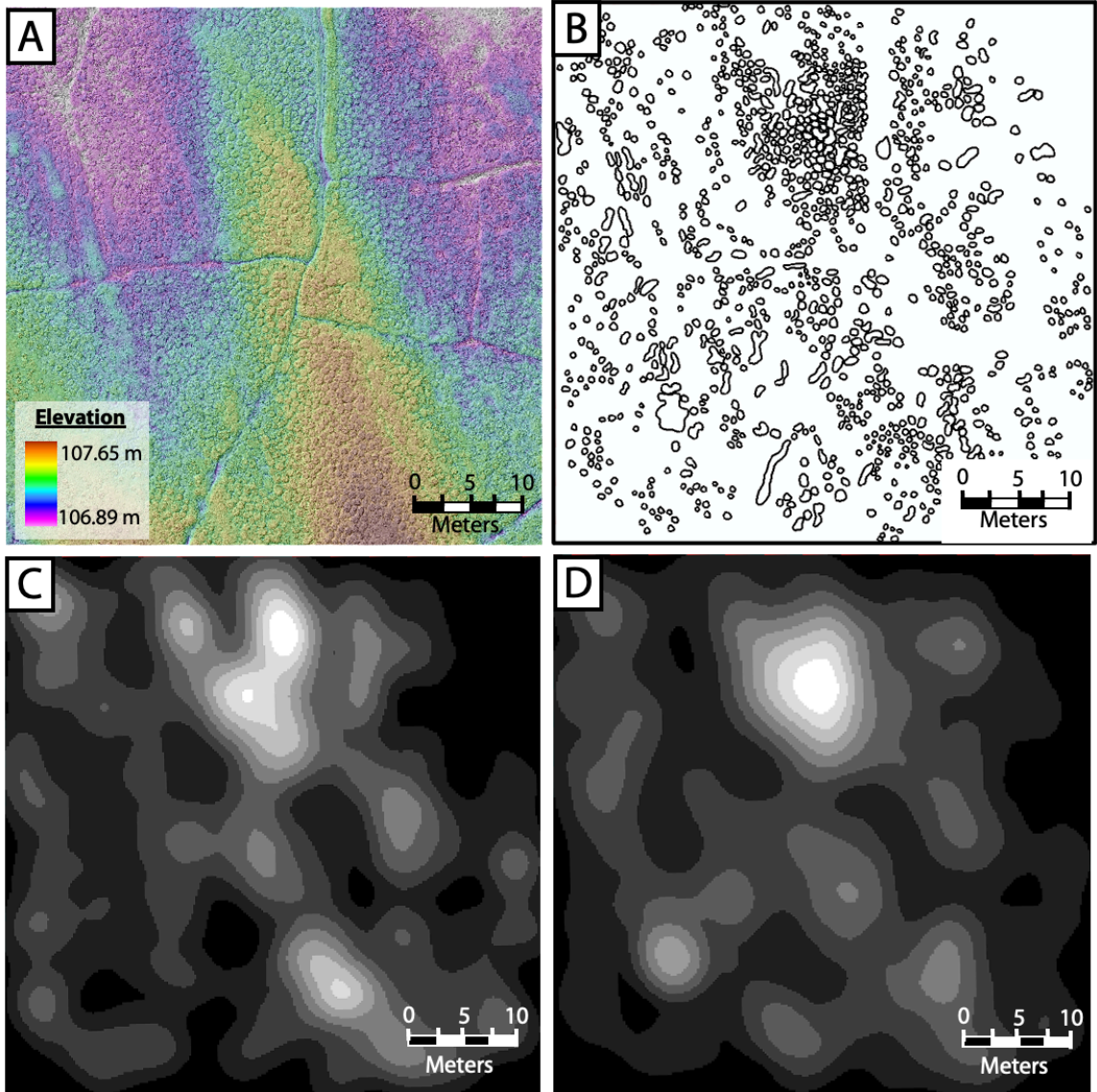




**Figure 3.5.** (A) LiDAR digital elevation map showing topographical variations on a centimeter scale for stone circles. (B) Mapped stone circle geometries in Grid 16D. (C) KDE model of the elongation ratio of Grid 16D stone circles. Lowest elongation ratio values (values closer to 0) that show more elongated features are shown in dark grey with the lighter shades signifying higher elongation ratios (values closer to 1), which are more equally rounded features. (D) KDE model of the area of stone circles in Grid 16D. Larger areas are indicated by white and smaller areas are indicated by the darker shades.



**Figure 3.6.** (A) LiDAR digital elevation map showing topographical variations on a centimeter scale for stone circles. (B) Mapped stone circle geometries in Grid 16K. (C) KDE model of the elongation ratio of Grid 16K stone circles. Lowest elongation ratio values (values closer to 0) that show more elongated features are shown in dark grey with the lighter shades signifying higher elongation ratios (values closer to 1), which are more equally rounded features. (D) KDE model of the area of stone circles in Grid 16K. Larger areas are indicated by white and smaller areas are indicated by the darker shades.



**Figure 3.7.** (A) LiDAR digital elevation map showing topographical variations on a centimeter scale for stone circles. (B) Mapped stone circle geometries in Grid 16L. (C) KDE model of the elongation ratio of Grid 16L stone circles. Lowest elongation ratio values (values closer to 0) that show more elongated features are shown in dark grey with the lighter shades signifying higher elongation ratios (values closer to 1), which are more equally rounded features. (D) KDE model of the area of stone circles in Grid 16L. Larger areas are indicated by white and smaller areas are indicated by the darker shades.



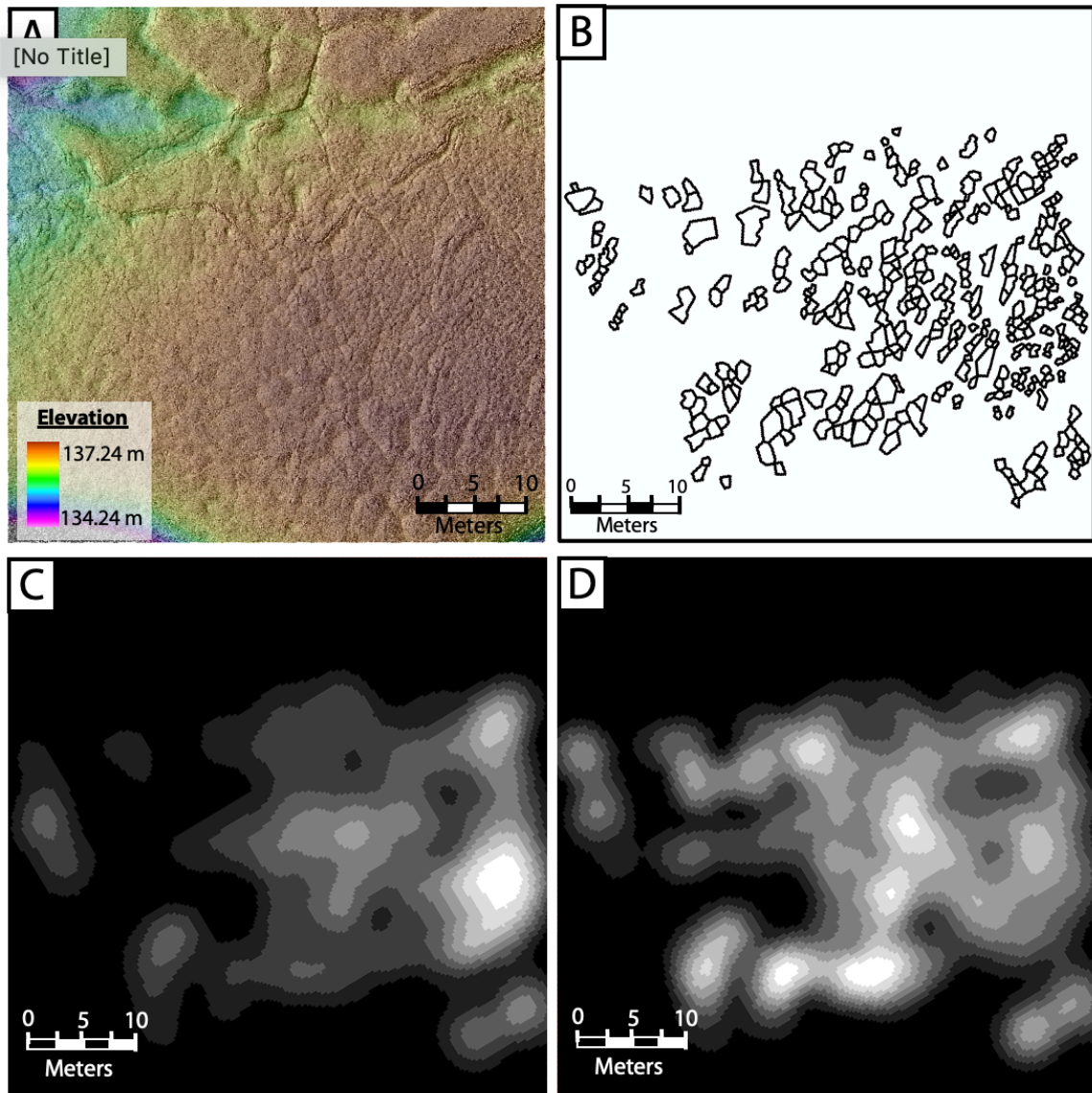
## Mud boils and Frost-shattered nets: *Grids 16N and 16AD*

Grids 16N and 16AD are situated on plateau tops on the western and eastern portion of the valley walls within the study site respectively. They are the two grids with the highest elevation with Grid 16N located at 197.52 m.a.s.l. and Grid 16AD located at 134.93 m.a.s.l. (**Table 3.3**). Geologically, Grid 16N is located on the eastern portion of HRV within the Impact Melt Rock unit and Grid 16AD is located on the north-western portions of HRV (**Figure 3.2g, 3.2i; Figure 3.8**). Both grids exhibit the formation of mud boil nets with poorly sorted, subangular substrate with cobbles ranging from 1 cm to 17 cm in diameter. The active layer thaw depth of the permafrost in Grid 16N was 0.67 m and Grid 16AD was 0.52 m.

Grid 16N exemplify mud boil features or sometimes referred to as frost shattered hummocks. There is a total of 366 mapped samples of mud boils in Grid 16N with a mean area of  $0.94 \text{ m}^2 \pm 0.79$  (**Table 3.3; Figure 3.8**). Mud boil geometry shows that Grid 16N has an overall mean elongation ratio of  $0.73 \pm 0.17$  and a mean compactness of  $0.56 \pm 0.07$ . A major difference between mud boils geometry and stone circle geometry is not only its lithology type of finer sediments, but also its angularity. Mud boils generally tend to assume a more regular, compact form, however topographical effects on mud boil geometries may change drastically. Since Grid 16N is on the eastern plateau of the HRV, the elevation difference between the maximum (137.24 m.a.s.l.) and minimum (134.24 m.a.s.l.) is 3.00 m throughout the grid boundary.

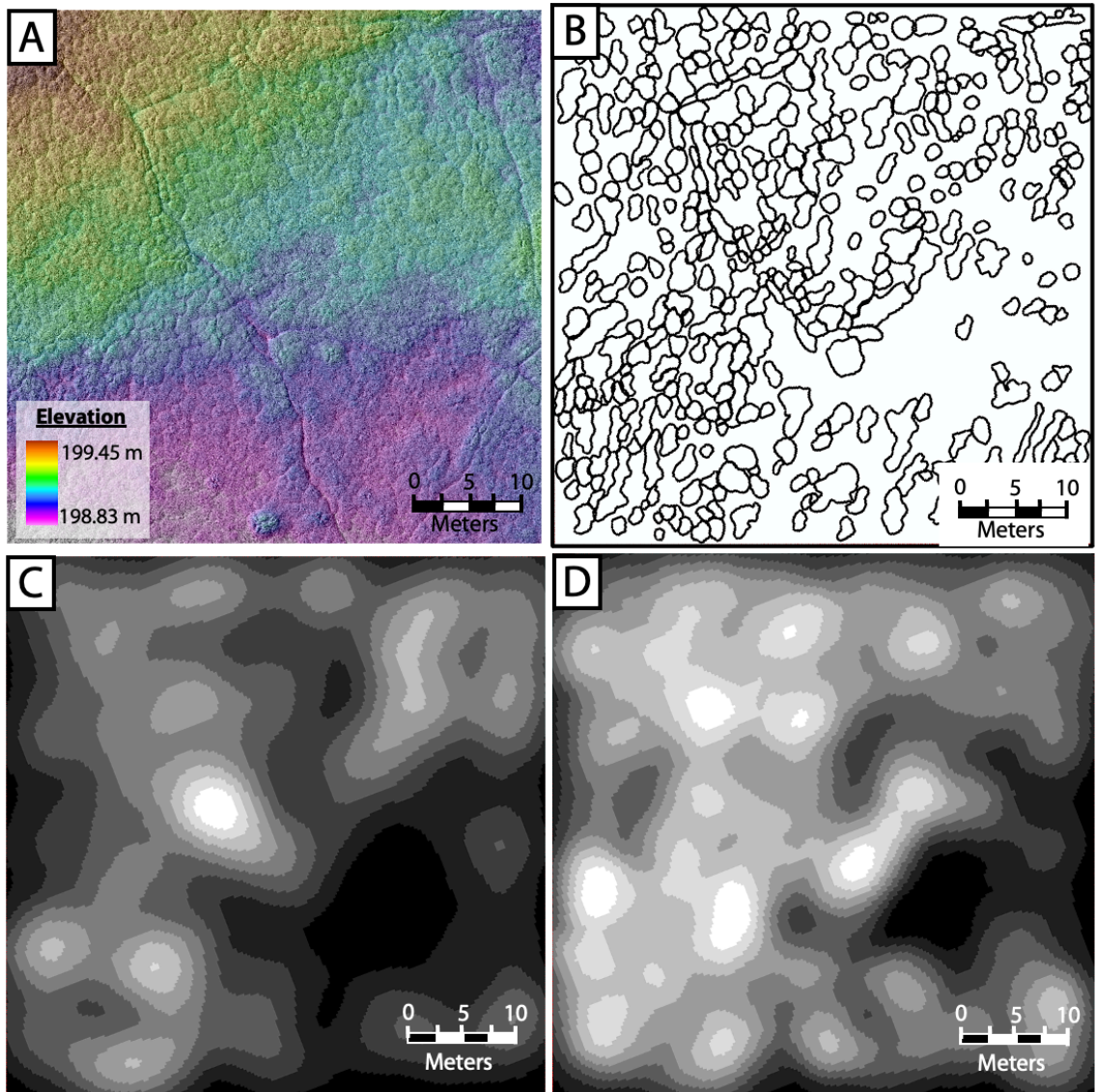
Grid 16AD also exemplifies mud boils similar to Grid 16N however, it is on the opposite plateau of the HRV to the northwestern portion. The mean area for the mud boils in this grid is  $0.94 \text{ m}^2 \pm 0.73$  with a mean elongation ratio of  $0.69 \pm 0.2$  and a mean compactness of  $0.79 \pm 0.15$  (**Table 3.3; Figure 3.9**). The mud boils in Grid 16AD are widespread throughout the entirety of the grid, which can also be seen overprinting polygonal patterns on the ground. This is another example of the complex idea of patterned ground occurring within patterned ground. Topographically, the elevation difference at this grid is much less in comparison to Grid 16N as the difference between the maximum (199.45 m.a.s.l.) and

minimum (198.83 m.a.s.l.) is 0.62 m even though it is evidently at a higher elevation downstream.



**Figure 3.8.** (A) LiDAR digital elevation map showing topographical variations on a centimeter scale of mud boils and frost-shattered nets. (B) Mapped mud boil geometries in Grid 16N. (C) KDE model of the elongation ratio of Grid 16N mud boils. Lowest elongation ratio values (values closer to 0) that show more elongated features are shown in dark grey with the lighter shades signifying higher elongation ratios (values closer to 1), which are more equally rounded features. (D) KDE model of the area of mud boils in

Grid 16N. Larger areas are indicated by white and smaller areas are indicated by the darker shades.



**Figure 3.9.** (A) LiDAR digital elevation map showing topographical variations on a centimeter scale of mud boils and frost-shattered nets. (B) Mapped mud boil geometries in Grid 16AD. (C) KDE model of the elongation ratio of Grid 16AD mud boils. Lowest elongation ratio values (values closer to 0) that show more elongated features are shown in dark grey with the lighter shades signifying higher elongation ratios (values closer to 1), which are more equally rounded features. (D) KDE model of the area of mud boils in

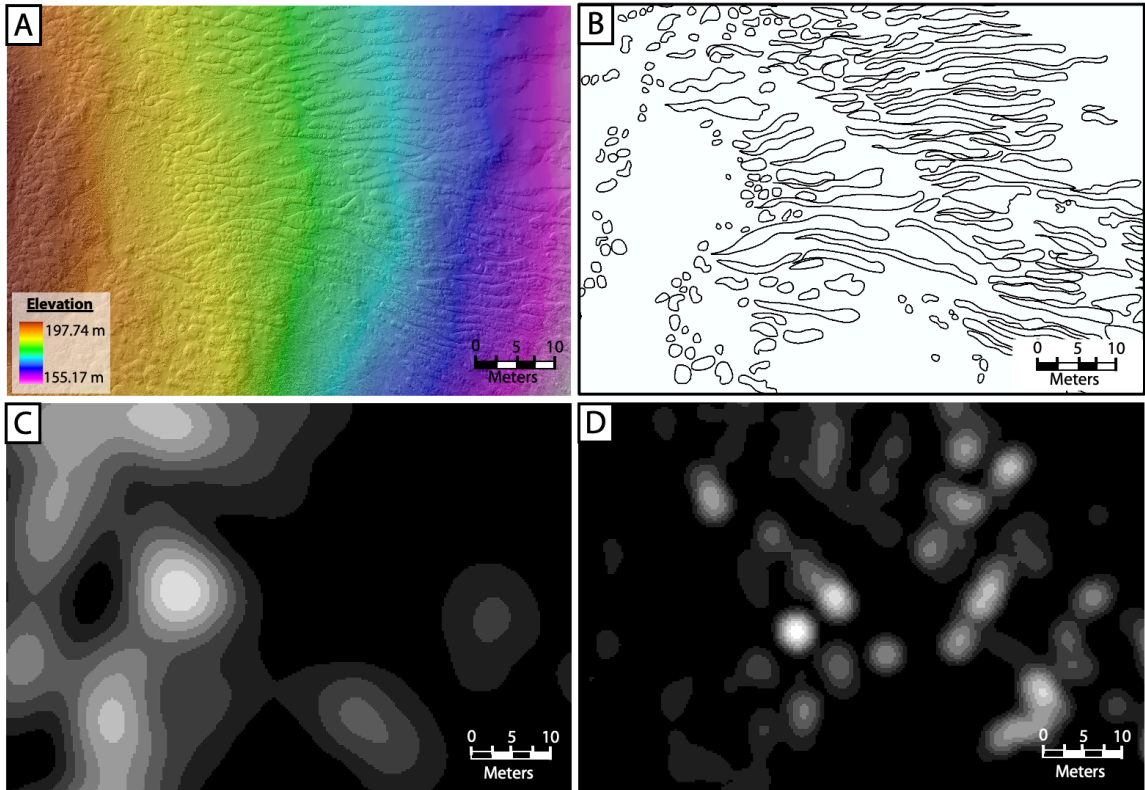
Grid 16AD. Larger areas are indicated by white and smaller areas are indicated by the darker shades.

## Stone Stripes

Stone Stripes are periglacial patterned ground features that are often associated with solifluction processes or frost creep due to the presence of a sloped topography. In this Stone Stripes grid (**Figure 3.10**), the slope is  $17^\circ$ . With respect to lithology and substrate, these stone stripes contain very poorly sorted, angular clasts with a grey and light brownish coarse sand matrix. The stone stripes follow their down flow pattern with ridges in the centre that appear to be cracked (**Figure 3.2d**). These ridges have fine sediment sorted in the middle where there are cracks, while the coarser sediment can be found scattered along the top and mostly on the side edges of the stripes. This grid is unique as it does not only sit atop the Eleanor River Formation but it also transitions into the clast-rich impact melt rock unit with some potential mixing. The permafrost thaw depth was excavated to be at 0.55 m on July 25<sup>th</sup> 2019.

Although, this LiDAR grid is larger in surface area, there is a total of 273 mapped stone stripe samples in this grid with a mean area of  $33.54 \text{ m}^2 \pm 39.09$ . These stone stripes are characteristically and quantitatively elongated with the highest mean elongation ratio of all the grids of  $0.5 \pm 0.39$  as well as a mean compactness of  $0.62 \pm 0.31$  (**Table 3.3; Figure 3.10**). This grid also has the largest variation in elevation change with a total difference of 42.57 m as seen in the topographic gradient illustrated in **Figure 3.10**.





**Figure 3.10.** (A) LiDAR digital elevation map showing topographical variations on a centimeter scale. (B) Mapped Stone Stripes geometries. (C) KDE model of the elongation ratio of Stone Stripes. Lowest elongation ratio values (values closer to 0) that show more elongated features are shown in dark grey with the lighter shades signifying higher elongation ratios (values closer to 1), which are more equally rounded features. (D) KDE model of the area of Stone Stripes. Larger areas are indicated by white and smaller areas are indicated by the darker shades.

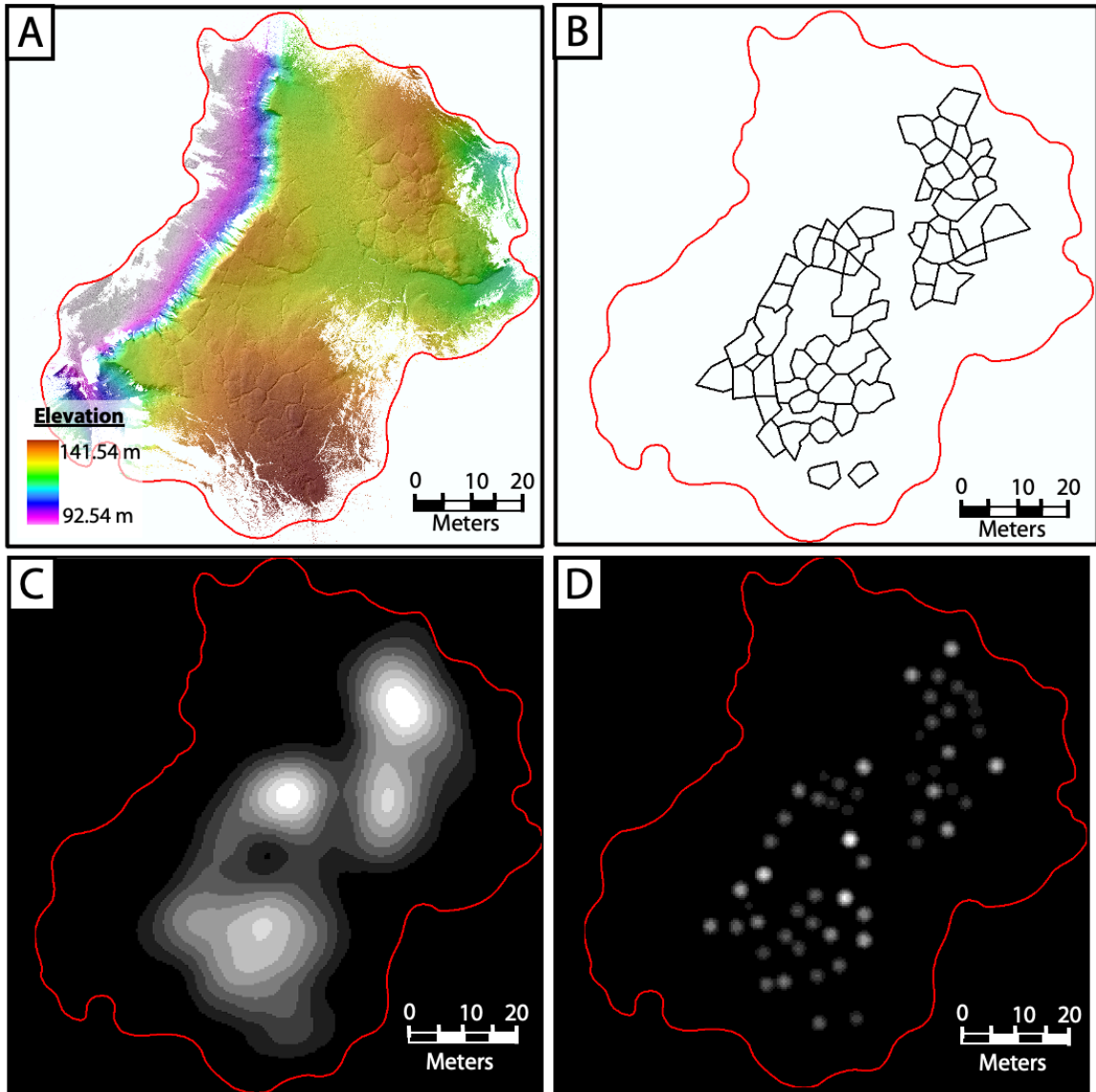
### Polygonal Terrain: *East Camp Polygons & Grids 16D, 16K, 16L*

Upon field observation, the East Camp Polygons area is atop the eastern plateau of the HRV that are highly incised by gully erosion. The gullies connect into the polygon systems via polygon troughs transitioning into flow paths or levee channels. The polygon trough intersection is 4.00 m wide with an approximate height of 0.30 m filled with fine dark grey silty clay sediment or highly weathered clast-rich impact melt rock material (**Figure 3.2h**; **Figure 3.11**). Sediment sizes were acquired in field measurements using a grain size card.



In comparison to the other sites, this site did not have an abundance of gravel, pebble or cobble substrate. This site has a thaw depth of 0.59 m on July 19<sup>th</sup> 2019.

Polygons are one of the most ubiquitous periglacial patterned ground landforms and the geometry of these features are interesting in many ways. This polygonal terrain has a mean surface area of  $983.86 \text{ m}^2 \pm 451.71$ , which are the largest patterned ground features observed from a centimeter scale perspective. These polygons have a mean elongation ratio of  $0.72 \pm 0.13$  and a mean compactness value of  $0.75 \pm 0.09$  (**Table 3.3; Figure 3.11**). The elevation change in this DEM is representative of the entire polygona plateau system which encompasses the gulley system draining into the valley floor as well. These gullies are associated with the occurrence and continuation of the polygonal troughs, that account for the lowest elevation values. The total elevation difference in this grid is 49.00 m, however, the polygons are situated at the upper limit of that elevation scale difference as it sits on top of the plateau irrespective of the gullies. It is also important to note the polygonal features that are dominated by stone circles in Grids 16D, 16K, and 16L (**Figures 3.5-3.7**). Although polygon troughs are less visible in the LiDAR grid coverages, these polygons were formed in coarse grained fluvial sediment (i.e. gravel) as opposed to fine grained material.

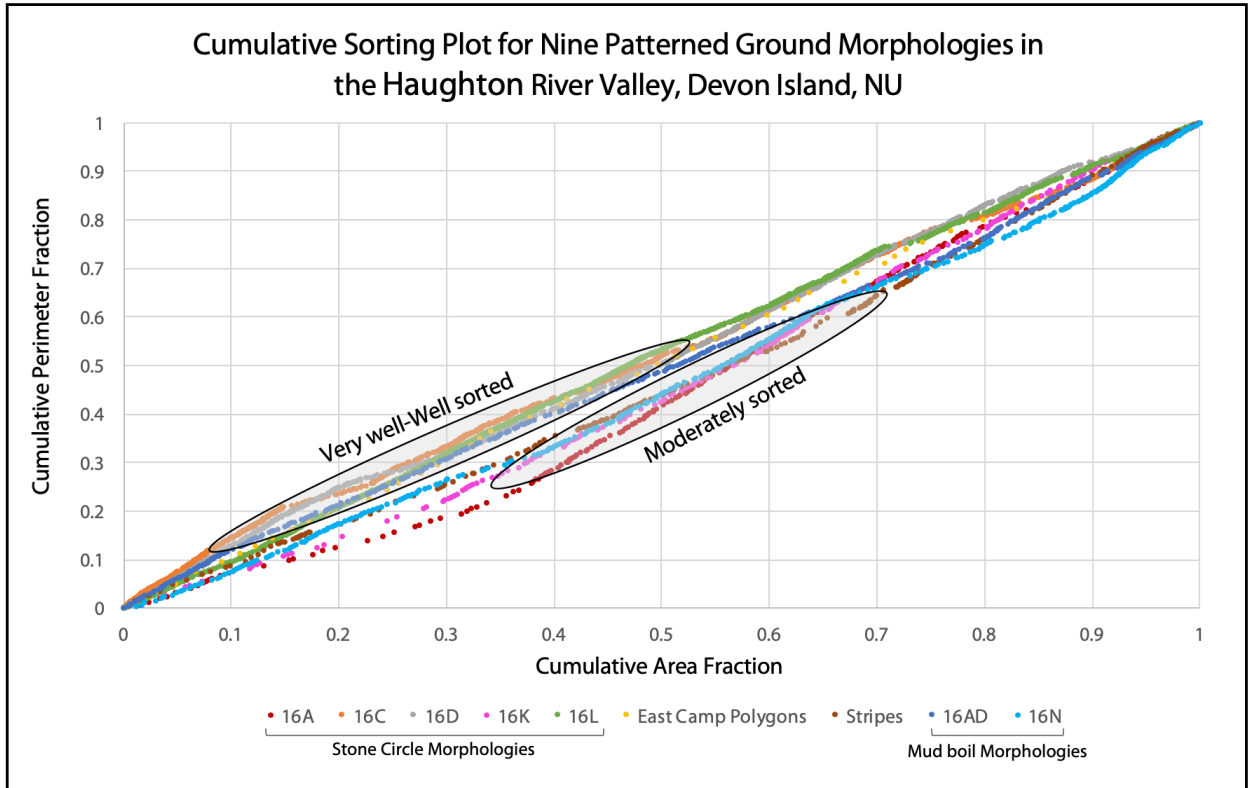


**Figure 3.11.** (A) LiDAR digital elevation map showing topographical variations on a centimeter scale. (B) Mapped polygon geometries of East Camp Polygons. (C) KDE model of the elongation ratio of polygons in HRV. Lowest elongation ratio values (values closer to 0) that show more elongated features are shown in dark grey with the lighter shades signifying higher elongation ratios (values closer to 1), which are more equally rounded features. (D) KDE model of the area of polygons in HRV. Larger areas are indicated by white and smaller areas are indicated by the darker shades.

### 3.4.2 Cumulative Spatial Sorting Analysis

For each patterned ground phenotype that had vectorized shapes, the cumulative area fraction over the total area was plotted against the cumulative perimeter fraction over the total perimeter. The resulting plot (**Figure 3.12**) potentially differentiates two sorting levels of progression given all samples from nine different patterned ground morphologies. The fraction cut-offs may be due to larger and more complex sediment grain/rock sizes that create a shift in the cumulative values (Chanou et al., 2014). Overall, the closer the slope value is to 1, the more spatial sorting there is on the maps (**Figures 3.3b-3.11b**), showing a continuous linear distribution. The slope indicates a faster rate of fraction increase for the less-sorted ground with steeper and more discontinuous distributions. Poor sorting can reach slopes larger than 3.

Two sorting groups were estimated by looking at the resultant cumulative sorting plot: *very well to well sorted* and *moderately sorted*. Very well to Well sorted range from slope values of 0.96-1.00 while the moderately sorted display slopes of 1.01-1.06. The very well-well sorted group in the graph (**Figure 3.12**) shows that most stone circle morphologies (Grid 16C, 16D, and 16L) tend to be very well sorted with respect to their geometries and shape with the exception of two grids, Grid 16A and 16K. In image analysis, Grids 16A and 16K both appeared to be mid-transition/quasi stone circles that tend to more oblate and crenulated in form given the same general substrate type. This group also includes the East Camp Polygon field, classifying these polygonal shapes are very well sorted geometries. The moderately sorted group in the graph (**Figure 3.12**) shows that both Stripes and mud boil morphologies tend to appear with less morphological sorting with decreasing regularity in shape and form in lateral space. Although, Grid 16N is less sorted than Grid 16AD, they both appear to be in similar depositional plateau top environments on opposite ends of the HRV but may therefore share different ground and local topographic controls.



**Figure 3.12.** Scale plot of the degree of spatial sorting using cumulative area and perimeter fractions for all patterned ground types based on vectorized shape maps (Figures 3.3b-3.11b). Using image analysis, there are potentially two groups of very well-to well sorted and moderately spatially sorted periglacial landforms derived from GIS maps (adapted plotting technique from Chanou et al., 2014)

### 3.5 Discussion

The data from this study of patterned ground housed within a small geographic region of the HRV indicates that there may be process-form relationships and interactions between the various types of patterned ground confined within the river valley, regarding their formation, frequency, and transition into the periglacial fluvial-valley landsystem. This interpretation considers the various patterned ground complexes given their different lithological types, microtopography, and substrate- and altitudinal-dependence.

### 3.5.1 Variations in Patterned Ground Morphology

Using high resolution LiDAR mapping, we mapped nine patterned ground grid sites in the Haughton River Valley using LiDAR vectorization and kernel density estimation (KDE) models, which are rarely used methods in periglacial geomorphology but allows for GIS analyses of high-scale spatial distribution (i.e. Boike and Yoshikawa 2003, Dabski et al., 2017). Using high-resolution LiDAR allowed us to quantify the landscape in sub-centimeter resolutions, which provided several advantages in the quality of detail, surface properties, and accuracy of geomorphologic parameters/features where decimeter scale satellite imagery is currently not able to provide. Moreover, spatial analysis on patterned ground proves to be very difficult due to the fact that geomorphic changes and evolution of periglacial terrain can be subtle and may require precise and repetitive measuring (Kääb et al., 2014; Hallet, 2013; Hallet and Prestrud, 1986).

In this study, image analysis through a schematic cumulative spatial sorting plot shows the degree of spatial sorting within this various patterned ground landforms situated in different lithologies of the impact structure. The fine (clay, sand) sediments in the Impact Melt Rock unit contain *mud boils* (Grid 16N; **Figure 3.8**), *frost-shattered nets* (Grid 16AD; **Figure 3.9**), and *polygons* (**Figure 3.11**), while *sorted stone circles* are more common in the coarse (gravel, cobble) sediments in the Eleanor River Formation and Fluvial units (Grid 16A, 16C, 16D, 16L; **Figure 3.3-3.5, 3.7**) *crenulated patterns* (Grid 16K; **Figure 3.6**), and *stone stripes* (**Figure 3.10**). According to the KDE analysis, the most elongated landforms are the stripes, stone circles, polygons, and mud boils, respectively. Correlated with their slopes, the stone stripes LiDAR grid (**Figure 3.10**) showed the highest slope difference and the mud boils (**Figures 3.8 and 3.9**) showed the lowest. Geomorphologically, this indicates that the most elongated features are hugely influenced by the regional slope of the site (Ballantyne, 2001; Naithani and Prasad, 1998; Francou and Texier, 1995; Gallagher, 2010). Microtopographic changes within the grids also match with the prevalence of the crenulated stone circle phenotypes. The most compact are the (crenulated) stone circles, mud boils, polygons, and stone stripes respectively (**Table 3.3; Figure 3.3-3.11**).

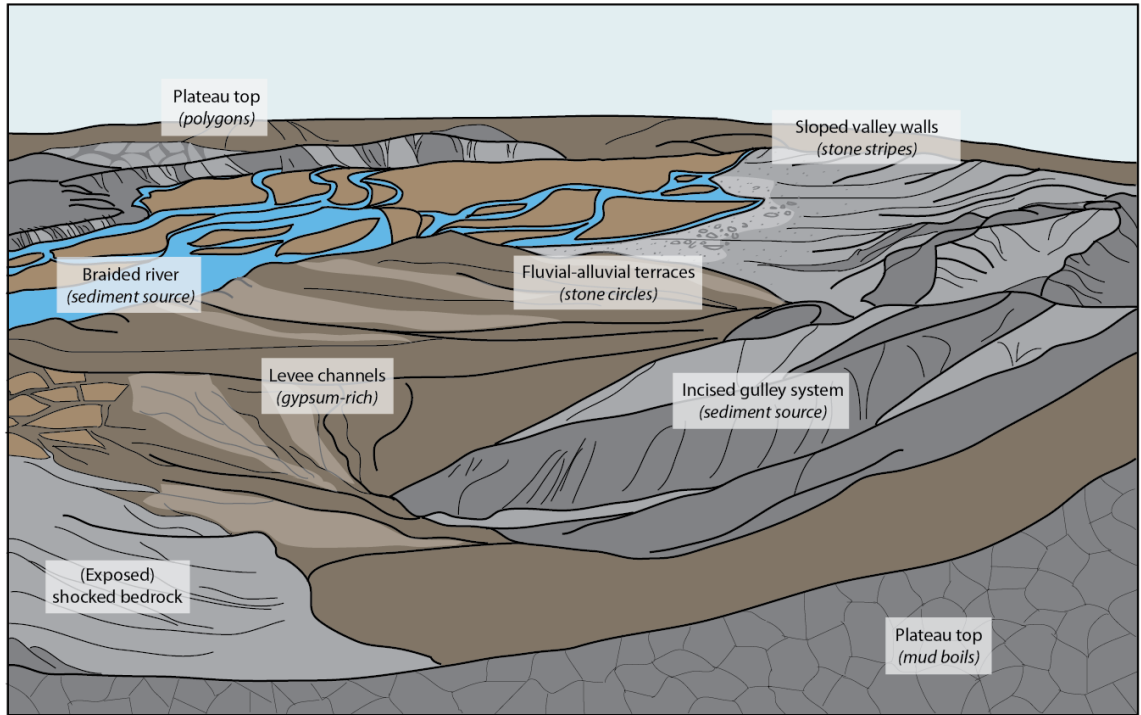
Along with the specified patterned ground groupings in the HRV, overtime, complex periglacial and fluvial processes begin to overlap, and form hybridized patterned ground geomorphology wherein we can observe the unique and uncommon features of patterned ground within patterned ground (i.e. stone circles within a polygon; **Figures 3.5-3.7**). Previous research (i.e. Hallet, 1990; Kessler and Werner, 2003) explore the self-organization of patterned ground from periodic patterned ground to scale-invariant topography (or microtopography) such as in HRV. Microtopography is the subtle centimeter scale change in elevation that should be a characteristic feature of many periglacial environments that is commonly lacking investigation. Consequently, microtopography may allow and account for the subtle creep, development, and slow evolution of periglacial landforms. Microtopographic features (from what seems to be invariant topography) can now be resolved with the hyper-resolution, sub-centimeter scale LiDAR, meaning that these complex spatial resorting and reorganization of the surface may be able to delineate confounding processes that may be acting on the study region simultaneously. By looking at hyper-resolution DEMs, sorted patterned ground (i.e. via freeze/thaw alterations, or frost heave), seems to be highly affected and interconnected via *microtopography, slope, and general lithology*,

Additionally, altitudinal distribution and lateral variability of periglacial landforms in the HRV suggest that periglacial processes are especially active between 90 and 140 m.a.s.l in the valley with a full elevation range of HRV being 75-151 m.a.s.l. This is most prevalent in sites where there is a topographical gradient; however, more specifically in order for pattern ground to evolve in space, microtopography may also play an important role.. In this study, patterned ground with coarser grains appears to be most morphologically affected by microtopography along with other environmental factors, while fine grained patterned ground are the least influenced by any microtopographic effect. Furthermore, microtopography may also be influencing the formation of more complex architectures of patterned ground within patterned ground. This patterned ground complex allows more than one formation mechanism (i.e. thermal contraction, circumventing cells, etc.) to generate a variety of overlapping patterns. For example, the morphology of stone stripes clearly indicates direction of a slow sediment transfer. These landforms frequently host

anchored boulders or small bedrock outcrops erosional incisions (**Figure 3.10**). However, places such as Grid 16D, 16K, 16AD, with microtopographic controls, have had stone circles and mud boils, evolve into elongated and crenulated polygon troughs. Quantifying these changes is thoroughly important in order to create an architectural analysis of the entire landsystem by using these different subunits and their possible interpretations.

### 3.5.2 Periglacial Landsystem Model for the Haughton River Valley

Periglacial landforms are widespread throughout that Haughton Impact Structure. With a unique location in the Canadian High Arctic within the continuous permafrost zone, the Haughton River Valley is dominated by periglacial patterned ground. More specifically, in the localized zone of the Haughton River Valley, a proposed periglacial landsystem model for a valley/plateau environment is conceptualized in **Figure 3.13**. This model considers the various types of patterned ground given their different lithological types, microtopography, and substrate- and altitudinal-dependence. In this periglacial landsystem model, the various phenotypes of patterned ground are also highlighted to show their spatial position in the valley. In essence, (crenulated) stone circles tend to appear more on the valley floor of the HRV within coarse-grained fluvial sediments; mud boils and polygons tend to be associated with finer grained material and valley-top locations, while stone stripes are more prevalent in highly sloped topography. In complex cases, patterned ground within patterned ground can also be seen in the study area as sediments reorganize in response to both strong active layer and fluvial (or alluvial) processes as exemplified in the valley floor of the HRV (**Figures 3.5-3.7**).



**Figure 3.13.** Conceptual periglacial landsystem model of the Haughton River Valley (HRV), Haughton Impact Structure, Devon Island, Nunavut. This perspective is upstream of the HRV.

### 3.6 Conclusions

The Haughton River Valley (HRV) in the Haughton Impact Structure, Devon Island exemplifies a network of various patterned ground phenotypes in a small geographic region. Patterned ground geomorphologies that are present in the HRV include, *stone circles, mud boils, polygons, and stone stripes*. A comprehensive quantitative analysis was done to nine study sites around the HRV to model the spatial distribution of patterned ground in relation to the local environment. Using the landsystem analysis approach in conjunction with hyper-resolution LiDAR, several sites were characterized and quantified using vector Geographic Information System (GIS) techniques. Patterned ground on every site was digitized for shape and spatial analysis using the Kernel Density Estimation (KDE) models. With this, parameters of *diameter, area, perimeter, elongation ratio, compactness, and long axis azimuth* were quantified. Showing the general trend that polygons and stripes have the largest diameter (5-31 m), while stone circles and mud boils have the smallest



diameter (0.5-1.2 m). In stone circles and mud boils observations, larger sizes are often associated with low topographic relief and smaller morphologies are located at high topographic relief. This may have implications with microtopographic factors controlling the re-distribution of subsurface and surface processes from a high to low elevation area – stone circles are good examples of contiguous regularly spaced patterns and microrelief features, whose origins are related to frost heave and hydrostatic pressures in the soil and have convoluted structures, typical of patterned ground disturbance (Washburn, 1979; Williams and Smith, 1989). Moreover, KDE plots of elongation ratio and circularity show that for all patterned ground, patterns become more elongate even with the slightest topographic change (i.e.  $<1^\circ$ ). Therefore, slope can be associated with changes in patterned ground shape and size and surface movement. In order of the highest elongation (elongation ratio of 1 = straight line) and lowest circularity, the most elongate patterned ground are as follows: stone stripes (0.31), stone circles (0.20), mud boils (0.16), and polygons (0.13).

Along with a robust quantitative shape analysis through the hyper-resolution LiDAR, different patterned ground morphologies within HRV can now be classified together as either very well sorted or moderately sorted using the cumulative sorting plot algorithm according to their vectorized shapes and spatial distribution. This yields a distinct classification of two groups of sorting within the HRV: (1) Very-well sorted = polygons and stone circles and (2) Moderately sorted = mud boils and stone stripes.

The derivation of the quantitative differences in patterned ground sorting and surface processes would not be possible without the use of hyper-resolution LiDAR. The sub-centimeter resolution capability of the Akkha3W LiDAR system is unprecedented and has significant utility within the periglacial environment given that features of interest such as patterned ground, are on the micro-scale that the highest altimetry Arctic dataset (i.e. ArcticDEM, 2m spatial resolution) still cannot provide. This is important to consider when organizing imaging field campaigns due to the fact that the use of a kinematic LiDAR system or even a high-resolution UAV to generate digital terrain models of periglacial landforms are ideal imaging platforms for detailed mapping studies.

With this, we are able to quantify the variation of the morphology of patterned ground across the HRV at sub-centimeter, hyper-resolutions showing that stone circles are most prevalent in the fluvial, coarse-grained valley floors, mud boils and polygons mostly occur in fine-grained, valley-plateau tops, and stone stripes are able to occur at slopes of 17 degrees. We are also able to delineate that through the altitudinal distribution and lateral variability of periglacial landforms in the HRV, this suggests that periglacial processes are distinctly active between elevations of 90-140 m.a.s.l.

Using a landsystem approach, in this study, we were able to determine that patterned ground morphologies within the HRV are connected via *microtopography*, *slope*, and *general lithology*, which are all confounding factors that affect patterned ground on a surficial level. Further lithologic and/or grain size analysis of various sampled areas of patterned ground need to be expanded with samples collected in each grid to conduct more detailed sedimentological facies association of the subsurface processes underlying these periglacial depositional environments. Studying patterned ground complexes via landsystem analysis has significant implications not only to periglacial systems but also to hydrological systems, subsurface permafrost dynamics, and High Arctic permafrost preservation.

### 3.7 References

- Anisimov, O.A., D.G. Vaughan, T.V. Callaghan, C. Furgal, H. Marchant, T.D. Prowse, H. Vilhjálmsson and J.E. Walsh, 2007: Polar regions (Arctic and Antarctic). Climate Change 2007: Impacts, Adaptation and Vulnerability. Contribution of Working Group II to the Fourth Assessment Report of the Intergovernmental Panel on Climate Change, M.L. Parry, O.F. Canziani, J.P. Palutikof, P.J. van der Linden and C.E. Hanson, Eds., Cambridge University Press, Cambridge, 653-685.
- Ballantyne, C.K. and Matthews, J.A., 1982. The development of sorted circles on recently deglaciated terrain, Jotunheimen, Norway. *Arctic and Alpine Research*, 14(4), pp.341-354.
- Ballantyne, C.K. and Matthews, J.A., 1983. Desiccation cracking and sorted polygon development, Jotunheimen, Norway. *Arctic and Alpine Research*, 15(3), pp.339-349.
- Ballantyne, C.K., 1997. Periglacial trimlines in the Scottish Highlands. *Quaternary International*, 38, pp.119-136.
- Ballantyne, C.K., 2001. The sorted stone stripes of Tingo Hill. *Scottish Geographical Journal*, 117(4), pp.313-324.
- Boike, J. and Yoshikawa, K., 2003. Mapping of periglacial geomorphology using kite/balloon aerial photography. *Permafrost and periglacial processes*, 14(1), pp.81-85.
- Boon, S., Burgess, D.O., Koerner, R.M. and Sharp, M.J., 2010. Forty-seven years of research on the Devon Island ice cap, Arctic Canada. *Arctic*, pp.13-29.
- Chanou, A., Osinski, G.R. and Grieve, R.A.F., 2014. A methodology for the semi-automatic digital image analysis of fragmental impactites. *Meteoritics & Planetary Science*, 49(4), pp.621-635.
- Christie, R., Embry, A. and Van Dyck, G., 2003. Eleanor River Formation. [online] Natural Resources Canada. Available at: <<https://weblex.nrcan.gc.ca/html/004000/GSCC00053004554.html>> [Accessed 19 June 2020].
- Cox, N.J., 2007. Kernel estimation as a basic tool for geomorphological data analysis.

- Earth Surface Processes and Landforms: The Journal of the British Geomorphological Research Group, 32(12), pp.1902-1912.
- Dąbski, M., Zmarz, A., Pabjanek, P., Korczak-Abshire, M., Karsznia, I. and Chwedorzewska, K.J., 2017. UAV-based detection and spatial analyses of periglacial landforms on Demay Point (King George Island, South Shetland Islands, Antarctica). *Geomorphology*, 290, pp.29-38.
- Douglas R. J. W. 1970. Introduction. In *Geology and economic minerals of Canada*. Geological Survey of Canada Economic Geology Report 1, edited by Douglas R. J. W. Ottawa: Geological Survey of Canada. pp. 2–8.
- Francou, B. and Texier, J., 1995. Stratified slope deposits: the stone-banked sheets and lobes model. *Steepland Geomorphology*. John Wiley, Chichester, pp.147-169.
- Gallagher, C., Balme, M.R., Conway, S.J. and Grindrod, P.M., 2011. Sorted clastic stripes, lobes and associated gullies in high-latitude craters on Mars: Landforms indicative of very recent, polycyclic ground-ice thaw and liquid flows. *Icarus*, 211(1), pp.458-471.
- Hallet, B., 1990. Spatial self-organization in geomorphology: from periodic bedforms and patterned ground to scale-invariant topography. *Earth-Science Reviews*, 29(1-4), pp.57-75.
- Hallet, B., 2013. Stone circles: form and soil kinematics. *Philosophical Transactions of the Royal Society A: Mathematical, Physical and Engineering Sciences*, 371(2004), p.20120357.
- Hallet, B. and Prestrud, S., 1986. Dynamics of periglacial sorted circles in western Spitsbergen. *Quaternary Research*, 26(1), pp.81-99.
- Harris SA, French HM, Heginbottom JA, Johnston GH, Ladanyi B, Sego DC, van Everdingen RO (eds) (1988) Glossary of permafrost and related ground-ice terms. Technical memorandum no 142. Permafrost Subcommittee, National Research Council of Canada, Ottawa.
- Haugland, J.E., 2004. Formation of patterned ground and fine-scale soil development within two Late Holocene glacial chronosequences: Jotunheimen, Norway. *Geomorphology*, 61(3-4), pp.287-301.
- Haugland, J.E., 2006. Short-term periglacial processes, vegetation succession, and soil

- development within sorted patterned ground: Jotunheimen, Norway. *Arctic, Antarctic, and alpine research*, 38(1), pp.82-89.
- Kääb, A., Girod, L.M.R. and Berthling, I.T., 2014. Surface kinematics of periglacial sorted circles using structure-from-motion technology. *The Cryosphere*, 8, pp.1041-1056.
- Kerguillec, R., 2014. Recent patterned grounds development on a glacier surface (Dovrefjell, central Norway): an ephemeral periglacial activity in a paraglacial context. *Geografiska Annaler: Series A, Physical Geography*, 96(1), pp.1-7.
- Kling, J., 1997. Observations on sorted circle development, Abisko, northern Sweden. *Permafrost and Periglacial Processes*, 8(4), pp.447-453.
- Lauriol, B., Hetu, B., Cote, D. and Gwyn, H., 1985. Karstic and Periglacial Phenomena in a Variable-level Lake from Anticosti Island, Quebec, Canada. *Seitschrift fur Geomorphologie.*, 29(3), pp.353-365.
- Maclachlan, J.C. and Eyles, C.H., 2013. Quantitative geomorphological analysis of drumlins in the Peterborough drumlin field, Ontario, Canada. *Geografiska Annaler: Series A, Physical Geography*, 95(2), pp.125-144.
- Matthews, J.A., Shakesby, R.A., Berrisford, M.S. and McEwen, L.J., 1998. Periglacial patterned ground on the Styggedalsbreen glacier foreland, Jotunheimen, southern Norway: micro-topographic, paraglacial and geoecological controls. *Permafrost and Periglacial Processes*, 9(2), pp.147-166.
- Naithani, A.K. and Prasad, C., 1998. Downslope soil movement in a periglacial region of Garhwal Himalaya: Rates, processes and climatic significance. *Current Science*, pp.365-372.
- Osinski, G.R., Lee, P., Spray, J.G., Parnell, J., Lim, D.S., Bunch, T.E., Cockell, C.S. and Glass, B., 2005. Geological overview and cratering model for the Haughton impact structure, Devon Island, Canadian High Arctic. *Meteoritics & Planetary Science*, 40(12), pp.1759-1776.
- Swanson, D.K., Ping, C.L. and Michaelson, G.J., 1999. Diapirism in soils due to thaw of ice-rich material near the permafrost table. *Permafrost and Periglacial Processes*, 10(4), pp.349-367.
- Thorsteinsson R. and Tozer E. T. 1970. Geology of the Arctic Archipelago. In *Geology*

and economic minerals of Canada, Geological Survey of Canada Economic Geology Report 1, edited by Douglas R. J. W. Ottawa: Geological Survey of Canada. pp. 547–590

- Washburn, A.L., 1980. *Geocryology: a survey of periglacial processes and environments*. Wiley.
- Vermeesch, P., 2007. Quantitative geomorphology of the White Mountains (California) using detrital apatite fission track thermochronology. *Journal of Geophysical Research: Earth Surface*, 112(F3).
- van Huissteden, J., 2020. The Role of Ground Ice. In *Thawing Permafrost* (pp. 107-177). Springer, Cham.
- Van Vliet-Lanoë, B., 1988. The significance of cryoturbation phenomena in environmental reconstruction. *Journal of Quaternary Science*, 3(1), pp.85-96.



to a thermal source. These all play a significant role in the response of a polygonal complex to climate, and therefore their formation in the aforementioned distinctive zones.

Chapter 3 explored the quantification of patterned ground using a DEM-derived dataset from a kinematic backpack LiDAR with sub-centimeter resolution in the Haughton River Valley. Specifically, shape descriptors of *diameter*, *area*, *perimeter*, *elongation ratio*, *circularity*, and *long axis azimuth* were calculated and plotted using the Kernel Density Estimation (KDE) model. The KDE models show the distribution of vectorized patterned ground shapes (i.e. stone circles), which tend to get bigger in size at lower elevations and more elongate in sloped elevations. A cumulative sorting plot was also applied to various patterned ground phenotypes such as polygons, mud boils, stone stripes, and stone circles. Overall, using quantitative geomorphology, there are two potential degrees and groups of sorting: (1) Very-well sorted group, which encompasses *polygons and stone circles* and (2) Moderately sorted, which encompasses *mud boils and stone stripes*. However, with these spatially clustered occurrences of patterned ground in a very small locale in the HRV, it is important to recognize how patterned ground landforms may be interconnected within a periglacial domain using landsystem analysis.

## 4.1 Contributions to Periglacial Science

### 4.1.1 The Periglacial Landsystem

A landsystem is a fundamental methodology of evaluating and classifying terrain based on the documentation of landforms and sediments and an understanding of the depositional processes that created them (Evans and Twigg 2002; Cooke and Doornkamp, 1990). The characterization of the periglacial landsystem is complex and often under-explored. Landsystem analyses of different glacial environments (i.e. proglacial, glaciofluvial, glaciolacustrine, etc.) are more commonly explored in scientific literature in comparison to periglacial environments.

In this thesis, two landsystem models are proposed for the Canadian High Arctic: (1) the *Strand Fiord “Fossil” Fan Ice-wedge Polygon Network Landsystem* in Axel Heiberg Island and (2) the *Haughton River Valley-Plateau Patterned Ground Landsystem* in the



Haughton Impact Structure, Devon Island. Two differing periglacial environments and dynamics were explored in Chapters 2 and 3, with the main take-away being that periglacial landsystem analysis, which involves a combination of sediment/subsurface architectural analysis, non-invasive, remote sensing and geophysical techniques, and fieldwork applications is an important tool in order to understand the entire locality of a specific periglacial system and its components. For example, the *Strand Fiord “Fossil” Fan Ice-wedge Polygon Network Landsystem* may be classified as a wet-cold polar desert environment, while the *Haughton River Valley-Plateau Patterned Ground Landsystem* may be classified as a dry-cold polar desert environment. Moreover, the value of this method lies not only in its ability to classify and simplify complex terrain (i.e. periglacial patterned ground), but also in its application to the understanding and delineating subsurface deposits and processes especially in complex periglacial domains.

#### 4.1.2 3D-GPR and Sedimentology of Ice-wedge Polygons

Ground penetrating radar (GPR) is a geophysical technique that allows non-destructive stratigraphic imaging of the subsurface. It records the two-way travel time of electromagnetic (EM) waves reflected at boundaries between sub-surface layers with contrasting relative permittivity thereby developing dielectric contrasts due to variations in sediment grain size, water content, and mineral composition. Moreover, GPR can optimally be used to look for signs of past or present water in the subsurface. In this thesis, the detection of the presence or absence of ice-wedges within polygon networks was fundamental. In order to characterize the widespread subsurface dynamics of polygonal terrain in general, not only did we use geophysical methods but also coupled with sedimentological and remote sensing field methods.

In Strand Fiord, Axel Heiberg, three singular radargrams revealed that ice-wedges were only present in the subsurface of the *Medial/Transition Zone* of the alluvial fan and not present in the *Apex* or the *Distal* zones. 3D-GPR revealed that these ice wedges are asymmetric in shape and discontinuous in the subsurface. We were also able to calculate the volume of ice-wedge housed in a 25 m x 25 m GPR grid, which resulted to 43.28 m<sup>3</sup> of ice. These results have significant implications for ground ice as a resource and mapping

permafrost and ice-wedge geometry in relation to the surface geomorphology of the ice-wedge polygons.

In tandem with GPR, sedimentological observations and interpretations proved to be significant in terms of characterizing the subsurface lithology of the ice-wedge polygons. The smaller sized polygons in the *Apex* showed larger sandy-grain sizes, while the largest-sized *Distal Zone* polygons showed the finest grains in their sediment profiles. Overall, this study showed that the size of the polygons are inversely proportional to their grain size and sorting.

## 4.2 The Canadian High Arctic as an Icy Analogue for Mars

Patterned ground are ubiquitous periglacial landforms that are commonly found on planetary bodies such as Earth and Mars. The Canadian High Arctic is often regarded as one of the best periglacial analogue sites due to its arid and well-preserved, polar environment. Research implies that patterned ground (i.e. polygons and stone crenulations) on Mars are key indicators that ground ice is present or was present in the recent past. This thesis emphasizes the importance of using terrestrial techniques and analogues to improve our understanding of the role of ice not only in the Canadian High Arctic but on Mars, both in the past and present, through its associated landforms. Since  $> 21$  million  $\text{km}^3$  of ice have been detected at or near the surface of Mars, terrestrial analogue fieldwork is crucial, not only to test future in-situ resource excavation methods, but also to better understand glacial/periglacial processes and their relationship to climate, geomorphology, and ice content. In particular, polar deserts and regions of relict icy terrains such as the Canadian high Arctic provide a unique opportunity to connect field work, geomorphology, geophysics, and modeling efforts. In situ sampling and characterization systems being developed for Mars will benefit from testing at terrestrial analogue sites. However, significant advances in understanding patterned ground and other periglacial phenomena will require further integration of field and theoretical studies.

#### 4.2.1 Targeted Techniques to Characterize Periglacial Terrain

There are several non-invasive methods that are proposed to help guide instrumentation in future missions in order to characterize periglacial patterned ground and terrain. Firstly, a GPR instrument aboard a rover platform (i.e. Radar Imager for Mars' Subsurface Experiment (RIMFAX) on the Perseverance rover and Water Ice Subsurface Deposit Observation on Mars (WISDOM) on the ExoMars rover) would be an ideal instrument primarily for ice detection and stratigraphic reconnaissance of the subsurface. Although the landing sites, Oxia Planum and Jezero Crater may not necessarily house large subsurface ice systems, the GPR will still aid in the stratigraphic imaging of the subsurface. Secondly, a rover-based kinematic LiDAR to act as an integrated vision system (IVS) for mapping rover tracks, obstacles, and path elevations that will help for planning and traversing a study site. This system is likely advanced and may have capabilities of automation and classifying objects in sight for further analysis. Thirdly, an in-depth sedimentological suite to analyse grain size that has excavation capabilities especially for sample collection or resources (i.e. water-ice). An instrument such as a microscopic imager (i.e. MAHLI on Curiosity) along with a trowel tool to make incisions to clear sediment faces would be sufficient in order to conduct sedimentological logging (i.e. important for grain size analysis, architectural- primary/secondary sedimentological structures, applying facies codes). Overall, a mission combining all these elements, which could be achieved through a combination of an uncrewed aerial vehicle (UAV) and a lander or rover, would provide a detailed characterization of the ice content, distribution, and depth of an ice deposit on Mars. This has significant implications not only for the localization of ice-rich sites and geological characterization of periglacial terrain, but also for ISRU and management of water as a resource on the Martian mid-latitudes for future exploration missions. The continued research of Martian periglacial environments through comparative geology and geophysics of Earth analogues is largely relevant for the future of Mars exploration – the periglacial landsystems in the Canadian High Arctic pose as ideal candidate, analogue sites for future planetary, glacial and periglacial exploration.

# Curriculum Vitae

**Name:** Chimira Nicole Andres

**Post-secondary Education and Degrees:** McMaster University  
Hamilton, Ontario, Canada  
2014-2018 H.B.Sc.

The University of Western Ontario  
London, Ontario, Canada  
2018-2020 M.Sc.

**Honours and Awards:** Eric Mountjoy Exchange Award  
*Geological Association of Canada*  
2020

LPI Career Development Award  
2020

The Northern Scientific Training Program (NSTP)  
2019

Robert and Ruth Lumsden Graduate Award in Earth Sciences  
2019, 2020

**Related Work Experience** Teaching Assistant  
*University of Western Ontario, London, ON*  
2018-2020  
*McMaster University, Hamilton ON*  
2016-2018

Communications and Outreach Assistant  
*Institute of Earth and Space Exploration*  
*University of Western Ontario, London, ON*  
2019-2020

**Publications:**

Andres, C., Eyles, C., Jara, H. and Narro-Pérez, R., 2018. Sedimentological Analysis of Paleolake Jircacocha, Cojup Valley, Cordillera Blanca, Peru. *Revista de Glaciares y Ecosistemas de Montaña*, (5), pp.1-18.